NASA-CR-168577
19820012239

The Telecommunications and Data Acquisition Progress Report 42-67

November and December 1981

N. A. Renzetti
Editor

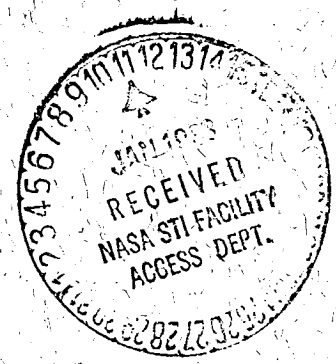

February 15, 1982

NASA
National Aeronautics and
Space Administration

Jet Propulsion Laboratory
California Institute of Technology
Pasadena, California

PRINTS
ENTER:D'82N20113' PRINTS REQUESTED

DISPLAY 82N20113/2

82N20113*# ISSUE 10 PAGE 1455 CATEGORY 99 RPT#: NASA-CR-168577
JPL-PR-42-67 82/02/15 140 PAGES UNCLASSIFIED DOCUMENT

UTTL: The telecommunications and data acquisition report TLSP: Progress Report, Nov. - Dec. 1981

AUTH: A/RENZETTI, N. A. PAT: A/ed.

CORP: Jet Propulsion Lab., California Inst. of Tech., Pasadena. AVAIL.NTIS SAP: HC A07/MF A01

Sponsored by NASA

MAJS: /*DATA ACQUISITION/*DEEP SPACE NETWORK/*LOGISTICS MANAGEMENT/*RADIO COMMUNICATION/*SPACECRAFT TRACKING

MINS: / COMPUTERIZED SIMULATION/ DECISION MAKING/ GEODESY/ GLOBAL POSITIONING SYSTEM/ GROUND STATIONS/ HELIOS 1/ HYDROGEN MASERS/ MAINTENANCE/ RADIO ANTENNAS/ RADIO ASTRONOMY/ RADIO RECEIVERS/ SPACE MISSIONS/ SPARE PARTS/ SUPPORT SYSTEMS/ SYSTEMS ANALYSIS/ TELEMETRY/ TRACKING STATIONS

ANN: Progress in the development and operations of the Deep Space Network is reported. Developments in Earth-based radio technology as applied to other research programs are also reported. These programs include geodynamics, astrophysics, and radio searching for extraterrestrial intelligence in the microwave region of the electromagnetic spectrum. For individual titles, see N82-20114 through N82-20130.

ENTER:

The Telecommunications and Data Acquisition Progress Report 42-67

November and December 1981

N. A. Renzetti
Editor

February 15, 1982

NASA
National Aeronautics and
Space Administration

Jet Propulsion Laboratory
California Institute of Technology
Pasadena, California

The research described in this publication was carried out by the Jet Propulsion Laboratory, California Institute of Technology, under contract with the National Aeronautics and Space Administration.

Preface

This publication was formerly entitled *The Deep Space Network Progress Report*. Although the practice of reporting progress in the development and operations of the Deep Space Network continues, the report has been expanded to include developments in Earth-based radio technology as applied to other research programs. These programs are:

(1) Geodynamics: For several years, the laboratory has been developing radio interferometry at microwave frequencies for application to geodetic measurements. This branch of telecommunications technology is now being applied to the study of geodynamics.

(2) Astrophysics: The deep space stations, individually and in pairs as an interferometer, have been used by radio astronomers for astrophysics research by direct observations of radio sources.

(3) An activity closely related to radio astronomy's use of the deep space stations is NASA's continuing program of radio search for extraterrestrial intelligence in the microwave region of the electromagnetic spectrum.

Each succeeding issue of this report will present material in some, but not all, of the following categories:

Radio Astronomy
Search for Extraterrestrial Intelligence
Radio Interferometry at Microwave Frequencies

- Geodetic Techniques Development
- Spacecraft Navigation
- Orbiting Very Long Baseline Interferometry

Deep Space Network

- Description
- Program Planning
- Planetary and Interplanetary Mission Support
- Advanced Systems
- Network and Facility Engineering and Implementation
- Operations
- Spacecraft Radio Science
- Planetary Radar
- Energy

In each issue, there will be a report on the current configuration of one of the seven DSN systems (Tracking, Telemetry, Command, Monitor and Control, Test Support, Radio Science, and Very Long Baseline Interferometry).

The work described in this report series is either performed or managed by the Telecommunications and Data Acquisition organization of JPL.

Contents

NETWORK AND FACILITY ENGINEERING AND IMPLEMENTATION

Network

OPERATIONS

Network Operations

Deep Space Stations

SETI Downconverter

B. Crow
Communications Systems Research Section

The SETI (Search for Extraterrestrial Intelligence) breadboard subsystem was begun in order to develop the technology to efficiently implement a SETI instrument capable of searching wide bandwidth with high resolution. Due to the recent directive from Congress to terminate the program, NASA has tasked JPL to complete the SETI breadboard (since it is more than half complete) so that it will be available for use by a NASA-selected user by the end of FY 82. The downconverter covered in this report is the interface hardware between the receiver IF output and ADC used as the input to the spectrum analyzer.

The SETI (Search for Extraterrestrial Intelligence) downconverter has been developed to interface between an IF input and provide complex baseband outputs for use in the SETI breadboard system (see Fig. 1).

The SETI downconverter subassembly (see Fig. 2) has been built in a modular fashion with 13 modules in the SETI downconverter drawer and the required monitor and control and power supplies in a second drawer. The downconverter accepts both a 30-MHz IF (for use at an Arecibo receiver) and a 50-MHz IF (for use with a Block III DSN receiver). The 50-MHz IF is translated to 30 MHz in the downconverter. Two types of signal gain control are available: (1) an AGC loop with loop time constants of 0.1, 1, and 10 sec, and (2) a computer control gain control that offers a 35-dB dynamic range. An ADC is provided to measure the output of the AGC detector and is calibrated to provide an indication of output power. The IF signal is basebanded in the complex mixer where careful attention has been paid to the amplitude and phase balance between the two baseband signals (see Fig. 3). An internal test signal is available to allow stand-alone testing of the downconverter (and the SETI breadboard). The downconverter is controlled and monitored by a PDP 11/44 and is currently operating as designed in the development laboratory.

Table 1 is a list of the technical requirements and the measurements that have been made to confirm the downconverter performance.

Table 1. Downconverter requirements vs measured performance

Parameter	Requirement	Measurement
Input bandwidth	10 MHz	16 MHz
Input frequency	30 MHz 50 MHz Test signal	30 MHz 50 MHz 28 MHz
Baseband output	.1 VRMS	.1 VRMS
AGC dynamic range	>30 dB	50 dB
AGC time constant	0.1, 1, 10 sec	0.1, 1, 10 sec
Compute controllable gain range	≥30 dB	35 dB (see Fig. 4)
Input impedance	50 ±5 ohm	58 ohm
Baseband frequency response	4 MHz	4.3 MHz
Rejection of unwanted harmonic	≥30 dB	2nd harmonic = −46 dB 3rd harmonic = −52 dB
Phase and amplitude balance	90 ±3 0 ±0.5 dB	See Fig. 3 See Fig. 3
Linearity	Pin max ≤−25 dBm	See Fig. 7
Noise figure	–	See Fig. 6
ADC power readout	–	See Fig. 5

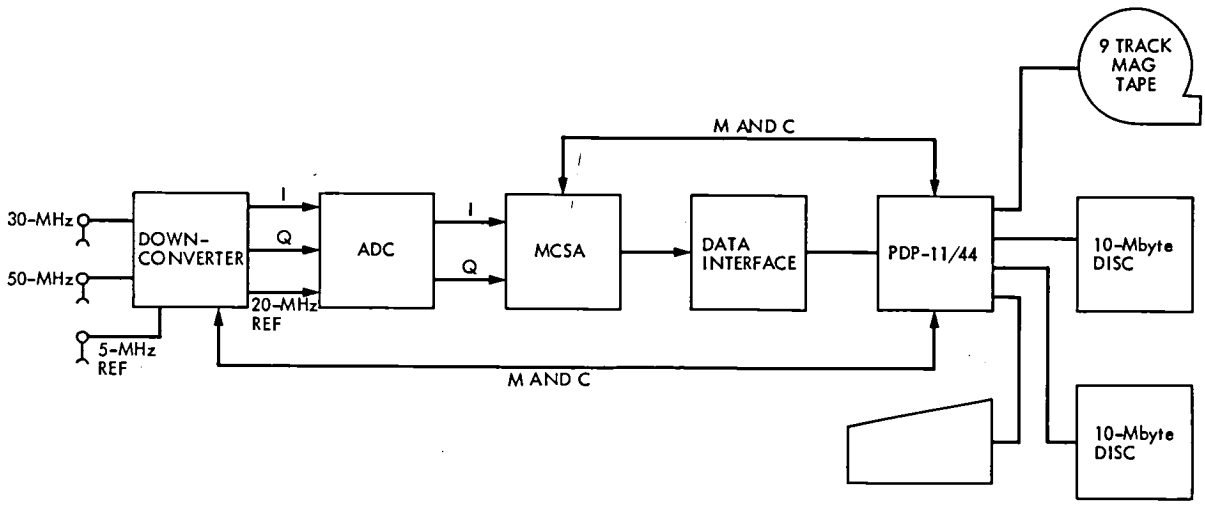

Fig. 1. SETI breadboard

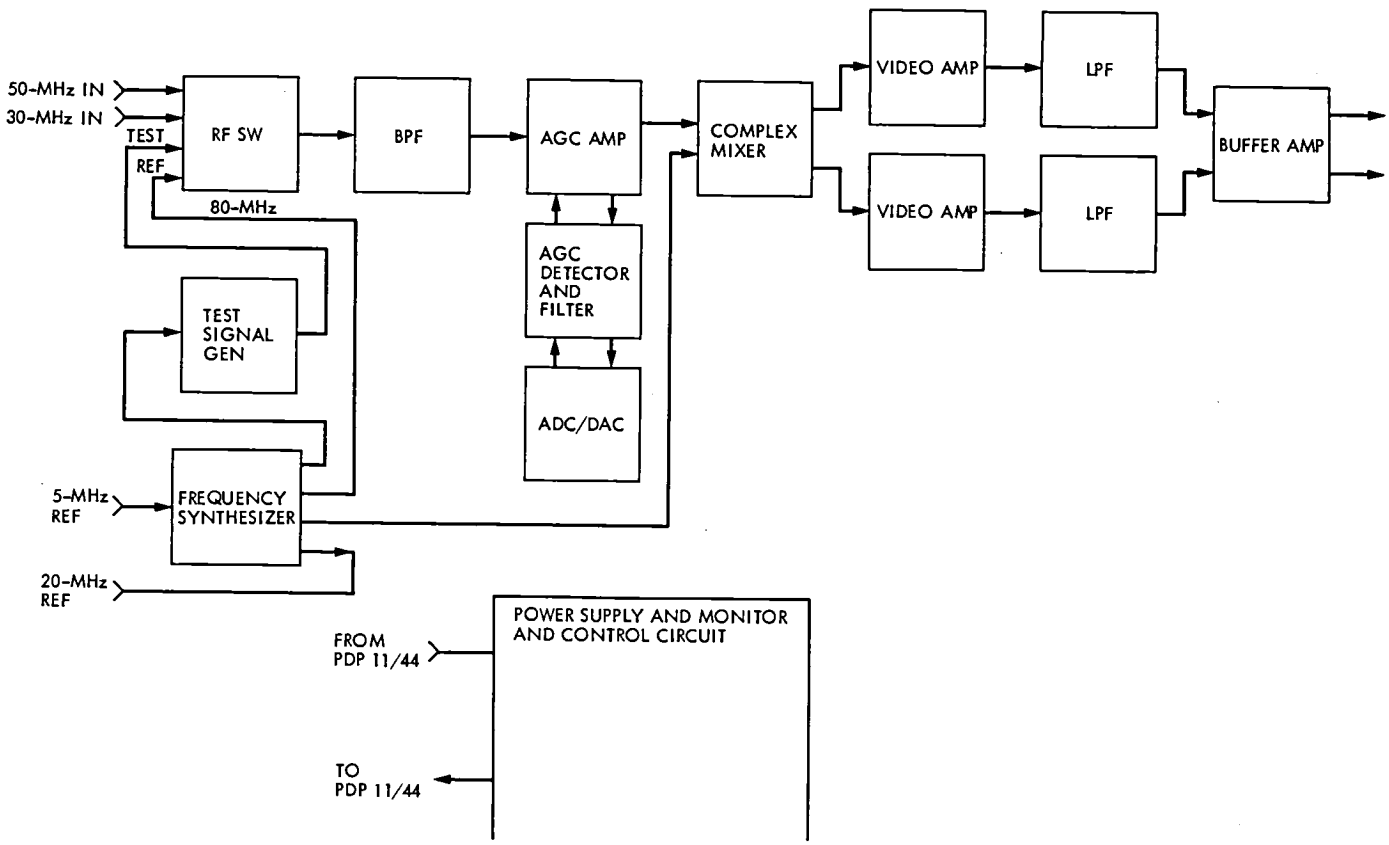

Fig. 2. SETI downconverter block diagram

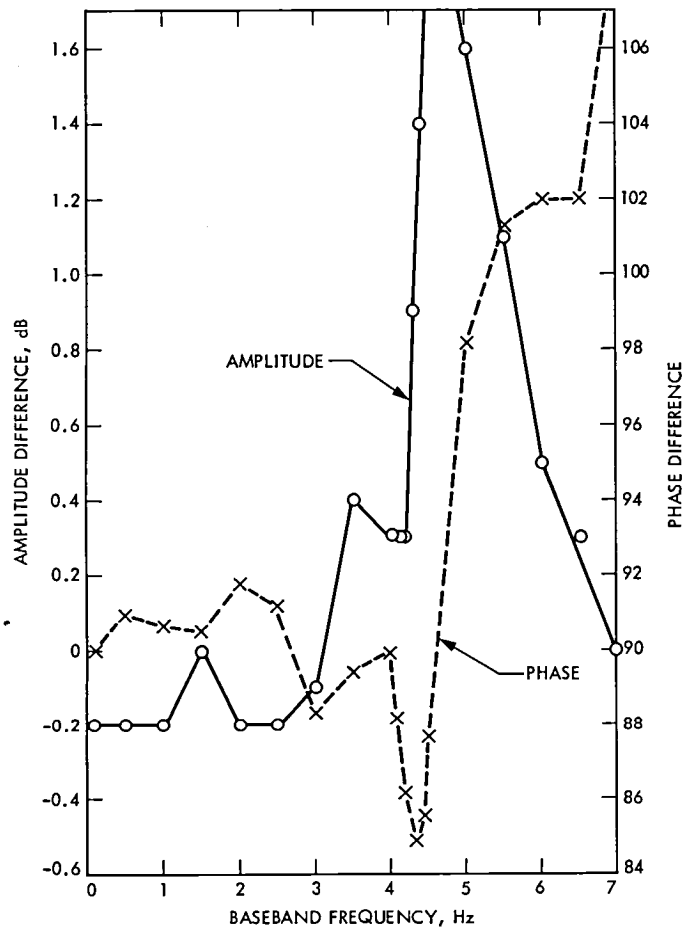

Fig. 3. SETI downconverter phase and gain balance vs frequency

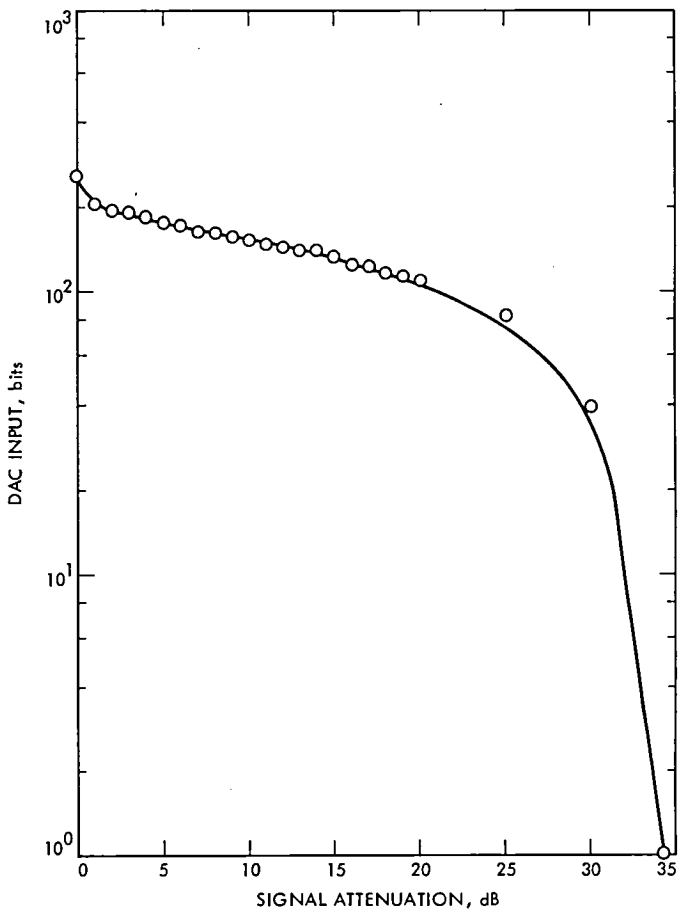

Fig. 4. SETI downconverter DAC input vs signal attenuation

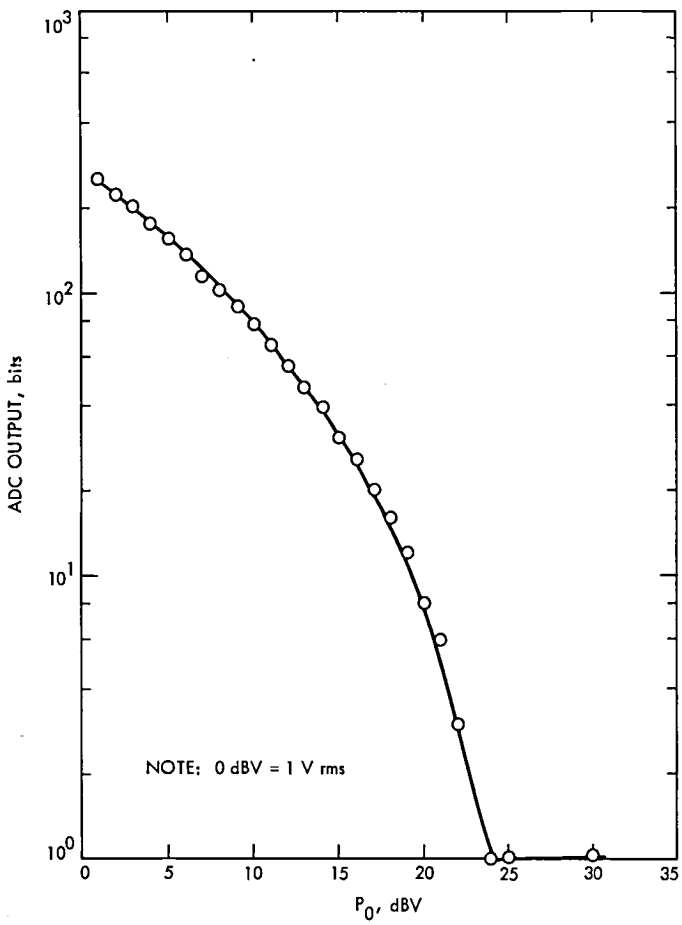

Fig. 5. SETI downconverter ADC output vs signal power output

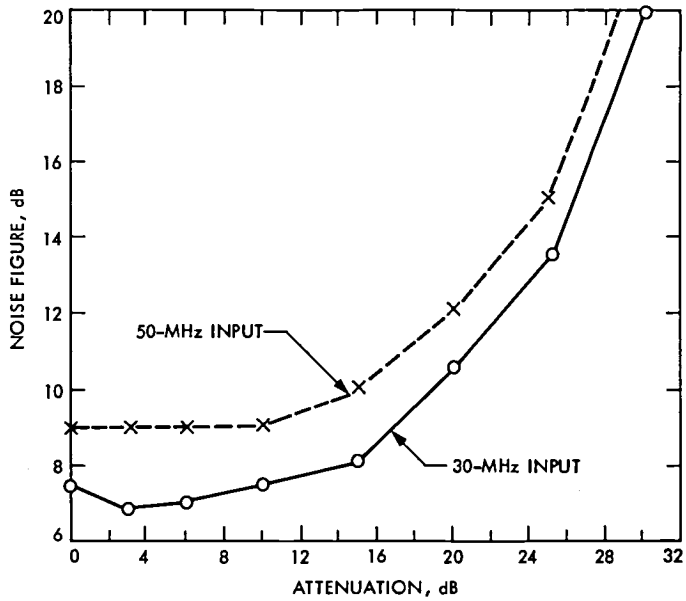

Fig. 6. SETI downconverter noise figure vs downconverter attenuation

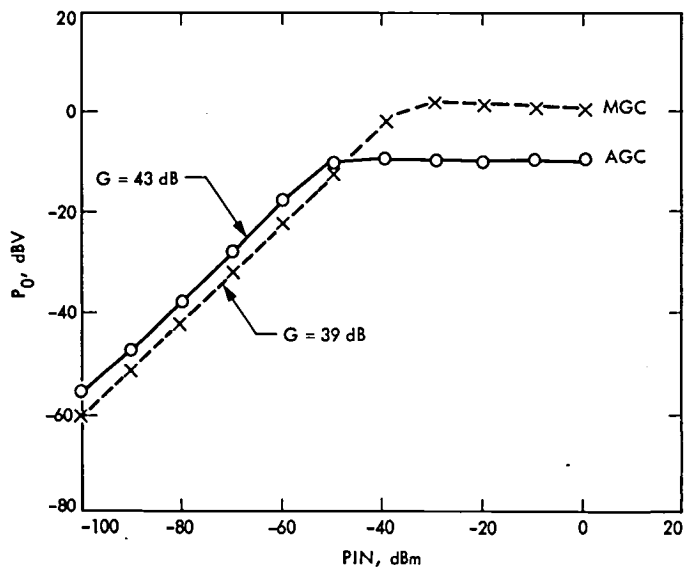

Fig. 7. SETI downconverter gain linearity for both AGC and MGC

The DSN Radio Science System Mark III - 1980

B. J. Buckles
TDA Engineering Office

The DSN Radio Science System supported the Voyager 2 Saturn encounter radio science experiments in August 1981. Support for these experiments was provided by all the Deep Space Stations of the DSN. However, the critical support for the Saturn occultation and ring scattering experiment was provided at DSS 43 by the medium-band open-loop recording system. The implementation of the medium-band open-loop recording system at DSS 43 culminated many years of effort by the DSN to provide a DSN multimission radio science capability, and all 64-m DSS open-loop recording systems are now essentially identical. This article describes the DSN Radio Science System, emphasizing the recent implementation at DSS 43.

I. Introduction

Figure 1 is a block diagram representation of the DSN Radio Science System (RSS) recently used to successfully support the Voyager 2 Saturn encounter radio science experiments. The DSN Deep Space Stations (DSSs) are the heart of this system. In particular, DSS 43 was the prime supporting station for the radio science experiments at Voyager 2 Saturn encounter. DSS 43 supported the Saturn planetary occultation and ring scattering experiments with a newly implemented medium-band recording system consisting of a highly phase-stable, four-channel, open-loop receiver and a high-rate, high-density digital recorder. Also, a wideband recording system consisting of a four-channel, wide-bandwidth, open-loop receiver and digital recorder was installed at DSS 43 to serve as a backup to the medium-band system.

Other new implementations provided to support the Voyager radio science experiments were modifications to the Precision Power Monitor (PPM) to provide more reliable operation of the instrument and new operational software for the Occultation Data Assembly (ODA) that provided an interface to the PPM, allowing PPM data to be recorded by the ODA and, thus, system temperature information to be provided with the Original Data Record (ODR) recordings. Also the capability to play back data from the DSS over the wideband data lines for system testing purposes was provided.

The following sections describe the DSS subsystems that support the DSN Radio Science System in detail. In addition, each of the other facilities supporting the DSN Radio Science System, the Ground Communications Facility (GCF) and the Network Operations Control Center (NOCC) and their support functions are described. The narrative in general will describe the flow of data from receipt at the antenna through the system as indicated on the Radio Science System block diagram (Fig. 1).

II. The Deep Space Stations

The Deep Space Station (DSS) is the Radio Science System instrument. DSS system performance directly determines the degree of success of the experiment, and system calibration determines the degree of uncertainty in the results of the experiment. The following paragraphs describe those functions performed by the individual subsystems depicted in Fig. 1. Specific configuration and calibration requirements are addressed in a separate paragraph after the functional descriptions of the subsystems.

A. The Antenna Mechanical Subsystem

The 64-m antenna mechanical subsystems function as large-aperture collectors which, by double reflection, focus incoming radio frequency (S- and X-band RCP/LCP) energy into the S- and X-band feedhorns (part of the Antenna Microwave Subsystem).

The large collecting surface of the antenna focuses the incoming RF energy onto the hyperboloid subreflector which is adjustable in both axial and tilt positions to permit optimization of the focusing of energy into the feedhorns. The subreflector is locked into a fixed position for many radio science events. The subreflector then reflects the received energy to the dichroic plate, a device that reflects S-band energy to the S-band feedhorn and transmits X-band energy to the X-band feedhorn.

Transmitted S-band RF energy emanating from the feedhorn is focused by the same reflectors into a narrow cylindrical beam. Since the beam is very narrow, the antenna must be pointed with high accuracy and precision. This is accomplished by a series of drive motors and gear trains which rotate those portions of the structure that support the reflectors, position sensors, and related electronics. Electronic servo amplifiers are used to amplify and condition the axes angles or position error signals which are received and are provided to the drive motor controls.

Pointing angles are computed from an ephemeris provided by the Project, and the antenna is pointed to these angles. Once the receiver has acquired a signal to provide feedback, a radio source can be tracked by scanning around it (CONSCAN) and computing pointing angles from signal-level information supplied by the receiver. During periods when excessive signal-level dynamics or low received signal levels are expected, i.e., occultations and some other radio science experiments, CONSCAN cannot be used and angle pointing is accomplished by manually inserting offsets to the computed angle predict set.

B. The Antenna Microwave Subsystem

The antenna microwave subsystem accepts the received S- and X-band RCP/LCP signals at the feedhorn from the antenna mechanical subsystem. The received signals are transmitted through the polarizer plates to the orthomode transducer. The polarizer plates are adjusted so that RCP signals are directed to X-band traveling wave maser 2 and S-band traveling wave maser 1 and so that LCP signals are directed to X-band traveling wave maser 1 and S-band traveling wave maser 2. After amplification by the masers, the signals are routed to the receiver-exciter subsystem via the microwave switching assembly.

The S-band uplink signal is transmitted via the diplexer assembly through the feedhorn to the antenna where it is focused and beamed to the spacecraft. The noise diode assemblies under control of the PPM inject known amounts of noise power into the received signal path so that accurate real-time system temperature measurements may be made.

C. The Transmitter Subsystem

The Transmitter Subsystem accepts the S-band frequency exciter signal from the receiver-exciter subsystem and amplifies it to a transmitted output level of 20 kW. The signal is then routed via the diplexer to the antenna and then focused and beamed to the spacecraft.

D. The Receiver-Exciter Subsystem

The Receiver-Exciter Subsystem receives, amplifies, and frequency downconverts spacecraft-radiated S- and X-band RCP/LCP signals. The closed-loop receivers provide doppler and ranging signals to the tracking subsystem. Dedicated open-loop receivers provide baseband signals to the radio science subsystem, and fixed-tuned, wide-bandwidth, open-loop receivers provide backup systems to the narrowband and medium-band open-loop receivers. The exciter generates the S-band drive signal provided to the transmitter subsystem that provides the spacecraft uplink signal.

The Spectral Signal Indicator provides local displays of received signal spectrums and routes spectral data to the radio science subsystem. These displays are used to validate radio science system data at the DSS, NOCC, and project areas.

The Precision Power Monitor (PPM) measures system temperatures by injecting known amounts of noise power into the signal path and comparing the total power within a given bandwidth before and during periods of noise injection. System temperature measurements are made for each of the four masers by utilizing the closed-loop receivers as monitoring

devices. This use of the receivers imposes a configuration restraint on them when they are used to monitor all four masers. That is, the Block IV receivers must monitor X-band RCP/LCP masers and the Block III receivers are used to monitor S-band RCP/LCP masers.

E. The Tracking Subsystem

The Tracking Subsystem receives the ranging spectrum and doppler signals from the Receiver-Exciter Subsystem. It generates a range code that is routed to the exciter and modulates the S-band uplink carrier. The demodulated range spectrum is compared to a model of the transmitted range code, and the round trip signal delay to the spacecraft is computed, formatted and transmitted to the GCF Data Records Subsystem, which produces an Intermediate Data Record (IDR) tape upon which the data are delivered to the Project. Similarly the doppler phase is counted, formatted, and delivered to the Project. The radio metric data supports radio science celestial mechanics and general relativity experiments in addition to providing a partial backup to the open-loop system.

In addition, the Tracking Subsystem computes data residuals and noise estimates, receives and stores predicts, and provides partial status information to the monitor and control subsystem including receiver AGC levels and lock status.

F. The Radio Science Subsystem

The Radio Science Subsystem digitizes, bandwidth reduces, and records (1) very narrow, (2) narrow, and (3) medium-bandwidth radio science data and digitizes and records wide-bandwidth radio science data. It receives radio science frequency predicts from NOCC, configuration and control data from the monitor and control subsystem, and S- and X-band RCP/LCP signals from the Receiver-Exciter Subsystem. It transmits spectral information from the SSI to NOCC via the GCF wideband data lines. It controls the narrow- and medium-band open-loop receiver local oscillator (LO) by sending frequency control information to the Receiver-Exciter Subsystem.

G. Monitor and Control Subsystem

The Monitor and Control Subsystem provides control messages to the centrally controlled DSS subsystems including the Radio Science and Tracking Subsystems. It provides partial status information for these same subsystems. It generates the angle drive tape needed by the Antenna Pointing Subsystem and, in addition, controls the SSI and PPM in the Receiver-Exciter Subsystem. It receives the system temperature information from the PPM and displays it on the Data System Terminal (DST). It relays the system temperature information to the NOCC Monitor Subsystem for display in NOCC and the project mission support area.

III. The Ground Communications Facility

The Ground Communications Facility provides the communication networks required to support the communication requirements of the Radio Science System. These facilities exist at the DSS and JPL and are briefly described in the following paragraphs.

A. GCF High-Speed Data Subsystem

The High-Speed Data Subsystem transmits radio science predictions from the NOCC to the DSS and CTA 21, and Radio Science System performance validation data from the DSS to NOCC.

B. GCF Wideband Subsystem

In real-time, the Wideband Subsystem transmits SSI data from the DSS to the NOCC.

C. GCF Data Records Subsystem

The GCF Data Records Subsystem formats and provides radio science data on computer-compatible tape to the flight projects.

IV. Network Operations Control Center

A. NOCC Radio Science Subsystem

The NOCC Radio Science Subsystem (NRS) generates open- and closed-loop radio science DTV graphics displays, and DRS status and configuration displays. In addition, the NRS provides the planetary atmosphere refracted trajectory input to the NOCC Support Subsystem for the purpose of generating radio science predicts.

B. NOCC Monitor Subsystem

The NOCC Monitor Subsystem displays system temperature information and supports the DSS Monitor and Control Subsystem.

C. NOCC Support Subsystem

The NOCC Support Subsystem generates DSS frequency and tracking predicts using a polynomial coefficient tape produced by the Planetary Orbital Ephemiris Atmospheric Study (POEAS) software as input. In addition, predicts can be generated using manual inputs.

D. NOCC Display Subsystem

The NOCC Display Subsystem provides the NOCC Radio Science Subsystem generated radio science displays to the Network Operations Control Area and to project radio science areas, and provides control data to the NOCC Radio Science Subsystem.

E. NOCC Tracking Subsystem

The NOCC Tracking Subsystem generates tracking system status displays and transmits them to the Display Subsystem to be routed and displayed.

V. CTA 21

A unique part of the Radio Science System exists at CTA 21. This equipment bandwidth-reduces wide-bandwidth radio science data recorded at the DSS. It receives digital wide-bandwidth and medium-bandwidth radio science data from the DSS Radio Science Subsystem, generates bandwidth-reduced radio science data, and provides medium- and wide-bandwidth radio science data on computer-compatible tape to the flight project.

VI. Open-Loop Recording System Pre-Pass Calibration

The recorded open-loop receiver signals were the prime deliverable data type for the Voyager 2 Saturn occultation and ring scattering radio science experiments. For that reason it was extremely important that the open-loop system be properly set up prior to the recording pass, and that a calibration tape be made. This calibration data serves as a benchmark of system performance and is later used to determine data quality and establishes the basic uncertainty in the results of the experiment.

VII. Purpose of the Calibration

The open-loop recording calibration tapes are made to accomplish the following:

(1) Establish the output of the open-loop receivers at a level that will not saturate the input to the Occultation Data Assembly (ODA) or Digital Recording Assembly (DRA) A/D converters.

(2) Provide data that will establish baseline values for the phase, frequency, and amplitude stability of the open-loop system.

To achieve goal 1, the calibration recording is made using a test signal generated by the exciter-translator that is set to provide the maximum predicted received signal level for the recording period. Then the output level of the receivers is adjusted to the level determined by the equation

$$S = \left[\frac{SNR + 1}{(2SNR + 2k\sqrt{2SNR} + k^2)}\right]^{1/2} \quad (1)$$

where

S = receiver output levels (volts rms)

SNR = expected received signal-to-noise ratio

k = number of sigma margin desired for saturation

L = A/D converter saturation level (volts)

In order to achieve goal 2 for medium-band recording, it is necessary to step the test signal across the bandpass of the receiver filter. This is done in ten 5-khz (at S-band) steps. Stepping the signal in frequency in this manner allows the necessary phase, frequency, and amplitude calibrations to be made. Frequency stepping is not necessary for narrow band recording.

So that a X-band RCP/LCP test signal may be generated a cap is provided that is placed over the X-band feedhorn from which a linearly polarized signal is injected into the horn. This cap is oriented such that the linearly polarized signal is transmitted equally by the orthomode coupler to its RCP and LCP output ports, thus providing equal RCP/LCP calibration signals.

A consequence of using a cap over the feedhorn in this manner to generate a test signal is that the X-band system temperature has been increased approximately 10 dB. It has, in effect, been terminated into an ambient load. To counter the 10-dB increase in receiver output power due to the presence of the cap it is necessary to insert 10-dB pads into the signal path at appropriate points. These must be removed after the calibration recording is made.

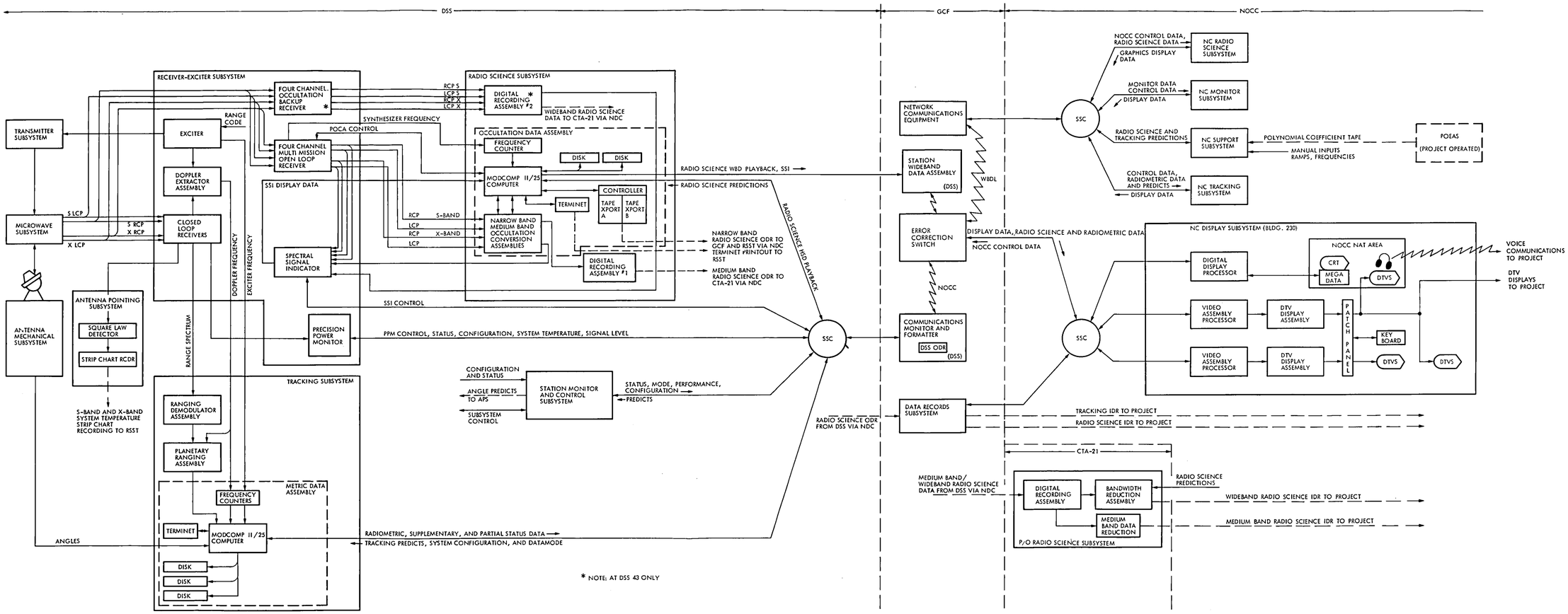

Fig. 1. Deep Space Network Radio Science System block diagram depicting the Radio Science System as configured to support the Voyager 2 Saturn encounter

A Summary of Space Flight Missions Supported by the Deep Space Network

E. S. Burke
Mission Support Operations Division

This article is a summary of all space flight missions that the Deep Space Network has supported, beginning with the Ranger Program and ending with the continuing coverage of the Voyager Program.

I. Introduction

The Deep Space Network (DSN) is managed and operated by the Jet Propulsion Laboratory under a NASA contract and has been since NASA was formed in 1958. The DSN is tasked to support all deep space planetary probes, including the lunar exploration.

Since the Ranger series in the 1960s the DSN has evolved to a highly sophisticated telecommunications and data acquisition network. The 26-meter antennas have been converted to 34 meters, and 64-meter antennas have been built at all complexes. The L-band systems were changed to S-band, with X-band now also being used on Voyager and Pioneer 12. Ranging systems were developed and are now used along with other techniques to determine exact spacecraft locations. Many other developments occurred during this period to support the requirements of future space flight missions.

II. The Programs

A. Ranger Program

The Ranger missions were a series of lunar probes to obtain pictures from different areas of the Moon, study space physics in transit, and analyze the human environment from a landed instrument package. The primary objective was the collection of preliminary information for scientific studies of possible landing sites for the NASA manned lunar program.

Several major technical advances were first used on Ranger. First, the spacecraft was fully stabilized in attitude, keeping a high-gain antenna pointed at Earth and solar cell panels aimed at the Sun, which was a technical challenge in the early 1960s. The second technical advance attempted, but not completed, was the landing of an instrument capsule on the lunar surface by means of a retrorocket.

B. Surveyor Program

The objective of these missions was the softlanding on the lunar surface of instrumented spacecraft capable of performing operations that would contribute scientific knowledge about the lunar surface. The Surveyors also returned data to explore landing sites in support of the Apollo Project.

C. Lunar Orbiter Program

These were photographic missions to obtain high-resolution pictures of the lunar surface while in orbit around the Moon.

The primary purpose was to search for and survey landing sites for the Apollo Project.

D. Mariner Program

This series of flight missions consisted of 10 different launches, of which three failed, that flew by Venus, Mars, Mercury, and orbited Mars. The objectives of these missions were to make interplanetary and planetary measurements consisting of the different science phenomena, and except for the first 2 Mariners, to return TV pictures of the different planets. The Mars Orbiter mapped the planet and returned data for site analysis for the Viking Landers.

E. Pioneer Program

The primary objective of the Pioneer 6 through 9 missions is to collect scientific data relative to interplanetary phenomena within a region approximately 0.8 to 1.2 astronomical units (AUs) from the sun. Phenomena of particular interest include the characteristics of electric and magnetic fields; electron density along the earth-spacecraft path; and temporal and spatial distribution of plasma, cosmic rays, high-energy particles, and cosmic dust.

The primary objectives of the Pioneer 10 and 11 missions are to conduct investigations of the nature of the Asteroid Belt, the physical characteristics of Jupiter and its immediate environment, and the interplanetary medium beyond the orbit of Mars and to the extreme of the spacecrafts' communications capabilities. Additionally, Pioneer 11 has a primary objective to investigate the physical characteristics of Saturn and its immediate environment.

The Pioneer Venus multiprobe spacecraft investigated the characteristics of the Venusian atmosphere down to the lowest scale height above the surface.

The Bus was retarded after the probes were released so that it did not enter the atmosphere until after completion of the probes' descent to the surface. In this way, the Bus acted as a frequency reference for an interferometric determination of the atmospheric wind effects on the probes during their descents.

The objectives of the Orbiter spacecraft were to conduct investigations of the characteristics of the upper atmosphere of Venus and the region about the planet. Additionally, the spacecraft performed radar altimetry and imaging of the planetary surface.

F. Helios Program

The objective of this mission was to place two solar orbiting spacecraft in highly elliptical orbits to achieve a perihelion of 0.3 AU and aphelion of 1.0 AU. With these trajectories the spacecraft were able to study the properties of the Sun at close range, and enable better understanding of the Sun's influence upon the Earth. One of the spacecraft is still active after 7 years in a changing thermal and radiation environment. This Program is a joint space venture between the Federal Republic of West Germany and the United States of America.

G. Apollo Program

This manned spacecraft mission was able to place the first men on the lunar surface. The DSN had a secondary role to the prime NASA tracking network, and was able to help support the Apollo 8 through Apollo 17 Missions.

H. Viking Program

The primary objectives of the Viking spacecraft were to study the planet Mars from orbit and the surface by the use of two Orbiters and two Landers. This was done while the Vikings took more than 10,000 pictures from orbit and the surface; conducted a search for microbial life; performed organic and mineralogical studies of the Martian soil; studied physical and magnetic properties of the soil; made daily weather reports and listened for seismic activity. An extended mission known as the Lander Monitor Mission (LMM) is still in operation. The primary objectives of the LMM are to continue radio science experimentation using Lander 1 as a radio source on Mars, to continue to monitor Mars' meteorology and to continue periodic picture taking of Martian terrain around Lander 1.

I. Voyager Program

The primary objectives of the Voyager Mission were to conduct exploratory investigations of the Jupiter and Saturn planetary systems and the interplanetary medium between Earth and Saturn. This was accomplished by two launches in 1977 on flyby trajectories that employ a Jupiter's gravitational assist to reach Saturn. The primary science objectives were to conduct comparative studies of the planetary systems of Jupiter and Saturn, including their environment, atmosphere, surface, and body characteristics. Additional objectives included the investigation of one or more satellites of each planet, the nature of Saturn's rings, and the interplanetary and interstellar media throughout the cruise phase of the mission. The Voyager Mission designs included one spacecraft, Voyager 2, which is using Saturn's gravitational assist to go on to a Uranus and a Neptune flyby.

III. Summary

All space flight missions previously described in this article are summarized in Table 1.

Table 1. Space flights supported by the Deep Space Network

Mission	Launch date	Objective	Results
Ranger 1	23 Aug 61	Lunar flyby	Decayed in Earth orbit
Ranger 2	18 Nov 61	Lunar flyby	Decayed in Earth orbit
Ranger 3	26 Jan 62	Soft land seismometer	Passed within 22,862 miles
Ranger 4	23 Apr 62	Soft land seismometer	Impacted on backside
Ranger 5	18 Oct 62	Soft land seismometer	Passed within 450 miles
Ranger 6	30 Jan 64	Lunar photo-impact	TV system failed
Ranger 7	28 Jul 64	Lunar photo-impact	Returned 4316 photos
Ranger 8	17 Feb 65	Lunar photo-impact	Returned 7137 photos
Ranger 9	21 Mar 65	Lunar photo-impact	Returned 5814 photos
Surveyor 1	30 May 66	Lunar soft landing	Successful engineering flight; over 11,000 photos
Surveyor 2	20 Sep 66	Lunar soft landing	Failed due to vernier engine
Surveyor 3	17 Apr 67	Lunar soft landing	Made 3-bounce landing, measured surface bearing; 6326 photos
Surveyor 4	14 Jul 67	Lunar soft landing	Lost during retro maneuver
Surveyor 5	8 Sep 67	Lunar soft landing	Provided soil analysis; over 19,000 photos
Surveyor 6	7 Nov 67	Lunar soft landing	Performed first lateral hop; over 30,000 photos
Surveyor 7	7 Jan 68	Lunar soft landing	Scientific exploration of a highland region; 21,038 photos
Lunar Orbiter 1	10 Aug 66	Equatorial orbit	Photographed complete equatorial belt of Moon for Apollo. First Earth pictures from deep space
Lunar Orbiter 2	6 Nov 66	Equatorial orbit	
Lunar Orbiter 3	5 Feb 67	Equitorial orbit	
Lunar Orbiter 4	4 May 67	Polar orbit	Photographed approximately 98% of lunar surface
Lunar Orbiter 5	1 Aug 67	Polar orbit	
Mariner 1	22 Jul 62	Venus flyby	Destroyed by range safety officer
Mariner 2	27 Aug 62	Venus flyby	Passed within 21,594 miles
Mariner 3	5 Nov 64	Mars photo flyby	Shroud failed to separate
Mariner 4	28 Nov 64	Mars photo flyby	Returned 22 photos
Mariner 5	14 Jun 67	Venus flyby	Obtained atmospheric, ionospheric, other data
Mariner 6	24 Feb 69	Mars flyby	Studied surface and atmosphere: returned TV images
Mariner 7	27 Mar 69	Mars flyby	Studied surface and atmosphere: returned TV images
Mariner 8	8 May 71	Mars orbiter	Failed to achieve Earth orbit
Mariner 9	30 May 71	Mars orbiter	Mapped nearly all of planet's surface; determined landing sites for Viking
Mariner 10	3 Nov 73	Venus/Mercury flyby	Studied clouds of Venus, returned TV images of Mercury: first to use gravity of one planet as aid in reaching another

Table 1 (contd)

Mission	Launch date	Objective	Results
Pioneer 6	16 Dec 65	Investigation of interplanetary environment	Obtained data on solar flares, solar wind, interplanetary particles and fields
Pioneer 7	17 Aug 66	Investigation of interplanetary environment	Obtained data on solar flares, solar wind, interplanetary particles and fields
Pioneer 8	13 Dec 67	Investigation of interplanetary environment	Obtained data on solar flares, solar wind, interplanetary particles and fields
Pioneer 9	8 Nov 68	Investigation of interplanetary environment	Obtained data on solar flares, solar wind, interplanetary particles and fields
Pioneer 10	2 Mar 72	Jupiter flyby	Studied Jovian system, asteroid belt, and heliosphere
Pioneer 11	5 Apr 73	Jupiter-Saturn flyby	Made additional studies of Jovian system; reached Saturn with assist from Jupiter's gravity
Pioneer 12	20 May 78	Venus Orbiter	Studied Venusian atmosphere from orbit
Pioneer 13	8 Aug 78	Venus atmosphere probes	Studied Venusian atmosphere via 4 decending probes and instrumented carrier
Helios 1	10 Dec 74	Heliocentric orbiter	Studied Sun from an orbit near center of solar system
Helios 2	16 Jan 76	Heliocentric orbiter	Studied Sun from an orbit near center of solar system
Apollo 8	21 Dec 68	Manned circumlunar flight	Command-service module orbit of Moon. Returned TV pictures of surface
Apollo 9	3 Mar 69	Manned Earth orbiter	First flight of lunar module. First Apollo EVA, live TV
Apollo 10	18 May 69	Manned circumlunar flight	First lunar module orbit of Moon. First color TV from space
Apollo 11	16 Jul 69	Manned lunar lander	First landing. Obtained surface samples, performed EVA and surface experiments, live TV
Apollo 12	14 Nov 69	Manned lunar lander	Second landing. Placed experiments package on surface, returned parts from Surveyor 3, obtained surface samples
Apollo 13	11 Apr 70	Manned lunar lander	Service module oxygen tank rupture. Crew returned safely to Earth after flight around Moon
Apollo 14	31 Jan 71	Manned lunar lander	Third landing. Returned surface samples, performed experiments
Apollo 15	26 Jul 71	Manned lunar lander	Fourth landing. First use of Rover vehicle, obtained surface samples
Apollo 16	16 Apr 72	Manned lunar lander	Fifth landing. Obtained surface samples, performed experiments, explored with Rover vehicle

Table 1 (contd)

Mission	Launch date	Objective	Results
Apollo 17	7 Dec 72	Manned lunar lander	Sixth landing. Obtained surface samples, performed experiments, explored with Rover vehicle
Viking 1 Orbiter	20 Aug 75	Mars Orbiter	Studied Martian surface and atmosphere from orbit; relayed Viking Lander data to Earth
Viking 2 Orbiter	9 Sep 75	Mars Orbiter	Studied Martian surface and atmosphere from orbit; relayed Viking Lander data to Earth
Viking 1 Lander	20 Aug 75	Mars Lander	Studied surface conditions; analyzed soil; returned TV images of landscape
Viking 2 Lander	9 Sep 75	Mars Lander	Studied surface conditions; analyzed soil; returned TV images of landscape
Voyager 1	20 Aug 77	Jupiter/Saturn flyby	Studied two planetary systems; returned TV images including Jupiter's Red Spot, Saturn's rings, and many satellites
Voyager 2	5 Sep 77	Jupiter-Saturn flyby	Studied two planetary systems; returned TV images including Jupiter's Red Spot, Saturn's rings, and many satellites

Helios Mission Support

A. L. Berman and C. T. Stelzried
TDA Mission Support Office

B. L. Seidel
Radio Frequency and Microwave Subsystems Section

J. C. Nash and R. E. Nevarez
Control Center Operations Section

This article describes ongoing Deep Space Network support of the Helios 1 spacecraft. In addition, planning for a Solar Corona Faraday Rotation Experiment during the December 1981 14th Helios 1 perihelion and subsequent solar conjunction phase is detailed.

I. Introduction

The Helios Mission, a cooperative effort of the Federal Republic of West Germany and the United States of America, was initiated to study the properties of the Sun via spacecraft measurements at close range. Two Helios spacecraft were launched; Helios 1 on December 10, 1974 (Ref. 1) and Helios 2 on January 15, 1976 (Ref. 2). Helios Mission support through 1978 was regularly documented in the TDA Progress Report (Ref. 3). On March 21, 1980, the Helios 2 spacecraft suffered a failure of the traveling wave tube amplifier, and (essentially) no useful data could be salvaged, although periodic attempts to communicate with and acquire data from Helios 2 were made until January 8, 1981, at which time the spacecraft transmitter was commanded off. On the other hand, the Helios 1 spacecraft continues in reasonably good health, and has been regularly in communication with the Deep Space Network (DSN) until the present time. This article describes recent DSN support of Helios 1, and, in particular, describes planning for a December 1981 Helios 1 Faraday Rotation Experiment.

II. Helios 1 Support

During 1981, Helios 1 was supported by the German Weilheim tracking station, and by (primarily) the 26-m DSN stations at Goldstone, California (DSS 11) and Honeysuckle Creek, Australia (DSS 44). During this period, important inner solar system science data were generated by onboard Helios 1 science instruments. In turn, these data are being correlated with science measurements from other spacecraft, such as the Voyagers, Pioneers, and ISEE-3, to further study such topics as the modulation of cosmic radiation with solar cycle, the observation of coronal mass ejection events from the solar limb, and the triangulation of Types III and IV solar events (Ref. 4). During 1981, which is marked by the beginning phase of the decline of solar activity during the 21st solar cycle, interesting phenomena observed in Helios 1 science data included magnetic bubbles, short periods of rapid decline in solar wind intensity, and the appearance of simple ionized helium (Ref. 4).

The 12th perihelion of Helios 1 occurred on December 12, 1980, and the 13th on June 13, 1981. The 14th perihelion passage will occur on December 20, 1981, with a solar conjunction phase immediately thereafter, and this opportunity will be utilized to perform a Faraday rotation radio science experiment with the Helios 1 signal and the DSN 64-m subnetwork.

III. Faraday Rotation Measurements in the Solar Corona

In November 1968, the Pioneer 6 spacecraft was occulted by the Sun. The Pioneer 6 spacecraft transmitted a linear polarized carrier, which allowed the first experiment to be performed using a man-made signal source in determining Faraday rotation through the solar corona (Ref. 5). The quasilongitudinal approximation for Faraday rotation is given by (Ref. 6):

$$\Omega = Qf^{-2} \int N_e B_l dR$$

where

Ω = Faraday rotation, deg

f = signal carrier frequency, Hz

$Q = 1.3548 \times 10^6$

R = signal path, m

N_e = electron density, m^{-3}

B_l = solar longitudinal component of magnetic field, tesla

Therefore, measurement of coronal-induced Faraday rotation provides information about both electron density and the solar magnetic field (Ref. 7). To support this class of experiment, the 64-m subnetwork was equipped with remotely rotatable, microwave linear feeds (Ref. 8). Closed-loop polarimeters (Ref. 9) were implemented and are used to automatically measure the orientation of the received signal polarization. This system maximizes the received signal strength and yields precise signal polarization angle data.

Research using the polarization measurement capability at DSS 14, 43, and 63 continues with the Helios spacecraft; Volland et al. (Ref. 10) and Bird et al. (Ref. 11) have reported Faraday rotation observations from the solar occultations of Helios in 1975. More recently, Dennison et al. (Ref. 12) have expanded on these results with a measurement of the gravitational deflection of polarized signal radiation propagating through the solar corona.

IV. Helios 1 Faraday Rotation Experiment Planning

In previous Helios Faraday rotation experiments (Refs. 10, 11, 12), heavy coverage requirements of other flight projects prevented the Helios Project from obtaining continuous coverage during the experiment period, causing sizeable gaps in the data and thereby somewhat hampering scientific analysis and interpretation of the data because of possible 180° ambiguities. In the upcoming 14th perihelion passage and subsequent solar conjunction, the geometry is such as to cause the solar conjunction phase to be compressed into a rather short period; Figs. 1, 2, and 3 detail the perihelion passage and subsequent solar conjunction geometry. In addition, total flight project coverage requirements on the 64-m subnetwork during December 1981 are light by historical standards. The fortuitous combination of these circumstances allowed Helios 1 to obtain nearly continuous scheduled coverage on the 64-m subnetwork from day of year (DOY) 353 at an ingoing Sun-Earth-Probe Angle (SEP) of 4.1 degrees, to DOY 359, at an outgoing SEP angle of 3.8 degrees. The schedule of tracks planned at the 64-m subnetwork in support of this experiment are listed in Table 1. Demonstration passes for this experiment were conducted as follows:

DSS 14: DOY 344 and 348
DSS 43: DOY 338 and 339
DSS 63: DOY 335 and 337

References

1. Berman, A. L., and Bright, L. E., "Tracking Operations During the Helios 1 Launch Phase," in *The Deep Space Network Progress Report 42-28*, pp. 83-94, Jet Propulsion Laboratory, Pasadena, Calif., Aug. 15, 1975.

2. Bright, L. E., "Tracking Operations During the Helios 2 Launch Phase," in *The Deep Space Network Progress Report 42-32*, pp. 262-276, Jet Propulsion Laboratory, Pasadena, Calif., April 15, 1976.

3. Jensen, W. N., and Nash, J. C., "Helios Mission Support," in *The Deep Space Network Progress Report 42-49*, pp. 43-44, Jet Propulsion Laboratory, Pasadena, Calif., Feb 15, 1979.

4. Heftman, K., private communication.

5. Stelzried, C. T., *A Faraday Rotation Measurement of a 13 cm Signal in the Solar Corona*, Technical Report 32-1401, Jet Propulsion Laboratory, Pasadena, Calif., July 15, 1970.

6. Stelzried, C. T., Levy, G. S., Sato, T., Rusch, W. V. T., Ohlson J. E., Schatten, K. H., and Wilcox, J. M., "The Quasi-Stationary Coronal Magnetic Field and Electron Density as Determined From a Faraday Rotation Experiment," in *Solar Physics, 14*, pp. 440-456, 1970.

7. Rusch, W. V. T., and Stelzried, C. T., "Net-field Polarization in a Magnetically Biased Plasma, in *Radio Science, 7*, pp. 1131-1141, 1972.

8. Reid, M. S., Clauss, R. C., Bathker, D. A., and Stelzried, C. T., "Low-Noise Microwave Receiving Systems in a Worldwide Network of Large Antennas," in *Proceedings of the IEEE, 61*, pp. 1330-1335, 1973.

9. Ohlson, J. E., Levy, G. S., and Stelzried, C. T., "A Tracking Polarimeter for Measuring Solar and Ionospheric Faraday Rotation of Signals from Deep Space Probes," in *IEEE Transactions Instrumentation and Measurements, IM-23*, pp. 167-177, 1974.

10. Volland, H., Bird, M. K., Levy, G. S., Stelzried, C. T., and Seidel, B. L., "Helios-1 Faraday Rotation Experiment: Results and Interpretations of the Solar Occultations in 1975," in *Journal of Geophysics, 42*, pp. 659-672, 1977.

11. Bird, M. K., Volland, H., Stelzried, C. T., Levy, G. S., and Seidel, B. L., "Faraday Rotation Transients Observed During Solar Occultation of the Helios Spacecraft," in *Study of Traveling Interplanetary Phenomenon*, pp. 63-74, D. Reidel, Dordrecht, Holland, 1977.

12. Dennison, B., Malnick, G., Harwit, M., Sato, T., Stelzried, C. T., and Jauncey, D., "Deflection of Polarized Radiation: Relative Phase Delay Technique," in *Nature, 273*, pp. 33-35, 1978.

Table 1. Planned Helios 1 64-m subnetwork coverage

Day of year, 1981	DSS	Pre-calibration, Z	Post-calibration, Z	Acquisition of signal, Z	Loss of signal, Z
352	43	16:55	08:40	19:05	08:10
353	63	08:00	16:20	09:30	15:50
353	14	13:15	00:00	15:15	23:25
353	43	22:15	08:50	23:45	08:20
354	63	06:45	16:25	08:15	15:55
354	14	13:25	00:15	15:25	23:45
354	43	17:20	08:50	19:20	08:20
355	63	06:50	16:30	08:20	16:00
355	14	13:35	18:30	15:35	18:00
356	63	10:00	16:40	12:00	16:10
356	14	13:40	00:35	15:40	00:05
356	43	17:30	09:10	19:30	08:40
357	63	06:35	16:30	08:35	16:15
357	14	13:45	00:50	15:45	00:20
357	43	17:40	09:20	19:40	08:50
358	63	06:40	16:50	08:40	16:20
358	14	13:50	00:50	15:50	00:20
358	43	22:20	09:25	23:50	08:55

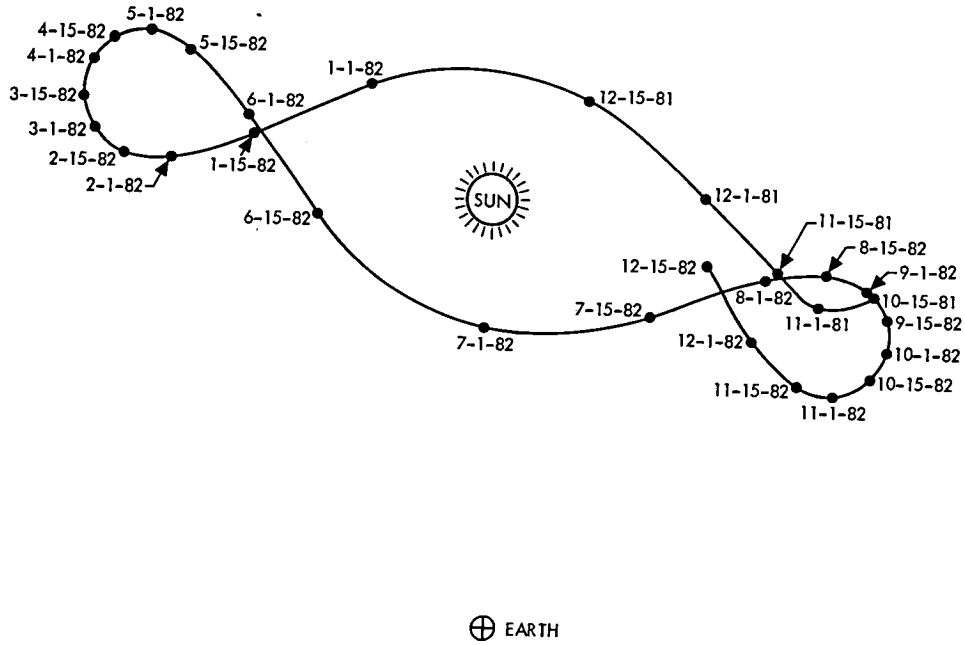

Fig. 1. 1981–1982 Helios 1 position in the ecliptic plane assuming a fixed Earth-Sun line

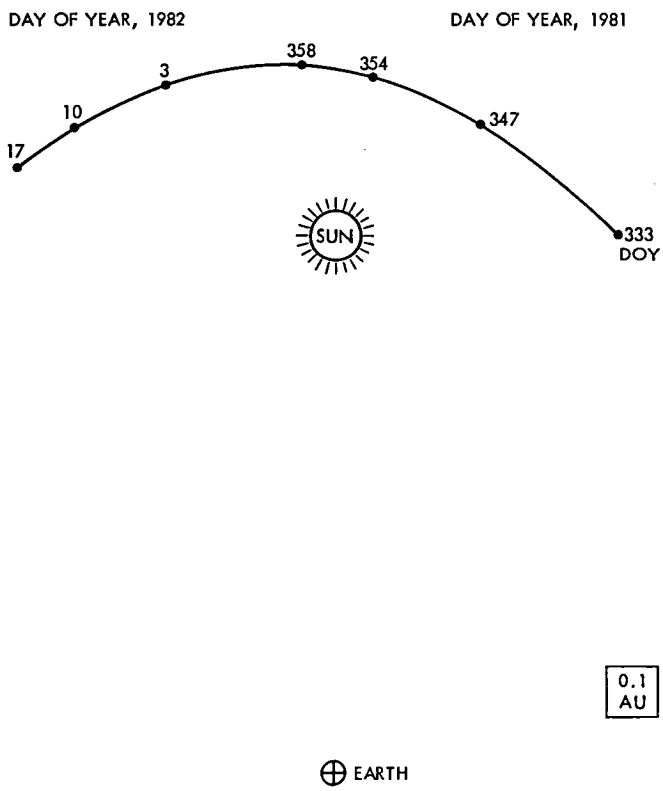

Fig. 2. 14th perihelion and subsequent solar conjunction phase of Helios 1 in the ecliptic plane assuming a fixed Earth-Sun line

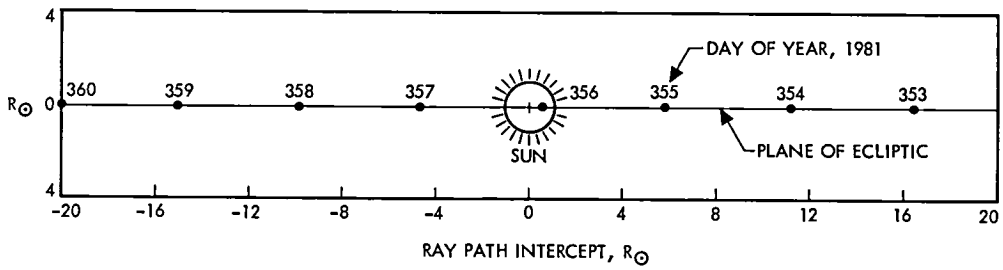

Fig. 3. Solar conjunction phase of Helios 1 ray path intercept in the plane perpendicular to the ecliptic plane and Sun-Earth line

The Development of a Magnetically Enhanced Hydrogen Gas Dissociator

L. Maleki and T. K. Tucker
Communications Systems Research Section

Application of a dc magnetic field on an rf hydrogen gas dissociator has led to the development of a more efficient source of atoms for hydrogen masers. We discuss the influence of the applied magnetic field on the plasma and some details of the resulting enhancement of the dissociation efficiency. We also consider the ways that this improved efficiency can result in the enhancement of the operation and field life of hydrogen masers, as well as aid the development of spaceborne masers.

I. Introduction

The development of an rf hydrogen gas dissociator, efficient in both atom production and power consumption, is of great interest in hydrogen maser research and development. The significance of a low-powered source for spaceborne masers is self evident: it reduces the power requirement for the operation of the maser and aids the power economy in the spacecraft. In ground-based masers, an efficient source can contribute to a more reliable operation as well as extended operational life.

The details of the influence of the rf dissociator on the operation of the hydrogen maser have been previously discussed (Ref. 1). Briefly, the dissociator produces atoms that, upon their exit through a multichannel collimator, form an atomic beam of hydrogen. The beam enters the inhomogeneous field of a state selecting magnet which focuses atoms in a particular hyperfine sublevel into the entrance of a storage bulb within the maser high-Q cavity. The stored atoms interact with the microwave field coupled to the cavity, and undergo stimulated emission.

The efficiency of the dissociator in atom production can then affect the operation of the maser in three important ways. First, since the state selecting magnet cannot alter the path of undissociated molecules which exit the collimator, a significant number may enter the storage bulb in the cavity. The presence of the molecules in the storage bulb, the number of which depends on dissociation efficiency, contributes to collisional line broadening of the hydrogen line. Second, the required back pressure of the hydrogen gas for production of a useful flux of atoms, as determined by the source efficiency, constitutes the load on the vacuum pumps. The vacuum pump saturation and the resulting decrease in their hydrogen capacity is a frequently encountered mode of maser failure. Finally, parameters of pressure and input power directly influence the operational life of the dissociator itself. The failure of the hydrogen gas dissociator is also an often encountered mode of maser failure.

Motivated by the above consideration, we undertook to improve the operational efficiency of the rf hydrogen gas dissociator (source), based on an initial study of the rf plasma

processes (Ref. 1). Here we report on the development of an rf hydrogen source which is capable of producing atoms with an efficiency comparable to conventional sources, but which consumes a significantly lower input rf power. This source can also operate in a low pressure mode, where the efficiency in atom production is improved, while the power is kept constant. The improvement in the source performance is obtained by the application of a dc magnetic field on a conventional rf dissociator.

In Section II of this paper we discuss theoretical background and the relevant concepts for this atom source. Section III presents some details of the source and its operation. Finally, a summary is given in Section IV, together with an outline of recommended future work.

II. Theory

Molecular dissociation in an rf plasma is due to the collision of molecules with electrons that move under the influence of the applied rf field. The rf field is coupled to the source in a capacitive or an inductive mode. In inductively coupled schemes, as employed in JPL masers, the motion of electrons may be regarded as circular motion about the axis of the oscillating magnetic field. These electrons transfer their energy to particles in the plasma through inelastic collisions and are eventually lost to the walls of the source or to recombination processes with positive ions. The efficiency of atom production in the rf source is therefore related to the energy of the electrons, as well as their collisional frequency with hydrogen molecules. The energy of the electrons is determined by the power input, while their collision frequency is related to molecular density via the pressure in the source. It is, however, undesirable to increase the power input or the source pressure in order to improve the efficiency of the atom production. An increase in the power, which is undesirable for spaceborne maser application, is responsible for generation of ions with higher energies. As the energetic ions collide with the glass wall, they cause sputtering, which then results in an increase in the recombination rate of hydrogen atoms on the walls. With a gradual degradation of the glass walls, the operational life of the source is degraded accordingly. As for the increase in the number density of molecules by increasing the pressure, we have already mentioned the desirability of a reduced gas load to the vacuum pumps, as well as a reduced molecular density in the storage bulb.

Consider, however, the motion of an electron in an rf plasma which is superimposed by an axial dc magnetic field. The electron will experience a force $\mathbf{F} = e\mathbf{v} \times \mathbf{B}$, where $\mathbf{v}$ is the electron velocity and $\mathbf{B}$ is the magnetic induction. This implies that the path of electrons would be modified through the action of the field on the component of velocity perpendicular to it. The result is that the electron will circulate the field with Larmor frequency $f = eH/2\pi mc$, while its parallel motion is unaffected by the field. Here H is the magnetic field, m is the mass of the electron, and c the velocity of light. The helical motion of the electron thus modified constitutes a lengthening of its path in the plasma, as compared to its path in the absence of the magnetic field. Furthermore, the circulating electron in the dc field can now absorb energy in resonance from the field as it moves in the direction of the field, when its cyclotron frequency $\omega_c = eH/mc$ is equal to the frequency of the oscillating field ω.

In this manner, it is possible to increase the efficiency of atom production in the rf dissociator by the application of the magnetic field. It should be mentioned that dc magnetic fields have been previously applied to rf plasmas used for production of positive ions (Ref. 2). While small dc fields do not directly affect the path of ions due to ions' relatively large mass, they significantly modify the drift of ions in the plasma (Ref. 3). It is the modification of ion drift that primarily contributes to improved performance of rf ion sources with axial dc magnetic fields. Furthermore, because of the general dependence of the ionization cross-section on energy (Ref. 4), increased electron energy due to the applied dc field directly improves ion production in rf ion sources, an effect that is not necessarily desirable in molecular dissociation. It is therefore quite important to keep in mind that the influence of a dc magnetic field on the efficiency of atom production in rf dissociators is significantly different from its influence on ion current production in rf ion sources.

III. The Source and Its Operation

Because the hydrogen gas dissociator assembly of JPL masers is inside the vacuum package and therefore not accessible without breaking of vacuum, a dissociator test bed was constructed. The test bed consists of a vacuum canister for connecting an ion pump to a source mating flange. A pyrex glass bulb was designed and constructed with dimensions identical to those of conventional sources used in JPL masers, but suitably modified for use in the test bed. The modification consists of a glass ring with an O-ring groove externally attached to the wall of the source containing the exit collimating holes. The source may then be positioned on the flange with the O-ring providing the necessary vacuum seal. The rf exciter coil assembly and hydrogen gas feed lines provide the necessary support for the glass bulb. A picture of the test bed and the source is given in Fig. 1.

For the generation of the dc magnetic field a solenoid was constructed from an insulated copper wire wound on a copper

cylinder with an inside diameter one inch larger than the diameter of the dissociator bulb. The solenoid was placed on the mating flange in a coaxial configuration with the source. This particular solenoid provided a maximum field of 145 gauss on its axis with a 2.0-A current input. The solenoid produced a field which was linearly dependent on current within the range of zero to 2.0-A, the maximum current which the power supply produced.

The dissociation efficiency of the source was determined by measuring the changes in the pressure observed when the plasma was on or off. The variation of the pressure was obtained by noting the current in the ion pump power supply. While this method of efficiency determination for the dissociation lacks a high absolute accuracy, it does provide a satisfactory means for a relative determination of the dissociator efficiency.

The source was initially operated under the condition of power and pressure similar to those employed in the maser. A back pressure of hydrogen gas produced a pressure of 200 m torr in the dissociator; an rf power input of 3 W produced an efficiency measured to be 5%. As the input power was decreased, the efficiency of the source deteriorated, and the plasma was not sustained if the power was reduced below 2 W. The source was left to operate under normal operating conditions for a period of a few days to allow its performance to stabilize. After this period, the solenoid power supply was turned on and the solenoid current was varied between zero and 2 A. As the magnetic field was increased, the light intensity of the plasma increased significantly. Furthermore, for specific values of the field a change in the plasma mode was observed. A measurement of the efficiency of the source at this level of pressure and power was performed with the dc magnet on. The source exhibited an increase and a decrease in efficiency depending on the magnitude of the applied magnetic field. The amount of variation in the efficiency ranged from a 10% increase to a 10% decrease of the efficiency measured without the applied magnetic field.

The efficiency measurements were continued as the input rf power was decreased. First it was observed that the application of the magnetic field decreased the value of the minimum power required for maintaining a plasma, depending on the current in the solenoid. For a current of 0.4 A corresponding to a field of approximately 40 gauss, it was possible to reduce the power to about 0.3 W. With these parameters, the efficiency of the source was determined to be 5%, the same value as the efficiency of a conventional source operating with 3 W of input rf power. The dc magnetic field then resulted in a tenfold decrease in the power consumption.

This result could be predicted in the following way. At a given value of pressure, a specific level of input power yields the optimum efficiency. A decrease in this power level would decrease the efficiency, while an increase in the level does not necessarily lead to increased efficiency because of the difference in the dissociation energy of the hydrogen molecule (4.8 eV) and its ionization potential (15.8 eV). While the dissociation and ionization of the molecule constitute competing processes in the rf plasma, an increase in the average energy of electrons, with a Maxwellian energy distribution in the plasma, contributes preferentially to the ionization process, rather than the desired dissociation of the molecules. Therefore increasing power from the optimal level may in fact decrease the dissociation efficiency by contributing to the ionization process, via the increase in the energy of electrons. Conversely, when the power is decreased from the optimum level, an appropriate magnetic field strength can enhance the dissociation by allowing the electrons circulating with cyclotron frequency to absorb energy in resonance with the field and regain the condition of optimal energy for maximum dissociation efficiency.

Based on this consideration, we decided to investigate the influence of an inhomogeneous field on the efficiency of the source. We reasoned that if the energetic electrons in the high energy tail of the Maxwellian distribution could be swept away from the region near the exit of the source, a larger number of electronic collisions with the molecules will result in dissociation in that region, rather than the competing ionization. A test of this reasoning was demonstrated by distorting the homogeneity of the magnetic field through positioning the axis of the solenoid away from the axis of the source. When the solenoid was positioned with its axis about 1/2 inch away from the source axis, an increase in the dissociation was observed for a 200-m torr pressure of hydrogen. With a decrease in the pressure to 80 m torr, the measured dissociation efficiency of the source increased from a 7% level to 12.8% when a current of 0.75 A was applied to the solenoid; this is a 70% increase of the dissociation efficiency. The power level in both cases was 2.5 W.

While the configuration of the inhomogeneous field was somewhat arbitrary, determined by the constraint of the existing setup, it clearly demonstrated the potential value of this approach in designing a highly efficient source. It should be mentioned, however, that such a design should include consideration of influence of the inhomogeneous magnetic field on the production of secondary electrons released by particle impact with the walls. These electrons participate in plasma processes and influence the parameters of the rf plasma.

IV. Summary and Conclusion

The development of a dc magnetic field to the rf dissociation has yielded the following results:

(1) For a specific value of the magnetic field, it is possible to maintain the efficiency of the source and yet decrease the rf power input by an order of magnitude. This conclusion is of significance to both spaceborne maser development and improved reliability of ground-based masers through the expected improvement in the source life.

(2) It is possible to obtain good efficiency for the source and, at the same time, reduce the hydrogen pressure with an applied dc magnetic field. This finding implies a means for the reduction of the gas load to the maser vacuum pumps, thereby increasing their operational life, and reducing the frequency of maser breakdowns resulting from pump failures.

(3) The results with the inhomogeneous field indicate that it is possible to design a magnetic field configuration to sweep energetic electrons away from the region near the source exit. This would increase the source efficiency by preferential dissociation of the molecules, as compared to the competing process of molecular ionization.

(4) The application of a magnetic field on the rf plasma results in a significant increase of the light output from the plasma. While this effect is not of interest to maser application (except for reaffirming that there is no direct relationship between the efficiency of the source and the intensity of the emitted plasma light) it may be of significance in other applications. In particular, certain light sources such as mercury ion light source, and rubidium light source, employ rf power for excitation. An application of a dc magnetic field can improve the performance of those sources and extend their operational life.

The investigation of the performance of the source was determined in a test bed and by obtaining the dissociation efficiency through the measurement of pressure variations. It is obvious that it would be highly desirable, and necessary, to perform the tests using a hydrogen maser. In this way, the extent of improvement obtained with the new source in relation to the maser vacuum system, power output, and line Q may be directly determined. Efforts are presently underway to design and construct a source unit which may be mounted externally to our existing maser test assembly. We intend to optimize the configuration and the strength of the magnetic field for a desirable mode of source and maser operation. Once this is accomplished, we will substitute equivalent permanent magnets for the solenoid, thereby eliminating the need for a solenoid power source. Finally, we intend to test the influence of the magnetic field on the light output of mercury lamps, which will be utilized in a trapped mercury ion frequency source. The results of this investigation will be reported in a later paper.

References

1. Maleki, L., "A Study of the Processes in the RF Hydrogen Gas Dissociator," in *The TDA Progress Report 42-59: July and August 1980*, Jet Propulsion Laboratory Pasadena, Calif., Oct. 15, 1980.

2. Vali, L., *Atom and Ion Sources*, Chapter III, John Wiley and Sons, New York, 1977.

3. Francis, G., *Ionization Phenomena in Gases*, Chapter IV, Butterworths Scientific Publications, London, 1960.

4. Kieffer, L. J., and Dunn, Gordon H., *Rev. Mod. Phys., 38*, 1 (1966).

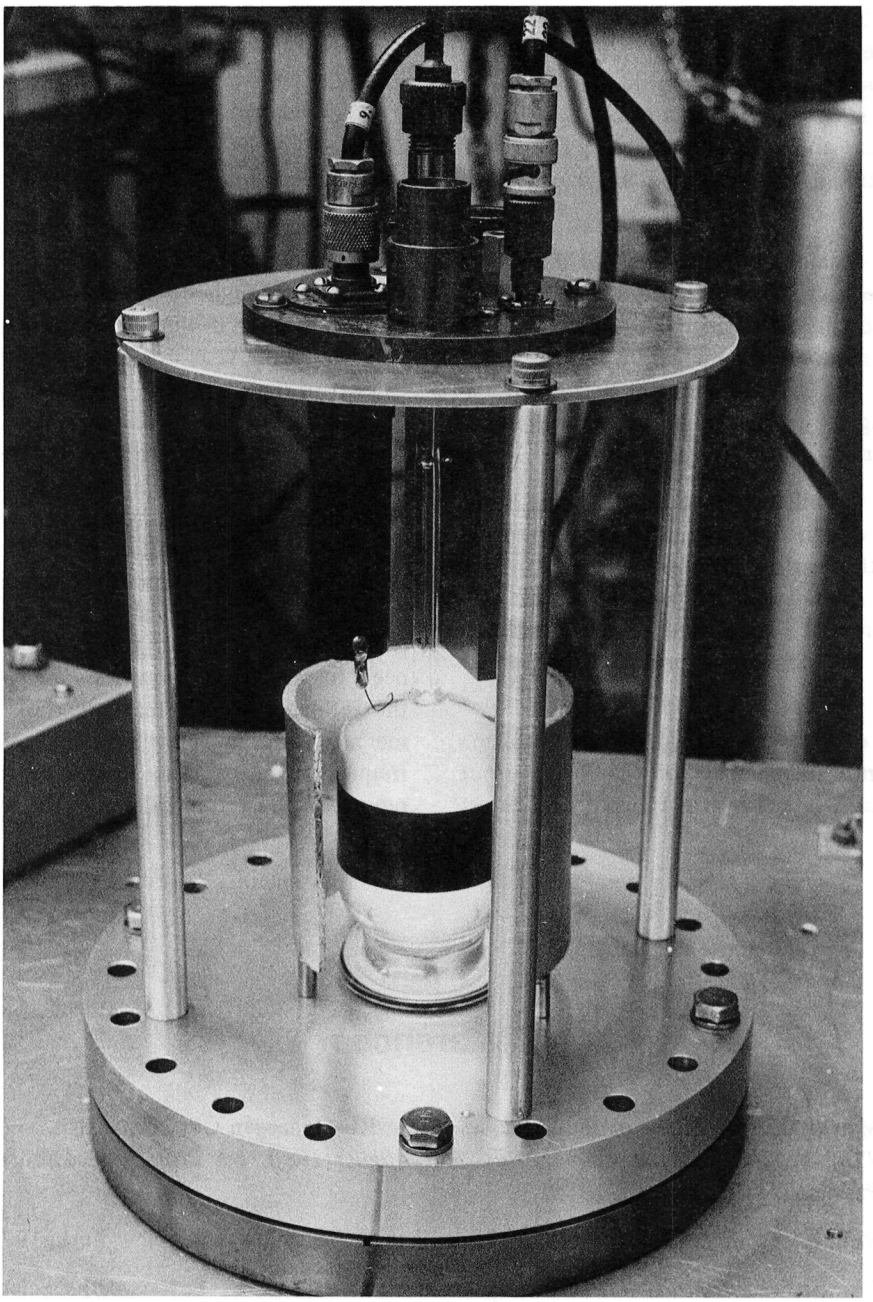

Fig. 1. Hydrogen gas dissociator installation on test bed

Magnetic Refrigeration for Maser Amplifier Cooling

D. L. Johnson
Radio Frequency and Microwave Subsystems Section

The development of a multifrequency upconverter-maser system for the DSN has created the need to develop a closed-cycle refrigerator (CCR) capable of providing more than 3 watts of refrigeration capacity at 4.5 K. In addition, operating concerns such as the high cost of electrical power consumption and the loss of maser operation due to CCR failures require that improvements be made to increase the efficiency and reliability of the CCR. One refrigeration method under consideration is the replacement of the Joule-Thomson expansion circuit with a magnetic refrigerator. Magnetic refrigerators can provide potentially reliable and highly efficient refrigeration at a variety of temperature ranges and cooling powers. This paper summarizes the concept of magnetic refrigeration and provides a literature review of existing magnetic refrigerator designs which have been built and tested and that may also be considered as possibilities as a 4 K to 15 K magnetic refrigeration stage for the DSN closed-cycle refrigerator.

I. Introduction

Efficient long-life refrigeration techniques are being developed for the DSN masers to improve the present closed-cycle refrigerator technology. One area of investigation is to find an alternative to the Joule-Thomson refrigeration process in the DSN closed cycle refrigerators (CCRs). In the CCR, as in virtually all mechanical refrigerators which are capable of the liquefaction of helium, a Joule-Thomson (J-T) circuit is added to an expansion engine to serve as the final stage of cooling to produce the desired refrigeration at the liquid helium (LHe) temperatures. The J-T circuit, while having no moving parts or seals, depends critically on extreme high gas purity to obtain long-term continuous operation. In fact, a major reason for present CCR failures is due to gas impurities which plug the J-T circuit. Because the J-T circuit and the precooling expansion engine circuit are essentially independent of each other, it is important to determine whether other refrigeration cycles can be used in place of the J-T circuit which will match or surpass the J-T circuit in terms of efficiency, reliability, temperature span achievable, and ease of construction and operation. One such refrigeration mode under investigation is the cooling by adiabatic demagnetization.

Adiabatic demagnetization of a paramagnetic salt (or magnetic refrigeration) was chosen as the possible replacement for the J-T circuit due to the following potential advantages over the J-T circuit.

(1) High efficiencies are attainable (more than 70% of Carnot efficiency in comparison to 20-25% for the J-T expansion stage as measured for a DSN 1-watt CCR (Ref. 1)).

(2) The refrigeration capacity per unit volume of working material is large as high density solids rather than the low density gases are used.

(3) Potential high reliability can be expected since only a few slow moving parts are required.

(4) The paramagnetic material is relatively inexpensive (e.g., gadolinium gallium garnet costs about $225/lb).

There are several disadvantages which must also be considered.

(1) The need for a high field superconducting magnet that must be maintained at liquid helium temperatures.

(2) Stray magnetic fields which will require shielding to protect the maser.

(3) The use of low temperature seals for moving parts.

The development work on cyclic magnetic refrigeration to date has shown great promise for its application as a viable means of providing efficient and reliable refrigeration. Their proposed uses include:

(1) Laboratory material studies in the μkelvin range through adiabatic demagnetization of the salt pill's nuclear spins (Ref. 2.).

(2) Spacecraft operations to cool detectors and instruments (Refs. 3, 4).

(3) Large-scale refrigeration for superconductivity application in power generation and transmission (Ref. 5).

(4) Complete magnetic refrigeration systems operating between 300 K and 20 K (or 4 K) for the production of liquid H_2 (or liquid He) (Ref. 6).

It is interesting to note that none of the material refrigerators developed to date have been used to produce 4 K refrigeration. The major development work thus far has centered around room temperature devices where the use of superconducting magnets could be avoided, or below 4 K where a liquid helium bath could be used to submerse the superconducting magnet and also be used for the high-temperature heat reservoir.

Van Geuns (Ref. 7) first proposed the idea of a 4-15 K magnetic refrigeration stage as early as 1966 to find a more efficient alternative to the J-T circuit of a closed-cycle refrigerator. Although the results of the analysis of the proposed refrigerator indicated that the prospects for the magnetic refrigerator were promising, no follow-up experimental work has been reported in the literature to our knowledge. Since that time there have been several studies of paramagnetic materials for use in a 2-20 K temperature range (Refs. 8, 9), and there have been more proposed designs for a 4-15 K magnetic refrigerator (Refs. 10-12), but to date no experimental devices have been developed.

In the next section, the concept of magnetic refrigeration will be described and possible thermodynamic cycles available for a magnetic refrigeration stage will be introduced. A brief discussion will be made of several magnetic refrigerators that have been reported on in the literature and how they may be used as a 4-20 K refrigerator stage for use in a DSN CCR. We will also introduce some of the design constraints that must be considered if a magnetic refrigeration stage is to be used.

II. Principles of Magnetic Refrigeration

Magnetic cooling is a consequence of the fact that at a fixed temperature the entropy of a system of magnetic dipoles is lowered by the application of a magnetic field. In the absence of an external magnetic field the magnetic moments of the electron spin system are randomly oriented, with all orientations equally probable. When a magnetic field is applied, the dipole moments tend to align parallel to the field, thereby increasing order in the system, or equivalently, decreasing its entropy. In doing so the moments go into lower energy levels, giving off excess energy to the crystal lattice of the paramagnetic material in the form of a heat of magnetization. This heat energy is removed from the material by holding it in contact to a constant-temperature reservoir. Now by thermally isolating the material and removing the field isentropically, the dipoles again become randomly oriented. But in doing so, energy must be drawn out of the material's lattice, thereby lowering the temperature of the material.

The entropy-temperature diagram (or S, T-diagram) of a paramagnetic material is shown in Fig. 1. The entropy curves at several constant magnetic fields have been shown. The temperature T_0 is defined as the temperature at which the zero magnetic field entropy per mole of material is equal to $R \ln (2J + 1)$ (see Fig. 1). At temperatures above T_0, the T^3 contribution to the entropy by the lattice vibrations becomes appreciable. Below T_0 the molar entropy depends little on the lattice entropy and thus remains fairly temperature-independent until the interaction energy E of the ions becomes an appreciable fraction of the average thermal energy kT. Spontaneous ordering of the dipoles then occurs and this lowers the entropy. This can be characterized by a magnetic ordering temperature $\Phi \cong E/K$. Here the specific heat of the material also shows a pronounced maximum (since it varies as $T \cdot \partial S/\partial T$). Between Φ and T_0 the entropy of the spin system depends most strongly on the magnetic field, and in this region the adiabatic demagnetization method is most effective.

III. Thermodynamic Cycles

The concept of cyclic magnetic refrigeration can best be described with the aid of Fig. 2. In phase 1 of the cycle, thermal switch S2 is open and thermal switch S1 is closed so that the working material M is in good thermal contact with the heat reservoir R during the application of a magnetic field. This permits the heat of magnetization $Q = T\Delta S$ to be removed from the material while the temperature of the material T_M remains nearly constant at the reservoir temperature T_R. In phase 2, both thermal switches are opened to thermally isolate the working material and the field is reduced until T_M is lowered to the heat source temperature T_S. In phase 3 switch S2 is closed to permit thermal contact between the working material and the heat sources while the field is reduced to zero. Heat energy is extracted from the source while the final demagnetization is lowering T_M. This process establishes a somewhat lower source temperature T_S. Phase 4 represents the last step in the magnetic cycle. During this phase, S1 and S2 are opened to isolate the material and the field is increased until T_M is increased to T_R. The magnetic cycle can be repeated by returning to phase 1 of the cycle and again applying the full field to the working material. The temperature T_S will continue to fall with each cycle of the refrigerator until the net refrigeration of the working material is balanced out by the heat leak to the source.

The magnetic refrigerator in the above example operated on the basis of the Carnot cycle (two isothermal steps and two adiabatic steps). It is an easy cycle to execute but has a limited temperature span while requiring a large field change. Other magnetic analogs to the gas thermodynamic cycles exist which are more difficult to carry out, but they are capable of larger temperature spans while requiring smaller magnetic field changes. They are: the Stirling cycle (Ref. 6), which consists of two isothermal and two isomagnetization steps; the Ericsson cycle (Ref. 6), which consists of two isothermal and two isofield steps; and the Brayton cycle (Ref. 6), which consists of two adiabatic and two isofield steps. The four cycles are shown in Fig. 3, but they do not represent the only refrigeration cycles possible. The operation of a magnetic refrigerator based on one of these thermodynamic cycles will depend largely on the design of the refrigerator, the ease of implementation and the environment in which the refrigerator will work.

IV. Approaches to Actual Magnetic Refrigeration Devices

A. Two-Switch Devices

It was the Nobel prize winning work of Giauque and MacDougall (Ref. 13) in 1933 which demonstrated the idea of magnetic refrigeration to cool from 3.5 to 0.5 K. Subsequent magnetic refrigeration work was able to produce temperatures to below 1 mK. Until recently, the method of adiabatic demagnetization was limited to so-called "one-shot operations" where the paramagnetic material was isothermally magnetized and followed by an adiabatic demagnetization to obtain temperatures below 1 mK for limited periods of time.

In 1954 Heer et al. (Ref. 14) developed the first magnetic refrigerator to operate in a continuous mode to provide a fairly constant low temperature. The device used superconducting thermal valves (as diagrammed in Fig. 1) and a high heat capacity material for the low-temperature reservoir to smooth out the low-temperature fluctuations. This refrigerator was capable of producing 7 μW of refrigeration at 0.26 K. Arthur D. Little, Inc. commercially marketed a few magnetic refrigerators modeled after this design (Ref. 15) until ^{3}He became commercially available in sufficient quantities to use as a refrigerant in this temperature range.

The next refinement was by Zimmerman et al. (Ref. 16) in 1962, by using a superconducting solenoid. This refrigerator was capable of producing 100 μW of refrigeration at 0.26 K. More recently Rosenblum et al. (Ref. 17) used a similar device to produce 0.1 μW of refrigeration at the much lower temperature of 10 mK. All of these refrigerators were low power devices and limited to temperatures below 1 K because of the superconducting switches used. Steyert (Ref. 12) recently proposed a 2-10 K refrigerator which uses magnetoresistive switches (Ref. 18) with large switching ratios to produce several watts of refrigeration at 2 K using a Carnot cycle. No such refrigerator has been built to date.

B. Reciprocating Devices

The reciprocating magnetic refrigerator requires the complex movement of two of the following components: the magnet, the magnetic material, or the regenerator fluid. Described simply, the working material passes through the regenerative column of fluid in which a temperature gradient has been established after numerous cycles. The regenerative fluid does the work of passing the heat from the heat source to the heat sink. The mixing of the fluid across the temperature gradient by the movement of the material is the key area of concern for the design of the device. An illustration of one such refrigerator (Ref. 19) is shown in Fig. 4.

Three reciprocating magnetic refrigerators have been built and tested since Van Geuns (Ref. 7) first proposed the idea of a 4-15 K reciprocating magnetic refrigeration stage to replace the J-T circuit of his closed cycle refrigerator. Brown (Ref. 19) utilized a magnetic Stirling cycle to demonstrate a 47 K temperature span between 272 and 319 K. He used gadolinium

metal as the working material which passed through a regenerative column of water and ethyl alcohol. Barclay et al (Ref. 20) used a salt pill of compressed $Gd_2(SO_4)_3 \cdot 8H_2O$ to pump heat from 2 to 4 K. Using a magnetic Ericsson cycle at a 1/60 Hz rate, they were able to develop 52 mW of refrigeration capacity at 2 K in their initial tests. Delpuech et al. (Ref. 21) built a 2 to 4 K double-acting reciprocating device in which two identical $Gd_2(SO_4)_3$ magnetic elements on a reciprocating drive shaft alternately entered and left the magnetic field. Incorporating this arrangement with a magnetic Ericsson cycle, they were able to attain 570 mW of refrigeration capacity at 2.1 K at a 0.3-Hz cycle rate. In later experiments using $Gd_2Ga_5O_{12}$ magnetic elements, they were able to achieve 1.2 W at 1.8 K with a 0.95 Hz rate (Ref. 22).

C. Rotating Wheel Devices

The wheel-concept magnetic refrigeration device uses the magnetic material to form the rim of the wheel. It has a simple axial drive but requires a more complicated magnetic field profile since one portion of the wheel must be in a large field while the opposite side must be in a low magnetic field. However, because one portion of the rim is constantly rotating into or out of the magnetic field, the wheel design does provide continuous refrigeration. Figure 5 illustrates the concepts of both a Carnot-cycle and a Stirling-cycle wheel design.

Steyert and coworkers (Refs. 5, 24) have developed several rotating wheel designs which have operated at either room temperature or between 2 and 4 K. The prototype low-temperature Carnot-cycle wheel design (Ref. 24) used $Gd_2(SO_4)_3 \cdot 8H_2O$ as the working material and was capable of pumping 0.5 W of heat from 2.75 K to the 4.2 K heat sink. The wheel rotated at 0.77 Hz. The capacity and source temperature varied with the rotation rate of the wheel.

As a feasibility study for the use of low-temperature magnetic refrigeration technology to provide refrigeration for superconducting applications in power generation and transmission, Barclay and Steyert (Ref. 5) built a room-temperature wheel with an objective of understanding the device in an experimentally convenient temperature range. Their prototype gadolinium metal wheel operated through a 1.2 tesla field change and provided 0.5 kW of continuous refrigeration over a 7 K temperature span while rotating at a 0.5 Hz rate. This Stirling-cycle wheel device used water as the regenerative fluid.

D. Rotating Anisotropic Crystal

Barclay (Ref. 11) proposed this magnetic refrigerator design based on the anisotropic nature of certain single-crystal paramagnetic materials. The anisotropic material, such as $DyPO_4$, is rotated in a constant magnetic field causing a drastic change in the material's magnetic entropy. The temperature changes associated with the changes in the paramagnetic ion polarization are used directly to heat or cool a heat exchange fluid. Each 360° rotation of the crystal represents a double execution of the thermodynamic cycle. Barclay describes a Carnot-cycle 4 to 20 K rotational refrigeration device that is capable of producing 1 W of refrigeration. A conceptual drawing of the device is shown in Fig. 6.

E. Active Magnetic Regenerator Device

The active magnetic regenerator is a device composed of layers of one or more magnetic materials having different Curie temperatures (depending on the temperature span desired) that are thermodynamically cycled like the ordinary lead regenerator of the CCR, except in this case the temperature of the materials can be changed by the application or removal of a magnetic field. Each of the different materials executes a small Brayton cycle near its Curie temperature. Depending on the number and types of different materials used, a temperature span of 10-220 K may be achieved. This concept was proposed by Barclay and Steyert (Ref. 10) and is still in the development stage. A prototype room-temperature device has been built and tested (Ref. 5) in which initial results show an 18 K temperature span using only gadolinium metal as the magnetic material.

V. A Magnetic Refrigeration System

The present and future requirements of the CCR system for the DSN are listed in Table 1. With the development of a multifrequency upconverter maser system there exists the need to develop a new CCR capable of providing 3-4 watts of refrigeration power at 4.5 K. A scaled-up version of the present DSN 1W CCR, capable of more than 3 W of refrigeration power at 4.5 K, is presently being tested. Also under investigation is the development of a 4-15 K magnetic refrigeration stage which will replace the J-T expansion circuit to provide the final stage of cooling in the CCR.

The reasons for considering a 4 to 15 K magnetic refrigeration stage are the advantages it has over the J-T circuit. This replacement eliminates the CCR failures that are a direct result of J-T circuit blockage due to gas impurities. The refrigeration power per unit volume of paramagnetic material is large (since we are dealing with a solid as the working substance rather than a gas, and the density of the solid is more than an order of magnitude greater than that of the compressed gas). This should facilitate the use of a small and compact design. The magnetic cycle itself can operate at nearly 100% efficiency; when the losses associated with the magnetic stage are included, the Carnot efficiency of the magnetic stage should still be on the order of 70% or more.

The magnetic refrigerator stage will require some moving parts, but as they will be moving at slow speeds the overall CCR reliability should not be impaired.

In order to incorporate a 4-15 K magnetic refrigeration stage into a closed-cycle refrigerator, the refrigerator components and their constraints must first be identified and fully understood. The major system components of the magnetic refrigerator are listed in Table 2. While the exact magnetic thermodynamic cycle to be used will play a part as to what the final design configuration of each component will be, it is nevertheless important to identify the main components and describe their general details. In what follows, we will discuss the pertinent points of the first four items listed in Table 2.

A. Magnetic Working Material

It is necessary to select the working material and the magnetic cycle which will best operate over the temperature span desired. Through the temperature span of interest, both the entropy and the heat capacity of the spin system of the material must be large compared to those of its lattice system so that the low spin temperature attained during a demagnetization is not appreciably curtailed by the internal heat load of the lattice. The magnetic ordering temperature of the material should be a degree or two below the lowest refrigeration temperatures desired because the magnetic entropy changes with external field become very small below this point. Other important characteristics to be considered must be its thermal, chemical and physical properties. Finally, cost, availability and machinability are also important considerations.

A study of paramagentic materials suitable for magnetic refrigeration in the 2-20 K range has been conducted by Barclay and Steyert (Ref. 9) for JPL as part of the overall R&D program on magnetic refrigeration at the Los Alamos Scientific Laboratory. The study was restricted to gadolinium compounds. In particular gadolinium gallium garnet ($Gd_2Ga_5O_{12}$ or GGG) was shown to be an excellent choice as the working material in the 4-15 K range because of its high thermal conductivity, its very low lattice heat capacity and its low ordering temperature (~0.8 K). The material is the standard substrate material used in magnetic bubble domain technology and therefore is readily available. Grown as a single crystal boule it is also very machinable. This material is presently being examined at JPL and results will be forthcoming.

B. Heat Exchange Mechanism

During the magnetic cycle, heat is periodically exchanged between the working material and the heat sink or heat source. There are two distinct ways in which this heat exchange can take place: through a thermal switch such as is needed in the isothermal stage of a Carnot cycle or through a regenerative fluid flow as would be used in the Stirling cycle, for example. Thermal switches require large switching ratios if they are to work efficiently. Two likely candidates would be magnetoresistive switches (Ref. 18), such as single crystals of beryllium, with switching ratios of 1000 at temperatures as high at 15 K, or helium gas gap switches which are actuated quickly by electrically heating charcoal to change the gas pressures. Of main importance is that no regenerative fluid is used since the field is changed by varying the magnet. However, this may cause serious problems for a nearby maser unless adequate shielding is provided. As another heat exchange mechanism, a heat exchange fluid such as high pressure helium gas can also be used to couple the working material to the hot or cold sources and to effect the regeneration. Fluid pumps will be required to operate at low temperatures to force the circulation of the fluid. It is perhaps better still to use the working material as the regenerator as in the active magnetic regenerator device. The magnetic material could be shaped in small spheres and have the helium forced through the regenerator bed to attain the necessary heat transfer.

C. Magnetic Material Drive Mechanism

The work for the magnetic refrigeration stage is provided by the drive motor. For a reciprocating design a force compensation mechanism must be utilized to pull the material in and out of the field because of the large forces involved. A more complicated cam and drive shaft are required if both the magnet and the magnetic material are to move. For both the rotating wheel and the rotating anisotropic crystal a simple axial motion of the drive shaft is used. The wheel provides its own force compensation by its continuous geometry; therefore the force from the drive shaft's torque will be smaller than the force required for the reciprocating drive units.

D. Superconducting Magnet

The biggest disadvantage in a magnetic refrigeration stage for the CCR is the need for a high field superconducting magnet. Stray fields from this magnet would pose a serious problem for maser operation unless effective shielding was provided. The shielding should be adequately accomplished through the use of high permeability or superconducting materials.

Another problem to be overcome is how to cool the magnet initially. The magnet can be cooled by an initial LHe

transfer but this method is not very feasible in light of the CCR being installed on the antennas. The magnet will most likely be precooled to 12-15 K by the two-stage expansion engine as the J-T circuit is now. From there, two options are possible: to use a Simon liquefier (expansion of stored high pressure helium gas that has been precooled to under 15 K) to produce sufficient LHe to cool the magnet; or to start the magnetic cycle at low fields at 12-15 K and have the magnetic stage cool itself down. The latter choice requires a high T_c superconducting wire such as Nb_3Sn. In either situation, once the magnetic refrigerator is operating, the small parasitic heat load required by the magnet operating in the persistent mode will require only a small fraction of the total large refrigeration capacity of the magnetic refrigeration stage.

VI. Conclusions

The idea of using magnetic refrigeration to provide the 4 K refrigeration for the DSN maser has been introduced. The main feature of the magnetic refrigerator is its potential high efficiency (more than 70% of Carnot efficiency can be expected). Additionally, because it uses solid materials it is inherently orientation-independent. This, and other design constraints laid on the refrigerator by the operating maser system on the antenna have been listed. Several different refrigerator devices have been presented as possible designs for a 4-15 K magnetic refrigeration stage. The question to be answered will be which type of magnetic refrigeration device using which thermodynamic cycles will prove to be optimal for our present and future refrigeration requirements.

References

1. Johnson, D. L., in *The Deep Space Network Progress Report 42-55*, pp. 41-49, Jet Propulsion Laboratory, Pasadena, Calif., Feb. 1980.
2. Mueller, R. M., Buchal, Chr., Folle, H. R., Kubota, M., and Pobell, F., *Phys. Lett., 75A*, 164, 1980.
3. Kittel, P., "Sub-Kelvin Temperatures in Space," Paper HB-6, presented at the Cryogenic Engineering Conference, August 10-14, 1981, San Diego.
4. Barclay, J. A., "Magnetic Refrigeration for Spacecraft Systems," Paper 81-ENAs-47, presented at the Intersociety Conference on Environmental Systems, July 13-15, 1981, San Francisco.
5. Barclay, J. A., and Steyert, W. A., "Magnetic Refrigerator Development," Report EPRI EL-1757, Final Report to the Electric Power Research Institute, April 1981.
6. Barclay, J. A., "Can Magnetic Refrigerators Liquefy Hydrogen at High Efficiency," Paper 81-HT-82, presented at the National Heat Transfer Conference, Aug. 2-5, 1981, Milwaukee.
7. Van Geuns, J. R., "A Study of a New Magnetic Refrigeration Cycle," *Philip Res. Rep. Suppl., 6*, 1966.
8. Flood, D. J., "Suitability of Rare-Earth Compounds $Dy_2Ti_2O_7$ and $Gd_3Al_5O_{12}$ for Low Temperature (4 K-20 K) Magnetic Refrigeration Cycle," Paper NASA TM X-71493, presented at the 19th Annual Conference on Magnetism, Nov. 13-16, 1973, Boston.
9. Barclay, J. A., and Steyert, W. A., "Materials for Magnetic Refrigeration Between 2 and 20 K," Los Alamos Scientific Laboratory Report LA-8746-MS, May 1981.

10. Barclay, J. A., and Steyert, W. A., "Magnetic Refrigeration of Space Applications, A Report on a Design Study," Los Alamos Scientific Laboratory Report LA-8134, Feb. 1980.

11. Barclay, J. A., "A 4 K to 20 K Rotational-Cooling Magnetic Refrigerator Capable of 1 mW to >1 W Operation," *Cryogenics, 20*, 467, 1980.

12. Steyert, W. A., in *Applications of Closed-Cycle Cryocoolers to Small Superconducting Devices*, NBS Special Publication 508, J. E. Zimmerman and T. M. Flynn, editors, 1978.

13. Giauque, W. F., and MacDougall, D. P., *Phys. Rev., 43*, 768, 1933.

14. Heer, C. V., Barnes, C. B., and Daunt, J. G., "The Design and Operation of a Magnetic Refrigerator for Maintaining Temperatures Below 1 K," *Rev. Sci. Instrum., 25*, 1088, 1954.

15. Daunt, J. G., Heer, C. V., McMahon, H. O., Reitzel, J., and Simon, I., *Bull Inst. Internat. du Froid*, Annexe 1955-3, Supplement, 362, 1955.

16. Zimmerman, J. E., McNutt, J. D., and Bohm, H. V., "A Magnetic Refrigerator Employing Superconducting Solenoids," *Cryogenics 2*, 153, 1962.

17. Rosenblum, S. S., Sheinberg, H., and Steyert, W. A., "Continuous Refrigeration at 10 mK Using Adiabatic Demagnetization," *Cryogenics, 16*, 245, 1976.

18. Radebaugh, R. J., *Low Temperature Physics, 27*, 91, 1977.

19. Brown, G. V., *J. Appl. Phys., 47*, 3673, 1976.

20. Barclay, J. A., Moze, O., and Patterson, J., *Appl. Phys., 50*, 5870, 1979.

21. Delpuech, C., Beranger, R., Bon Mardion, G., Claudet G., and Lacaze, A. A., *Cryogenics, 21*, 579, 1981.

22. Lacaze, A. F., Beranger R., Bon Mardion, G., Claudet, G., Delpuech, C., Lacaze, A. A., and Verdier, J., "A Gadolinium Gallium Garnet Double Acting Reciprocating Magnetic Refrigerator," Paper HB-6 presented at the Cryogenic Engineering Conference, August 10-14, 1981, San Diego.

23. Steyert, W. A., "Magnetic Refrigerators for Use at Room Temperature and Below," Los Alamos Scientific Laboratory Report LA-WR 78-1764, 1978.

24. Pratt, W. P., Jr., Rosenblum, S. S., Steyert W. A., and Barclay, J. A., *Cryogenics, 17*, 689, 1977.

Table 1. CCR System requirements for maser cooling

Reliable
Efficient
Multiyear lifetime
Unattended operation
Rapid cooldowns
1-4 watt cooling capacity
Compact
Magnetic field isolation of maser package
Low microphonics
mK temperature stability
Orientation independence
Continued operation during power failures

Table 2. Major components of a magnetic refrigerator system

Solid magnetic working material
Heat exchange mechanism
Magnetic material drive mechanism
Superconducting magnet
Dewar
15 K refrigerator precooler

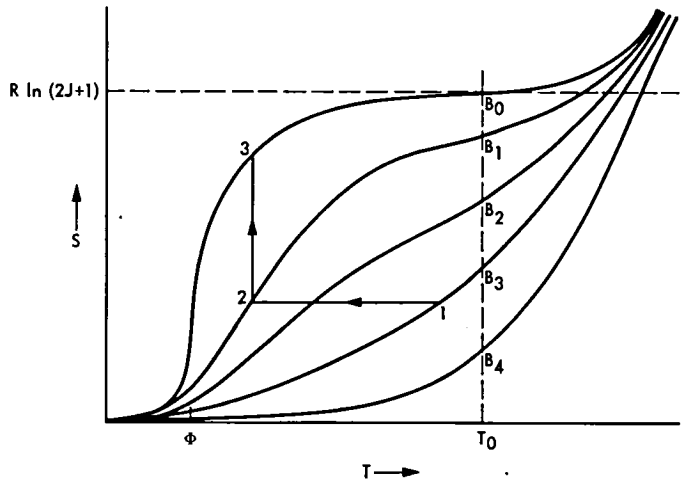

Fig. 1. S, T-diagram for a typical paramagnetic material showing the entropy vs temperature curves for several applied magnetic fields. Process 1 → 2 shows an isentropic (adiabatic) demagnetization which decreases the temperature of the material. Process 2 → 3 shows an isothermal demagnetization whereby the material absorbs heat from low-temperature heat source. Temperatures Φ and T_0 are defined in the text

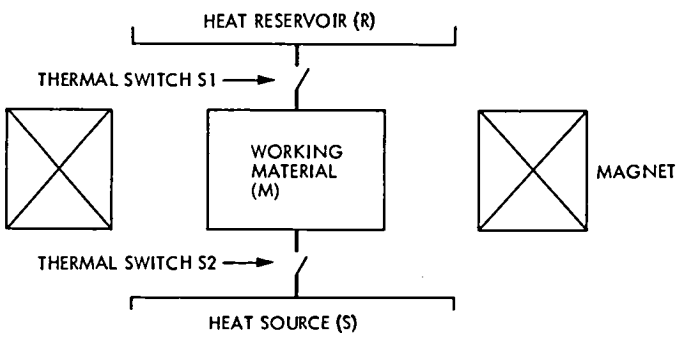

Fig. 2. Schematic diagram of a conventional magnetic refrigerator. The cyclic operation of this refrigerator is discussed in the text

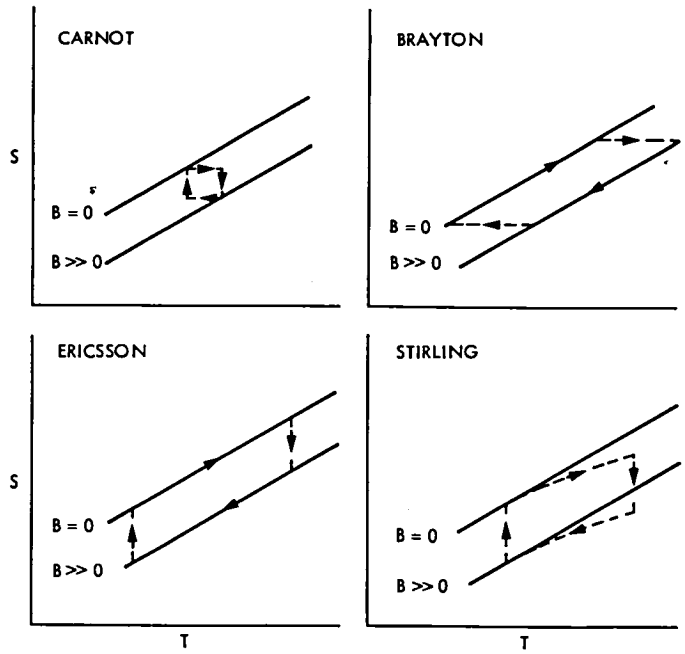

Fig. 3. Four magnetic cycles that can be used to make a cyclic magnetic refrigerator. The processes of each cycle are mentioned in the text (taken from Ref. 6)

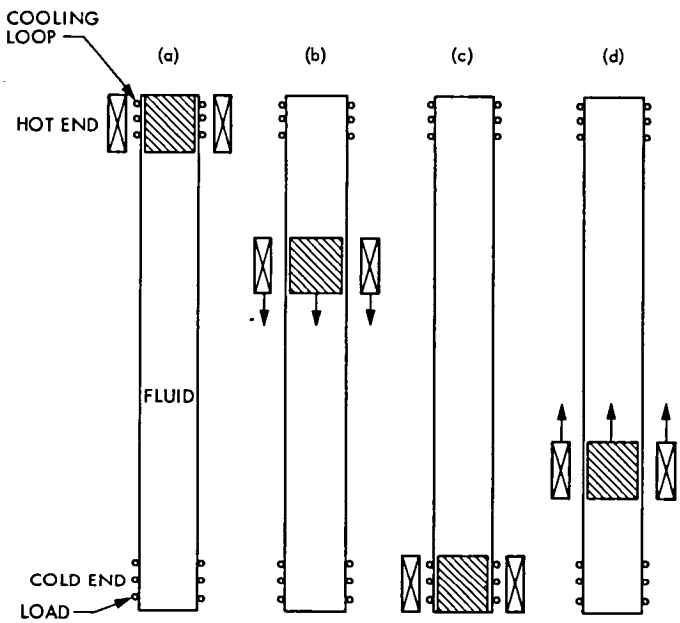

Fig. 4. Schematic diagram of magnetic Stirling cycle. The processes are (a) isothermal magnetization, (b) isofield cooling in regenerator, (c) isothermal demagnetization, and (d) zero (or low) field heating in regenerator (taken from Ref. 19)

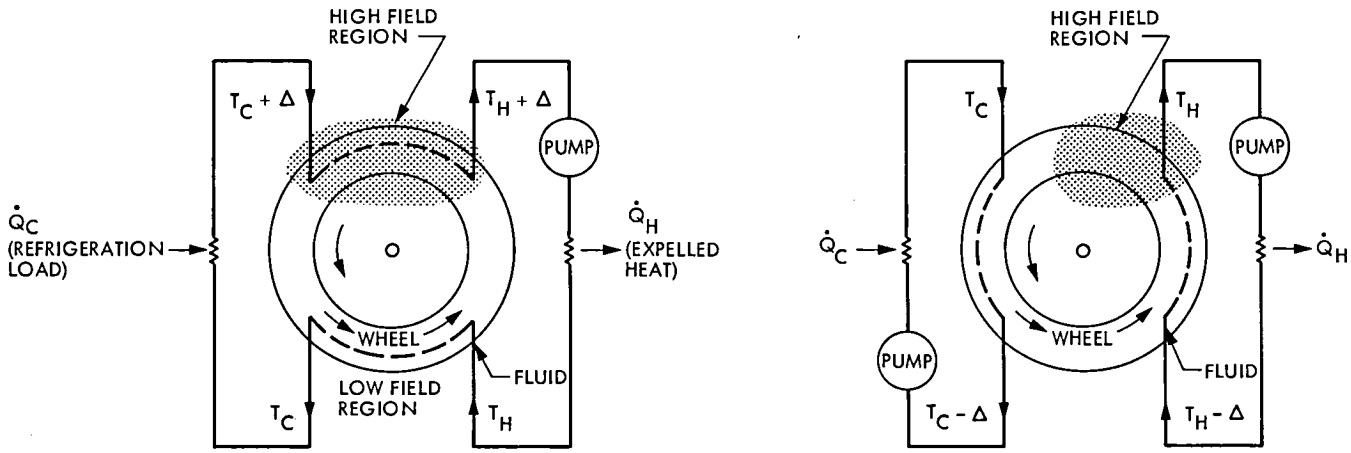

Fig. 5. Schematics of (a) Stirling-cycle wheel and (b) Carnot-cycle wheel refrigerators. The paramagnetic material forming the rim of the wheels rotates in a counterclockwise direction. The fluid flow is forced by a pump and its direction of motion is indicated by the arrows. The high magnetic field region is indicated by the shaded area. Radially across the wheel is the low field region. Δ represents the inherent temperature change of the working material upon entering and leaving the field (taken from Ref. 23)

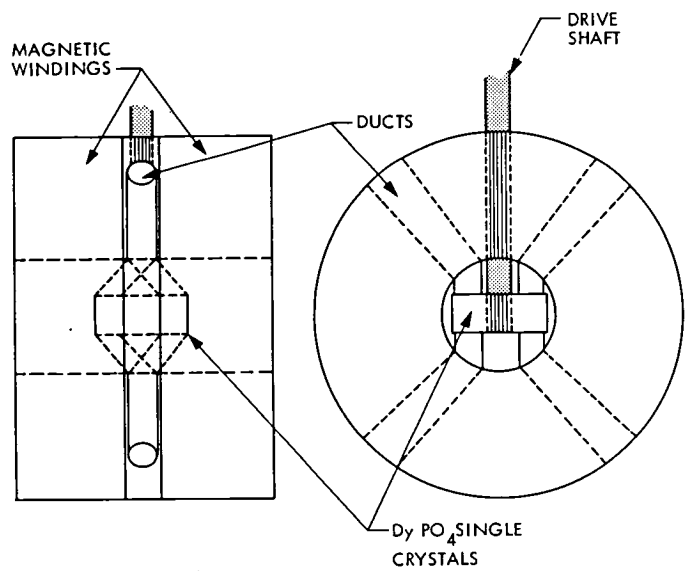

Fig. 6. Side and end views of a wheel of $DyPO_4$ single crystals inside a superconducting magnet. The drive shaft and ducts are also shown (taken from Ref. 11)

Sideband-Aided Receiver Arraying

S. A. Butman, L. J. Deutsch, R. G. Lipes, and R. L. Miller
Communications Systems Research Section

Recently, there has been a substantial effort to increase the amount of data that can be received from outer planet missions by coherently combining signals from ground antennas in such a way as to increase the total effective aperture of the receiving system. However, as these signals become weaker, the baseband arraying technique in current use degrades somewhat due to carrier jitter. One solution to this problem is Sideband-Aided Receiver Arraying (SARA). In SARA, sidebands demodulated to baseband in a master receiver at the largest antenna are used to allow slave receivers in the other antennas to track the sideband power in the signal rather than the carrier power. The already existing receivers can be used in the slaves to track and demodulate the signals in either a residual carrier or a suppressed carrier environment. The resultant baseband signals from all the antennas can then be combined using existing baseband combining equipment. Computer simulations of SARA show increases in throughput (measured in data bits per second) over baseband-only combining of 17% at Voyager 2 Uranus encounter and 31% at Neptune for a four-element antenna array and (7, 1/2) convolutional coding.

I. Introduction

Many different antenna arraying systems have been proposed for receiving increased telemetry rates from outer planet missions. The performance of two of these schemes, "baseband-only combining" (BBO) and "baseband combining with combined carrier referencing" (CCR), have been studied by the authors (Ref. 1). BBO (Refs. 2, 3) is the scheme that is currently used by the DSN for Voyager. In BBO each receiver demodulates its own carrier using a conventional phase locked loop (PPL). CCR schemes involve summing the carrier signals from the arrayed antennas in phase so that the array behaves like a single antenna with aperture equal to the sum of the apertures of the individual array elements. Two different implementations of CCR have been studied in detail. These are the "master-slave system" (Refs. 4, 5) and "virtual center arraying" (Ref. 6). All of the above-mentioned arraying schemes require the presence of a residual carrier for tracking.

Sideband-Aided Receiver Arraying (SARA) is an arraying system that offers increased performance over BBO and CCR at high modulation indices (such as those proposed for Voyager 2 Uranus and Neptune encounters) and the ability to operate in a suppressed carrier environment. Suppressed carrier transmission, in which the modulation index is equal to 90°, offers a $\text{secant}^2(\theta)$ improvement in bit energy-to-noise ratio over residual carrier transmission with a modulation index of θ. For Voyager 2 Uranus and Neptune encounters, suppressing the carrier will yield a 0.25-dB improvement in E_b/N_0.

SARA is a master-slave type system. Either a conventional tracking loop or suppressed carrier tracking loop may be used

in the master channel to demodulate the carrier and produce good data and subcarrier estimates. A suppressed carrier loop will yield better performance in most cases, and the conceptual block diagrams described in this article are for this type of loop. The master channel is associated with the largest antenna in the array where the signal-to-noise ratio is largest. The slave receivers contain conventional tracking loops that are aided by the subcarrier and data estimates derived in the master. These sidebands are relatively low frequency and low bandwidth signals that may be transmitted digitally over existing microwave links. Hardware must be provided in each slave for proper alignment of its modulation with the estimates it receives from the master. This aiding allows the slave receivers to track the sideband power in the incoming signal (rather than the carrier power), with losses that are lower than those that would be present in systems with separate suppressed carrier loops in each slave. The demodulated baseband signals from the master and all slaves are then combined in a baseband combiner in the same way as in BBO.

In the following sections, SARA is described in more detail. Loop signal-to-noise ratios are derived for the master and slave receivers. Degradations due to subcarrier demodulation, subcarrier alignment, and data alignment are discussed. Section VI discusses the performance of SARA at Voyager 2 Uranus and Neptune encounters for two-, three-, and four-element arrays as determined from computer simulations. These results show that SARA, operating in a suppressed carrier environment, has less radio loss than either BBO or CCR. Graphs of data rate vs time for the two encounters are also presented, and these clearly show the increased telemetry capability that SARA allows.

II. The Data-Aided Loop

In the preferred implementation of SARA, the master receiver should be capable of operating with both residual and suppressed carrier signals. Three well-known regenerative loops can be employed for obtaining a carrier reference from a suppressed carrier signal. These are the squaring loop (Ref. 7), the Costas loop (Ref. 7), and the "data-aided" loop (Ref. 8). Moreover, these implementations provide very good carrier reference estimates from residual carrier signals whose carrier power is suppressed by more than 12 dB below the data sideband power (Ref. 9). In the body of this article, only the data-aided implementation will be considered. Comparative analyses of data-aided and Costas or squaring loops are given in Refs. 7 and 8. A block diagram of a data-aided loop appears in Fig. 1. The input to this loop is assumed to be a phase-modulated sinusoid of frequency ω_0 with no subcarrier. Since the data-aided loop tracks only the data power in the signal, it may be assumed that $x(t)$ has the form

$$x(t) = \sqrt{2P_D}\sin[\omega_0 t + \pi/2\, d(t) + \phi] + n_1(t)$$

$$= \sqrt{2P_D}\, d(t)\cos(\omega_0 t + \phi) + n_1(t)$$

where P_D is the data power of the signal, $d(t)$ is the data in the form of plus and minus ones that are constant for a symbol time T_s, and ϕ is the phase of the signal. In this analysis it is assumed that ϕ changes slowly with time compared to $d(t)$. The noise, $n_1(t)$, is assumed to be a narrowband Gaussian process with one-sided spectral density N_0 W/Hz in the region of interest.

The output of the VCO is

$$r(t) = \sqrt{2}K_1\cos(\omega_0 t + \hat{\phi})$$

where K_1 is a gain associated with the VCO and $\hat{\phi}$ is the loop's estimate of the phase error ϕ. It follows that, after filtering out the double frequency terms,

$$y(t) = \sqrt{P_D}K_1K_2\, d(t)\cos(\phi - \hat{\phi}) + n_2(t)$$

where K_2 is the gain of the upper mixer and n_2 is a white Gaussian process with one-sided spectral density $K_1 K_2 N_0$ W/Hz over the closed-loop bandwidth. The data detector integrates $y(t)$ over a symbol time T_s. The sign of this integral defines the data estimate

$$e(t) = \hat{d}(t - T_s).$$

The probability that a correct estimate is made is

$$pr(\hat{d} = d) = 1/2 + 1/2\,\mathrm{erf}(\sqrt{E_s/N_0}\cos[\phi - \hat{\phi}])$$

where

$$\mathrm{erf}(x) = 2/\sqrt{\pi}\int_0^x \exp(-t^2)\,dt.$$

Therefore, the mean value of $e(t)$ is given by

$$\overline{e(t)} = d(t - T_s)\,pr(\hat{d} = d) - d(t - T_s)\,pr(\hat{d} \neq d)$$

$$= d(t - T_s)\,\mathrm{erf}(\sqrt{E_s/N_0}\cos[\phi - \hat{\phi}]).$$

The quadrature carrier estimate $s(t)$ is given by

$$s(t) = -\sqrt{2}K_3\sin(\omega_0 t + \hat{\phi})$$

where K_3 is a gain associated with the VCO and the quadrature generator box (labeled "$\pi/2$" in the figure). After the lower mixer, an associated low-pass filter to attenuate the double frequency terms, and a one symbol time delay,

$$w(t) = \sqrt{P_D} K_3 K_4 \, d(t - T_s) \sin(\phi - \hat{\phi}) + n_3(t)$$

where K_4 is the gain in the mixer and $n_3(t)$ is a white Gaussian noise process with one-sided spectral density $K_3 K_4 N_0$ W/Hz. Notice that n_2 and n_3 are uncorrelated due to the fact that they are in quadrature with one another.

Under the previously stated assumption that ϕ varies slowly with respect to $d(t)$,

$$z(t) \approx \overline{e}(t)\, w(t)$$

$$= \sqrt{P_D} K_3 K_4 \sin(\phi - \hat{\phi}) \operatorname{erf}\left[\sqrt{E_s/N_0} \cos(\phi - \hat{\phi})\right] + n_4(t).$$

For small phase errors $\phi - \hat{\phi}$ this linearizes to

$$z(t) = \sqrt{P_D} K_3 K_4 \, [\phi - \hat{\phi}] \operatorname{erf}(\sqrt{E_s/N_0}) + n_4(t)$$

from which the standard PLL theory (see Appendix A) shows the loop signal-to-noise ratio (loop SNR) of the data-aided loop to be

$$\rho = \frac{P_D}{N_0 B_L} \operatorname{erf}^2(\sqrt{E_s/N_0})$$

where B_L is the one-sided closed-loop bandwidth of the receiver.

III. The Slaves

In SARA, the modulation estimates obtained in the master are sent to each slave to aid in tracking. Figure 2 shows a diagram of a slave that could be used in conjunction with the data-aided loop described in the last section. In this implementation, a hard-limited estimate of the data ($e(t)$ in Fig. 2) is passed to the slave to derive a carrier reference. In Appendix B, the rationale for this procedure is developed. The input signal is again assumed to have the form

$$x_s(t) = \sqrt{2P_{Ds}}\, d(t) \cos[\omega_0 t + \phi_s] + N_1(t) \qquad (1)$$

where P_{Ds} is the data power in the slave and ϕ_s is the phase of the signal. It is assumed that ϕ_s changes slowly with respect to $d(t)$ although it is not necessarily the same as ϕ. The carrier estimate from the VCO is

$$r_s(t) = -\sqrt{2} K \sin[\omega_0 t + \hat{\phi}_s]$$

where K is a gain associated with the VCO and $\hat{\phi}_s$ is the phase estimate of the slave loop. After filtering out the double frequency components and delaying, it follows that

$$y_s(t) = \sqrt{P_{Ds}} K K' \, d(t - T_s) \sin(\phi_s - \hat{\phi}_s) + N_2(t). \qquad (2)$$

If $e(t)$ is perfectly aligned, then

$$z_s(t) \approx \overline{e}(t)\, y_s(t)$$

$$= \sqrt{P_{Ds}} K K' \sin(\phi_s - \hat{\phi}_s) \operatorname{erf}\left[\sqrt{E_s/N_0} \cos(\phi - \hat{\phi})\right]$$

$$+ N_3(t)$$

where N_3 is a white Gaussian process independent of the noise in the master. If both the phase errors in the master and the slave are small, then this can be linearized to

$$z_s(t) = \sqrt{P_{Ds}} K K' \, [\phi_s - \hat{\phi}_s] \operatorname{erf}(\sqrt{E_s/N_0}) + N_3(t).$$

Standard PLL theory (see Appendix A) then shows that the loop SNR in the slave is given by

$$\rho_s = \frac{P_{Ds}}{N_{0s} B_{Ls}} \operatorname{erf}^2(\sqrt{E_s/N_0}) \qquad (3)$$

where N_{0s} is the one-sided noise spectral density in the slave, and B_{Ls} is the one-sided closed-loop bandwidth of the slave.

IV. Subcarrier Demodulation

In Sections II and III, only signals without subcarriers were considered. If the incoming signal has a subcarrier, then a subcarrier tracking loop must be added to the master receiver in order to demodulate the subcarrier before the data can be detected. The subcarrier estimate must also be sent to the slaves along with the data estimate. Figure 3 shows one possible configuration for a SARA master and slave with such a subcarrier loop added. The subcarrier is assumed to be a square wave in the following analysis.

The subcarrier tracking loop in the master is, itself, a data-aided loop similar to that described in Section II. It shares the data detection arm with the carrier tracking loop. The principal difference is that the input to the subcarrier loop is an amplitude-modulated square wave,

$$i(t) = \sqrt{P_D} K_1 K_3 \, d(t) \, \square\sin(\omega_{sc} t) \cos(\phi - \hat{\phi}) + n_2(t)$$

where P_D, K_1, K_3, ϕ, $\hat{\phi}$, and n_2 are as defined in Section II. The subcarrier frequency ω_{sc} is assumed to be high compared to the channel symbol rate $R_s = 1/T_s$. For Voyager 2 Uranus and Neptune encounters, $\omega_{sc} = 360$ kHz while $R_s < 40$ kHz. Recall that ϕ and $\hat{\phi}$ also vary slowly compared to $d(t)$. Under these assumptions, the analysis of the subcarrier tracking loop is identical to that of the carrier tracking loop with the exception that only the first harmonic of the subcarrier is retained after mixing with the subcarrier estimate $j(t)$. Since the fraction of the total square wave power in the first harmonic is $8/\pi^2$, the subcarrier tracking loop SNR is given by

$$\rho_{sc} = \frac{8}{\pi^2} \frac{P_D}{N_0 B_{Lsc}} \operatorname{erf}^2 (\sqrt{E_s/N_0})$$

where B_{Lsc} is the closed-loop bandwidth of the subcarrier tracking loop.

In practice, once subcarrier and carrier lock have occurred in the master, the bandwidth of the subcarrier loop can be narrowed, since most of the doppler error in the incoming signal is removed by carrier demodulation. Hence, in the steady state, subcarrier demodulation losses should be small compared to carrier demodulation losses in the master receiver.

In order to aid the slave receivers, the subcarrier and data estimates are recombined. The subcarrier estimate $j(t)$ must be delayed by one symbol time before being mixed with the data estimate. The slave is then aided just as in Section III, with both data and subcarrier demodulation occurring simultaneously.

V. Alignment Losses

Thus far it has been assumed that the modulation estimates from the master are perfectly aligned with the modulation in the slaves. In practice, there will be losses resulting from an imperfect alignment of these signals. This misalignment will result in a degradation in the loop SNR of the slaves and therefore will result in poorer performance in those receivers.

Suppose that the modulations of the master and slave are misaligned by τ seconds (where $|\tau| < 1/4\omega_{sc}$). Then the average value of the product of the subcarriers will not be one as in the case of perfect alignment. Instead it will be

$$\overline{\operatorname{Sin}(\omega_{sc}t)\operatorname{Sin}(\omega_{sc}t+\tau)} = (1/(2\omega_{sc}) - 2|\tau|)/[1/(2\omega_{sc})]$$

$$= 1 - 4\omega_{sc}|\tau| .$$

If the transition probability in the symbol stream $d(t)$ is p_t, then the average value of the product of the data signals is

$$\overline{d(t)\,d(t+\tau)} = (T_s/p_t - 2|\tau|)/(T_s/p_t)$$

$$= 1 - 2p_t R_s|\tau| .$$

These lead to a degraded slave loop SNR of

$$\rho_s = \frac{P_D}{N_0 B_{Ls}} \operatorname{erf}^2 (\sqrt{E_s/N_0})\,(1 - 4\omega_{sc}|\tau|)^2\,(1 - 2p_t R_s|\tau|)^2 .$$

Graphs of the losses due to improper subcarrier and data alignment in the slaves appear in Figs. 4 and 5 respectively. A subcarrier frequency of 360 kHz and a data frequency of 38.4 ksps were assumed in these plots. These are typical values for the Voyager 2 Uranus encounter. Notice that the alignment loss is much greater in the subcarrier than in the data.

The primary cause of misalignment in SARA will be interreceiver timing problems due to link jitter. A study of the existing GCF10-DSS 14 microwave link (Ref. 10) shows a two-way link jitter on the order of 20 nanoseconds. With additional alignment hardware in the slaves to take care of gross interreceiver time delays, the alignment degradations due to the link can probably be kept to a tolerable level (less than a dB of loop SNR).

VI. Numerical Results

The performance of SARA on coded telemetry was determined by software simulation. The code used was the DSN standard (7, 1/2) convolutional code with Viterbi (maximum likelihood) decoding. Perfect subcarrier demodulation, symbol tracking, and modulation alignment were assumed. The only losses were the space loss, a 90% weather confidence attenuation, and the independent carrier phase jitter in each receiver.

Carrier loop simulation software was used to generate the phase errors for each of n receivers according to the distribution

$$p_i(\phi_i) = \frac{\exp(\rho_i \cos\phi_i)}{2\pi I_0(\rho_i)} \quad (i = 1, 2, 3, \ldots, n)$$

where ϕ_i is the carrier phase error in the i^{th} receiver, ρ_i is the loop SNR of that receiver and I_0 is the zero-order Bessel function. The loop SNRs for SARA master and slave receivers are those given in Sections II and III respectively. If a signal with total bit signal-to-noise ratio E_b/N_0 is received by this

array, then the bit SNR seen at the output of the baseband combiner is

$$TOTSNR = E_b/N_0 \left(\sum_{i=1}^{n} w_i \cos \phi_i\right)^2$$

where w_i is the fraction of signal amplitude seen by the i^{th} antenna. A software Viterbi decoder was used to monitor the decoded bit errors made by the system.

The performances of BBO and CCR systems were also determined by the software. BBO was simulated in exactly the same way as SARA except that the ρ_i were the loop SNRs of conventional receivers. CCR was modelled as a single antenna whose aperture would receive the total power incident on the array.

The power-to-noise ratios for Voyager 2 Uranus encounter were taken from design control tables (Ref. 11). The power-to-noise ratios for Neptune encounter were assumed to be 3.5 dB less than those for Uranus encounter due to the increased distance of the spacecraft from Earth. The loop SNRs of the various receivers were calculated from these power-to-noise ratios according to the formulas given in Ref. 1 and in Sections II and III. A threshold loop bandwidth of $2B_{LO} = 30$ Hz was assumed in all receivers for comparison purposes.

Tables 1 and 2 show the relative performance of BBO, CCR, and SARA at Voyager 2 Uranus and Neptune encounters for two-, three-, and four-element arrays. The modulation indices were optimized to within 2 degrees. The numbers labeled "maximum data rate" represent the highest possible information bit rate that would allow transmission at a bit error rate of 5×10^{-3}. Since, in practice, Voyager has only a small number of available data rates, these numbers should be considered as a convenient measure of system performance rather than as actual data rates. From the tables it is clear that SARA performs substantially better than CCR and BBO for these Voyager scenarios. Data rates for SARA are about 11% higher than either of the other schemes.

The performance of SARA was also determined at a modulation index of 76°. The maximum data rates for Uranus and Neptune encounters were found to be 26.5 kbps and 11.7 kbps respectively. This means that data rate increases of 2.3% for Uranus encounter and 5.4% for Neptune encounter over CCR are attainable with SARA without suppressing the carrier.

The relative performance of the various arraying schemes is also shown in plots of maximum data rate vs time for the two Voyager planetary encounters. These plots appear in Fig. 6 for Uranus encounter and in Fig. 7 for Neptune encounter. (In the case of Neptune encounter, the time axis should be read as hours relative to some unspecified zero hour.) Horizontal dotted lines represent the data rates that are actually available on Voyager. One may determine the number of hours of transmission at an average bit error rate of 5×10^{-3} from these graphs for each of the arraying schemes, data rates, and array configurations. This is done by observing how much of the particular data rate curve is above the data rate line in question. For example, with a four-element array at Uranus encounter, SARA provides about 13.8 hours of viewing at a data rate of 19.2 kbps, while CCR allows only about 12.3 hours and BBO only 11.8 hours. This represents an improvement in throughput of 12% over CCR and 17% over BBO. At Neptune, the corresponding improvements at 8.4 kbps are 12% over CCR and 31% over BBO.

VII. Summary and Conclusions

The numerical results presented in Section VI show that SARA offers improvements in throughput for Voyager 2 Uranus and Neptune encounters. The improvements are due primarily to two effects. The first is the ability of SARA to work in a suppressed carrier environment. For example, while the optimum modulation index for CCR at Uranus encounter is about 76°, SARA can operate at a modulation index of 90°. Consequently, SARA can see 0.26 dB (6%) more data power than CCR. The second effect is the smaller radio loss of SARA as compared to the other two systems. The radio loss is lower because the sideband aiding in both the master and the slaves greatly increases the receiver loop SNRs over conventional phase lock loops. A greater loop SNR means smaller phase jitter and better tracking.

Another advantage to SARA is that it can be made compatible with existing DSN hardware. The slave receivers can be existing Block III or Block IV receivers with a mixer added for the sideband aiding. The master can be built as described in the text, or it can be made out of an existing receiver by taking the modulation estimates out of the Subcarrier Demodulation Assembly (SDA) and the Symbol Synchronizer Assembly (SSA). The modulation can be sent to the slave receivers over existing microwave links, and they can be aligned with the modulations in the slaves using reprogrammed Real Time Combiners (RTCs). One possible DSN implementation of SARA is shown in Fig. 8.

A number of issues associated with the SARA concept remain to be addressed. Optimal loop filter parameters for specific situations such as the Voyager planetary encounters should be derived. The question of tracking loop acquisition is also very important. The sideband aiding in the slaves should

help them acquire in a low SNR environment where a conventional PLL might not lock at all. The master has three coupled loops: the carrier loop, subcarrier loop, and the data loop (included in the data detection function). An efficient lockup sequence should be established. It may be necessary to change filter parameters for the acquisition process. Also, a device for detecting when lock has occurred in each loop might be needed.

References

1. Deutsch, L. J., Miller, R. L., and Butman, S. A., "New Results on Antenna Arraying: Part 1," in *TDA Progress Report 42-62, January and February 1981*, Jet Propulsion Laboratory, Pasadena, Calif., April 15, 1981.

2. Winkelstein, R. A., "Analysis of the Signal Combiner for Multiple Antenna Arraying," in *DSN Progress Report 42-26, January and February 1975*, Jet Propulsion Laboratory, Pasadena, Calif., April 15, 1975.

3. Howard, L. D., "Prototype Real-time Baseband Signal Combiner," in *TDA Progress Report 42-60, September and October 1980*, Jet Propulsion Laboratory, Pasadena, Calif., Dec. 15, 1980.

4. Brockman, M. H., "Radio Frequency Carrier Arraying for High Rate Telemetry Reception," in *DSN Progress Report 42-45, March and April 1978*, Jet Propulsion Laboratory, Pasadena, Calif., June 15, 1978.

5. Divsalar, D., and Yuen, J., "Improved Carrier Tracking Performance with Coupled Phase-Locked Loops," in *TDA Progress Report 42-66, September and October 1981*, Jet Propulsion Laboratory, Pasadena, Calif., Dec. 15, 1981.

6. Deutsch, L. J., Lipes, R. G., and Miller, R. L., "Virtual Center Arraying," in *TDA Progress Report 42-65, July and August 1981*, Jet Propulsion Laboratory, Pasadena, Calif., Oct. 15, 1981.

7. Lindsey, W. C., and Simon, M. K., *Telecommunications Systems Engineering*, Prentice-Hall, Inc., N.J., 1973.

8. Simon, M. K., and Springett, J. C., "The Theory, Design, and Operation of the Suppressed Carrier Data-Aided Tracking Receiver," JPL Technical Report 32-1583, June 15, 1973.

9. Park, Y. H., "Effect of CW RF Interference on the Carrier Tracking Performance of a Costas Loop," IOM 3391-80-36, March 26, 1980 (JPL internal document).

10. Ware, K. C., "Goldstone AMW/One Pulse Per Second Interface," IOM 377D-80-238-KCW, May 9, 1980 (JPL internal document).

11. Madsen, B., "Voyager Uranus Encounter Telemetry Performance," IOM # VOYAGER-SCT-80-0411, August 25, 1980 (JPL internal document).

Table 1. Performance of various arraying schemes at Voyager 2 Uranus encounter (0 hour GMT, Day 34, 1986; BER = 0.005, $2B_{LO}$ = 30 Hz)

Array configuration		Optimal modulation index, deg	Radio loss, dB	Maximum data rate, kbps
64m-34m(T/R):				
	BBO	74	0.32	16.1
	CCR	74	0.25	16.4
	SARA	90	0.07	18.3
64m-34m(LO)-34m(T/R):				
	BBO	74	0.29	20.9
	CCR	74	0.22	21.3
	SARA	90	0.10	23.4
64m-34m(LO)-34m(LO)-34m(T/R):				
	BBO	74	0.30	25.1
	CCR	76	0.22	25.9
	SARA	90	0.08	28.3

Table 2. Performance of various arraying schemes at Voyager 2 Neptune encounter (Peak of day curve; BER = 0.005, $2B_{LO}$ = 30 Hz)

Array configuration		Optimal modulation index, deg	Radio loss, dB	Maximum data rate, kbps
64m-34m(T/R):				
	BBO	72	0.51	6.75
	CCR	72	0.45	6.84
	SARA	90	0.25	8.04
64m-34m(LO)-34m(T/R):				
	BBO	72	0.59	8.53
	CCR	72	0.34	9.04
	SARA	90	0.20	10.2
64m-34m(LO)-34m(LO)-34m(T/R):				
	BBO	70	0.43	10.4
	CCR	74	0.36	11.1
	SARA	90	0.23	12.2

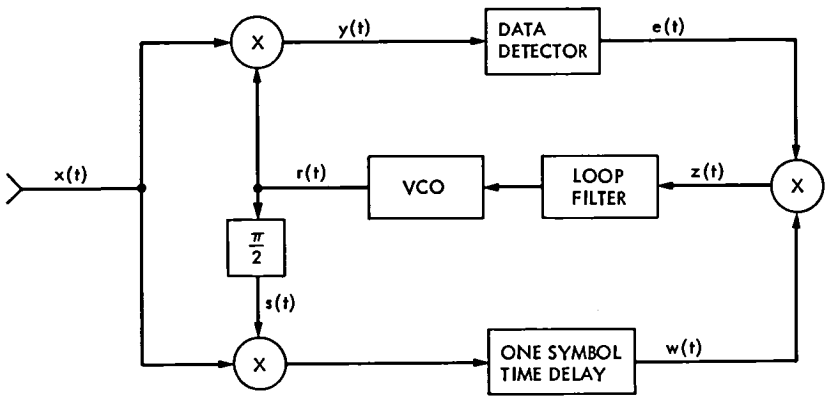

Fig. 1. The data-aided loop

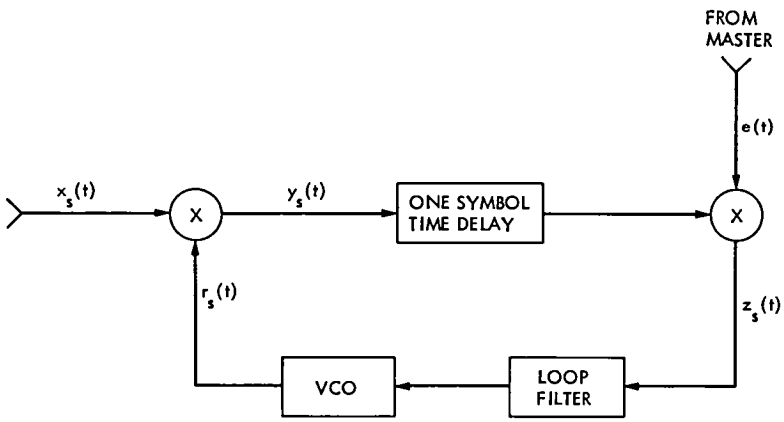

Fig. 2. A slave receiver in SARA

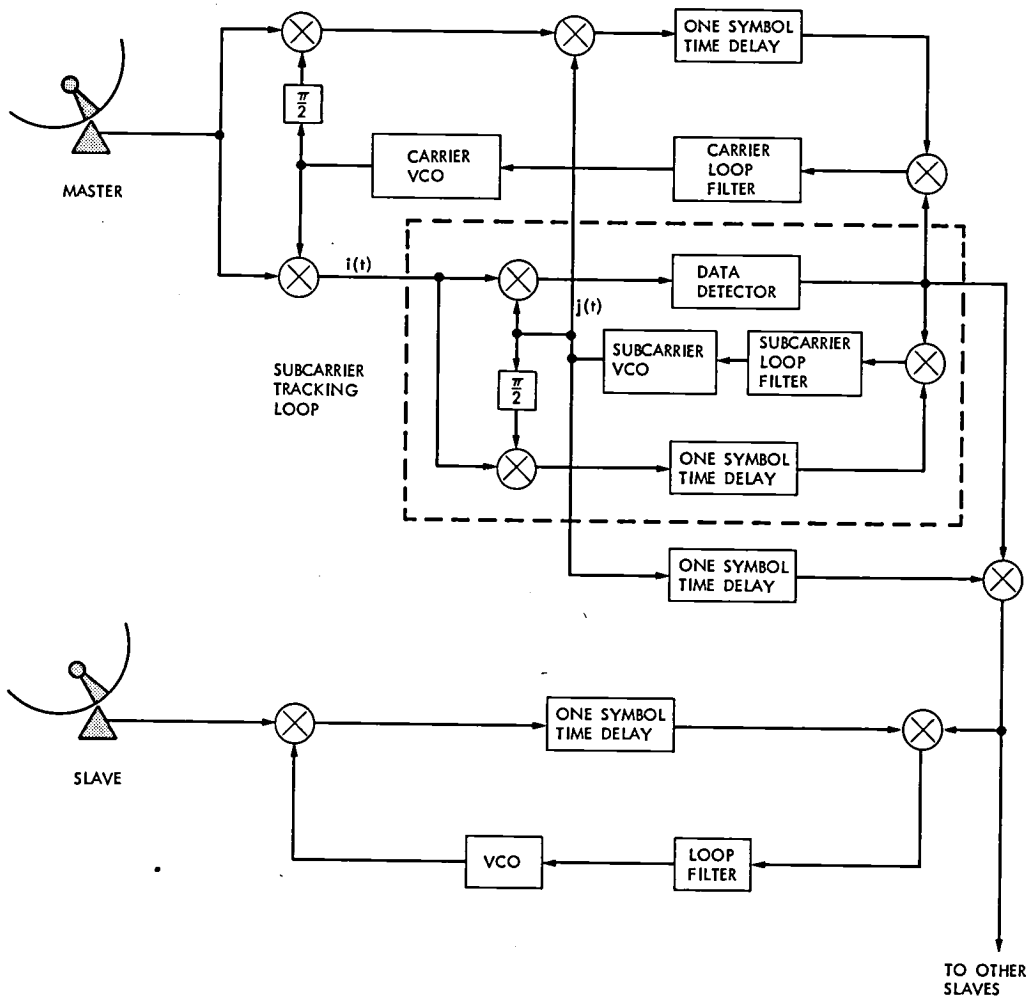

Fig. 3. SARA with subcarrier demodulation

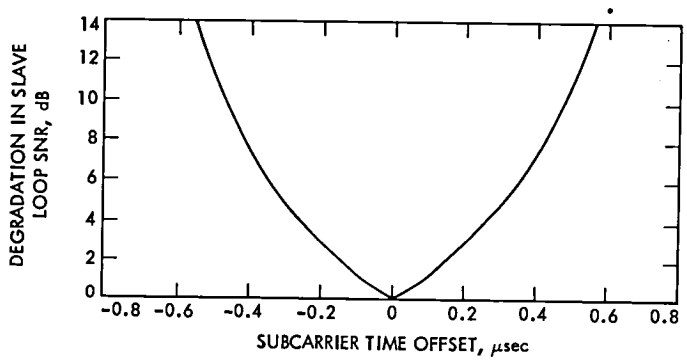

Fig. 4. Degradation in loop SNR of SARA slave due to misalignment of subcarriers (ω_{SC} = 360 kHz)

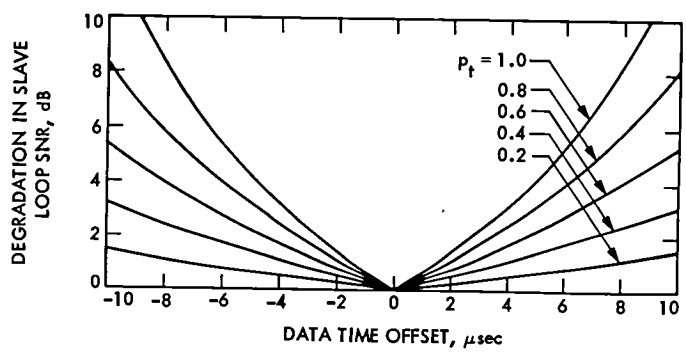

Fig. 5. Degradation in loop SNR of SARA slave due to misalignment of data stream (R_S = 38.4 ksps; p_t = .2, .4, .6, .8, 1.0)

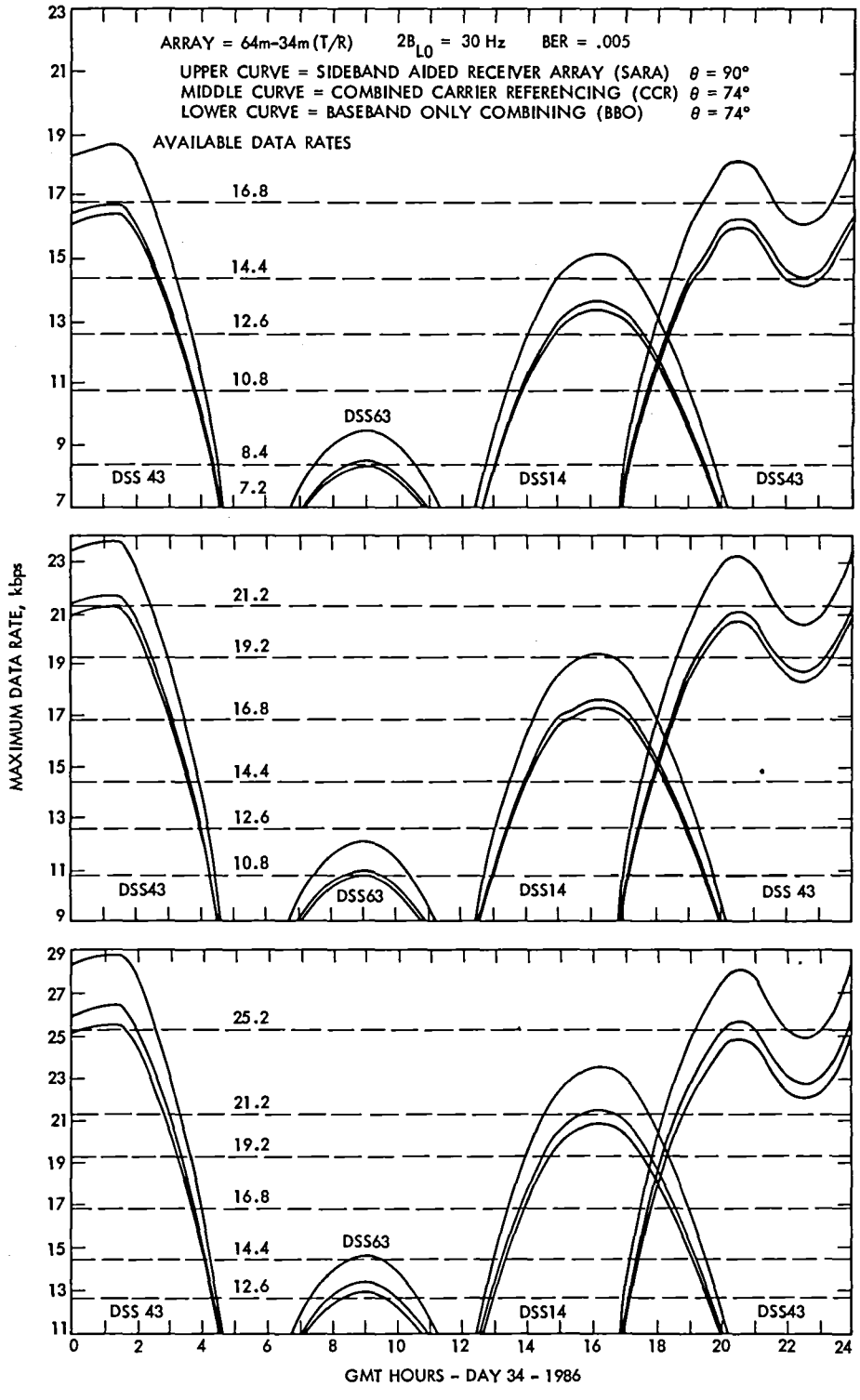

Fig. 6. Data rate vs time: Voyager 2 Uranus encounter

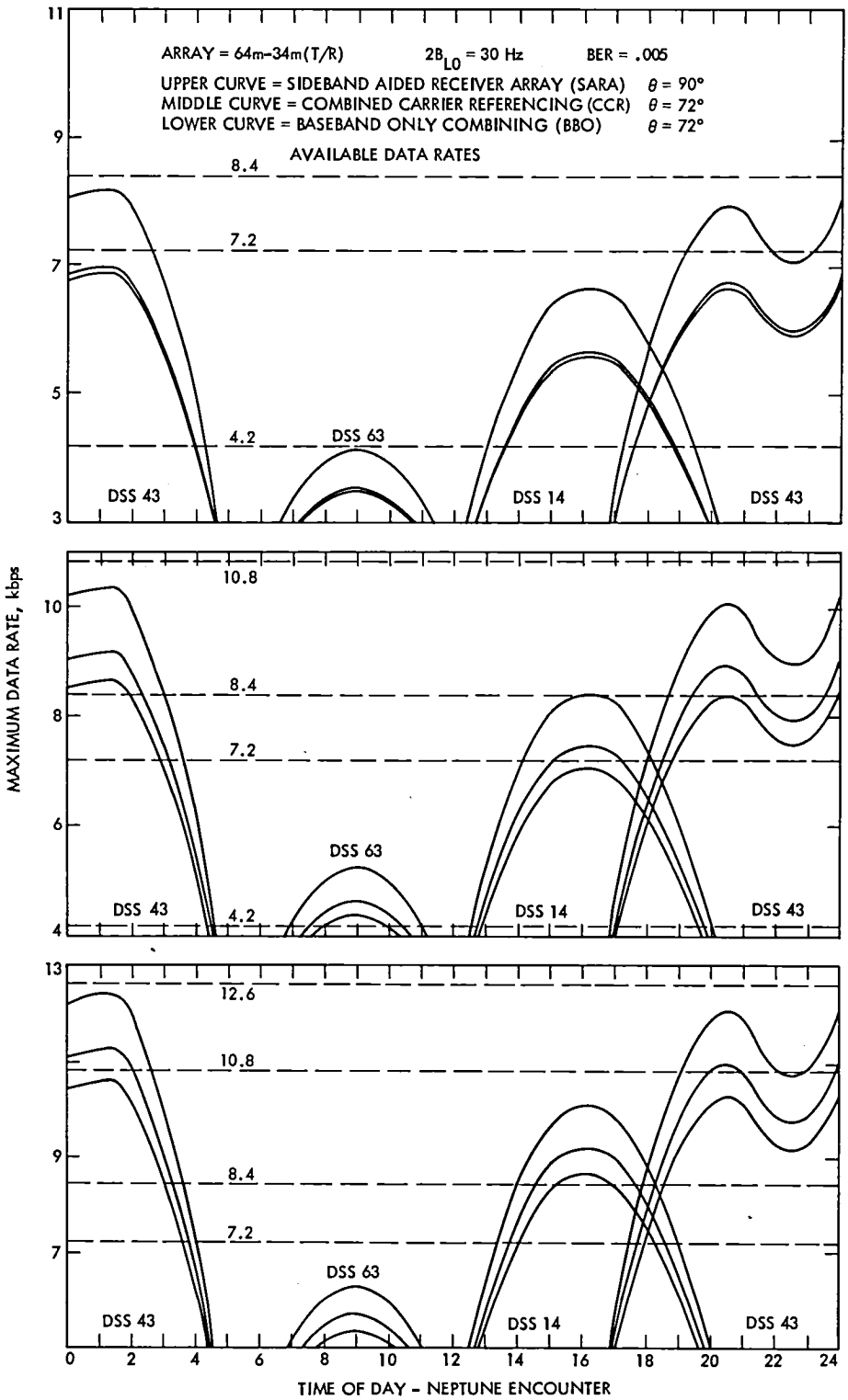

Fig. 7. Data rate vs time: Voyager 2 Neptune encounter

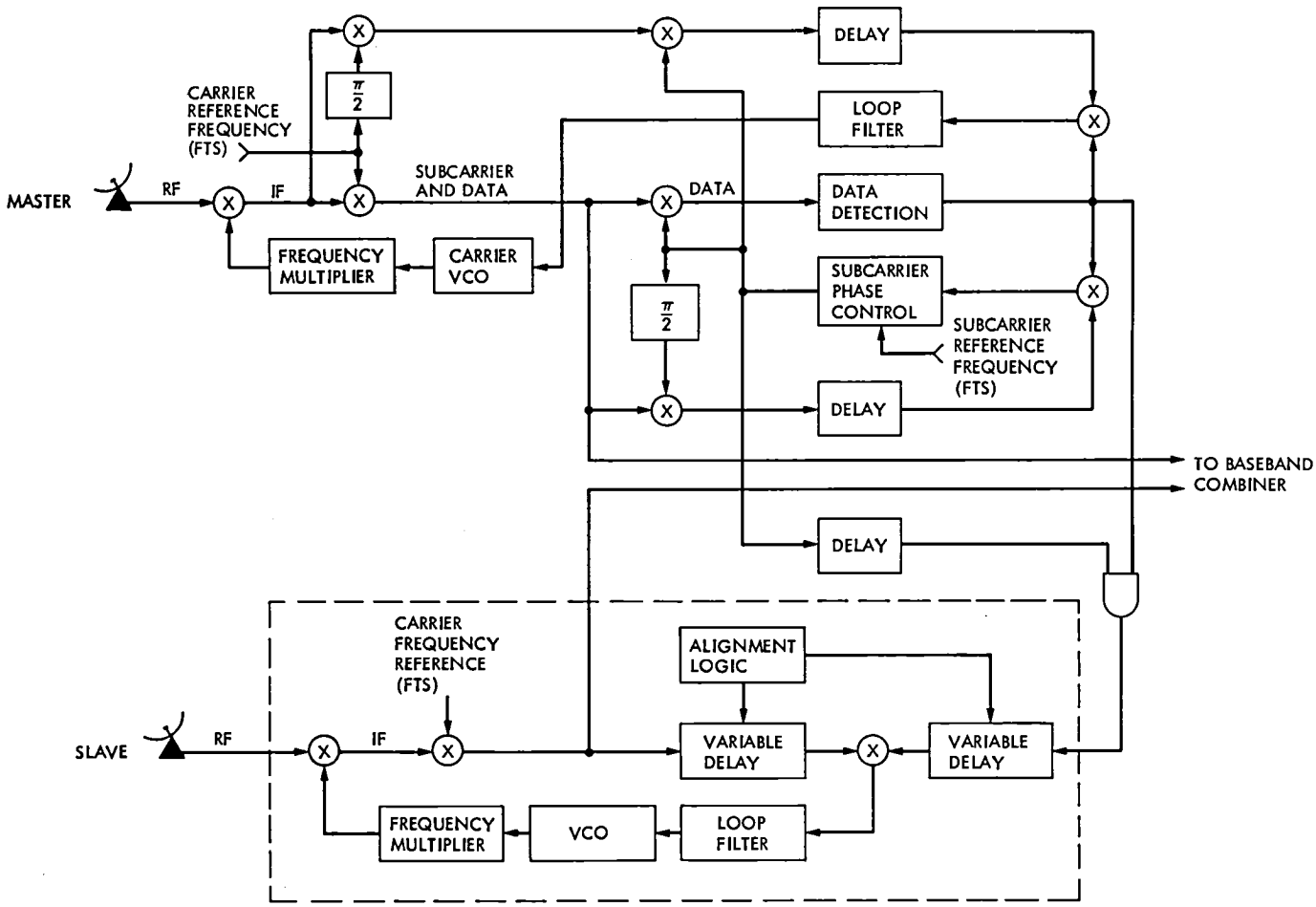

Fig. 8. A possible DSN implementation of SARA

Appendix A
Standard PLL Theory

In a standard phase-locked loop, as shown in Fig. A-1, the input to the loop filter has the form

$$z(t) = A \sin(\phi - \hat{\phi}) + n(t)$$

where ϕ is the phase of the input signal, $\hat{\phi}$ is the loop's estimate of that phase, and $n(t)$ is noise. In our case, $n(t)$ is white Gaussian noise with two-sided spectral density $N_0/2$. If the impulse response of the filter is $f(t)$, then the output of the filter is

$$a(t) = \int_{-\infty}^{\infty} z(x) f(t-x)\, dx + N(t)$$

where $N(t)$ is the filtered noise. It follows that

$$\frac{d\hat{\phi}}{dt}(t) = K_{VCO}\, a(t)$$

where K_{VCO} is the frequency gain associated with the VCO. Upon taking Laplace transforms of the equation,

$$s\,\hat{\phi}(s) = K_{VCO}\, A\, F(s)\, \{\sin[\phi(s) - \hat{\phi}(s)] + N(s)/A\}$$

where F is the Laplace transform of the function f. For small phase errors, this may be linearized to

$$s\,\hat{\phi}(s) = K_{VCO}\, A\, F(s)\, [\phi(s) - \hat{\phi}(s) + N(s)/A]$$

whence

$$\hat{\phi}(s) = \frac{K_{VCO}\, A\, F(s)}{s + K_{VCO}\, A\, F(s)} [\phi(s) + N(s)/A]\ .$$

The function

$$H(s) = \frac{K_{VCO}\, A\, F(s)}{s + K_{VCO}\, A\, F(s)}$$

is called the closed-loop transfer function of the loop.

The phase jitter in the loop is given by

$$\sigma^2 = E\,[\phi - \hat{\phi} - E(\phi - \hat{\phi})]^2$$

where E is the expected value operator. If the phase ϕ of the incoming signal is varying slowly compared to $\hat{\phi}$ (as is the case in SARA), then

$$\begin{aligned}
\sigma^2 &= E[E(\hat{\phi}) - \hat{\phi}]^2 \\
&= E(H(s)\,\phi(s) - H(s)\,[\phi(s) + N(s)/A])^2 \\
&= E[H(s)\,N(s)/A]^2 \\
&= \frac{N_0}{2A^2} \int_{-i\infty}^{i\infty} |H(s)|^2\, ds \\
&= \frac{N_0 B_L}{A^2}
\end{aligned}$$

where

$$2B_L = \int_{-i\infty}^{i\infty} |H(s)|^2\, ds$$

is the closed-loop bandwidth of the system. The loop signal-to-noise ratio is just the reciprocal of the phase jitter,

$$\rho = \frac{A^2}{N_0 B_L}\ .$$

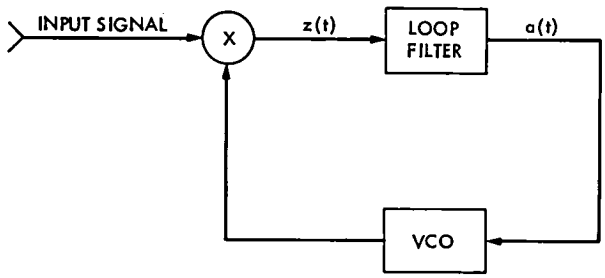

Fig. A-1. A standard phase locked loop (PLL)

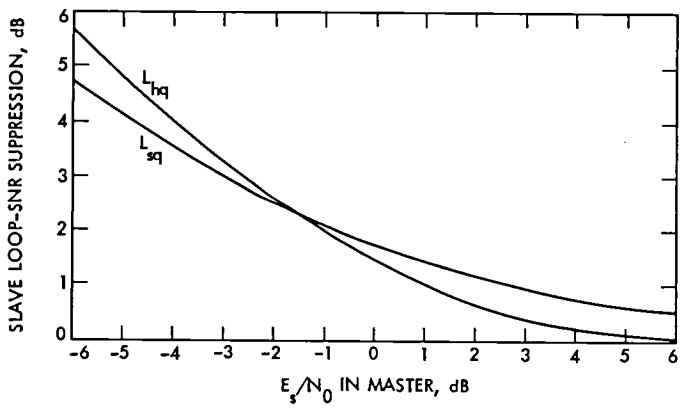

Fig. A-2. Slave loop SNR suppression due to aiding: L_{hq} = suppression with hard-quantization of data estimate; L_{sq} = suppression with soft-quantization of data estimate

Appendix B
Sideband Aiding Without Hard Limiting

In the body of the text, the slave receivers were analyzed assuming a hard-limited estimate of the data from the master was utilized to derive a carrier reference. Since some information is lost in the hard limiting of the output of the data integrator, the question arises as to whether performance could be enhanced if this output itself were used in deriving the slave carrier reference. In the following analysis, all signal references refer to Fig. 2. The incoming signal to the slave has the form

$$x_s(t) = \sqrt{2P_{Ds}}\, d(t) \cos(\omega_0 t + \phi_s) + N_1(t)$$

where the various quantities have the same meanings as in Eq. (1). The carrier estimate from the VCO is

$$r_s(t) = -\sqrt{2}K \sin(\omega_0 t + \hat{\phi}_s).$$

Neglecting the double frequency components, it follows that

$$y_s(t) = \sqrt{P_{Ds}}\, K K'\, d(t) \sin(\phi - \hat{\phi}_s) + N_2(t)$$

where the noise $N_2(t)$ is a white Gaussian process of one-sided spectral density $K K'\, N_0$ W/Hz over the closed-loop bandwidth. If the date detector box of Fig. 1 does not perform the previously described hard-limiting function, then the signal that is sent to the slave for aiding has the form

$$e(t) = d(t - T_s) + n_3(t)$$

where $d(t)$ can be plus or minus one and $n_3(t)$ is a zero mean Gaussian random variable with variance $N_0/(2E_s)$ over the symbol time T_s.

With proper alignment,

$$z_s(t) = \sqrt{P_{Ds}}\, K K' \sin(\phi_s - \hat{\phi}_s) + N_3(t) + N_2(t)\, n_3(t)$$

where $N_3(t) = d(t)\, N_2(t)$ has approximately the same spectral density as $N_2(t)$ over the closed-loop bandwidth. The other noise term, $N_2(t)\, n_3(t)$, has zero mean and spectral density $K K'\, N_0[N_0/(2E_s)]$ over the closed-loop bandwidth since $N_2(t)$ and $n_3(t)$ are independent processes. From standard PLL theory (Appendix A), the loop SNR in the slave for this "soft-quantized" implementation is

$$\rho_s^{(sq)} = \frac{P_{Ds}}{N_0 B_{Ls}} \left(1 + \frac{N_0}{2E_s}\right)^{-1}.$$

The corresponding loop SNR for the "hard-quantized" implementation of SARA (Eq. 3) is

$$\rho_s^{(hq)} = \frac{P_{Ds}}{N_0 B_{Ls}} \operatorname{erf}^2(\sqrt{E_s/N_0}).$$

The corresponding suppression factors are defined by

$$L_{sq} = \left(1 + \frac{N_0}{2E_s}\right)^{-1}$$

and

$$L_{hq} = \operatorname{erf}^2(\sqrt{E_s/N_0}).$$

These are shown plotted as a function of E_s/N_0 in Fig. A-2. The figure shows that the breakpoint occurs at $E_s/N_0 = -1.55$ dB, with the SARA implementation performing better above this value and the soft-quantized better below this value. The range of values expected for a 64-m antenna arrayed with three 34-m antennas during Voyager Uranus encounter is $-3 \text{ dB} < E_s/N_0 < 0 \text{ dB}$. This brackets the breakpoint. If the SARA implementation is used, the slave loop SNR is degraded by at most 0.3 dB. Since slave loop SNRs at Voyager planetary encounters are expected to be above 14 dB with SARA, this degradation is virtually insignificant. Consequently, the relative difficulties in passing a one-bit (hard-quantized) vs a many-bit (soft-quantized) data estimate to the slave receiver will determine which scheme should be implemented.

Capacity Limit of the Noiseless, Energy-Efficient Optical PPM Channel

J. R. Lesh
Communications Systems Research Section

We examine the power-efficient capacity of the noiseless optical PPM channel. It is shown that even though the capacity per photon can be made to increase without bound, the capacity per channel use (for best power efficiency) is always less than 2 nats per symbol. Furthermore, it approaches 2 nats per symbol as the bandwidth expansion factor goes to infinity.

I. Introduction

In Ref. 1 a method was described for maximizing the energy efficiency of a noiseless PPM optical channel subject to simultaneous constraints on the throughput capacity and bandwidth. Specifically, we considered a Q-ary erasure channel often used to model a Q-ary PPM optical communication system. This channel is known to have a capacity C_S per channel use of

$$C_S = \left(1 - e^{-N_S \Delta T}\right) \ln Q \text{ nats/channel use} \qquad (1)$$

where N_S is the intensity of the optical source as seen by the receiver during the PPM pulse (measured in photons/second) and ΔT is the PPM slot width in seconds. Since there are $Q\Delta T$ seconds required for each channel use and each PPM symbol contains, on the average, $N_S \Delta T$ photons, then one can specify the channel capacity in terms of

$$C_T = \frac{C_S}{Q\Delta T} = \frac{1 - e^{-N_S \Delta T}}{\Delta T} \frac{\ln Q}{Q} \text{ nats/second} \qquad (2)$$

and

$$C_{Ph} = \frac{C_S}{N_S \Delta T} = \frac{1 - e^{-N_S \Delta T}}{N_S \Delta T} \ln Q \text{ nats/photon.} \qquad (3)$$

In Ref. 1 we simultaneously fixed the throughput capacity C_T and the slot width (or equivalently the system bandwidth) ΔT. Then, C_{Ph} was plotted as a function of Q. From such plots one could determine Q^*, the value of Q for which the capacity/photon, C_{Ph}, was maximized. In Ref. 1 we also observed that the product $C_T \Delta T Q^*$ was approximately constant. In this article we will examine this latter topic in more detail. This will lead to what can effectively be interpreted as a Shannon limit for the noiseless, power-efficient optical PPM channel.

II. Analysis

We must first determine the requirements on the optimizing value of Q. A necessary condition for Q^* can be obtained by setting the derivative of C_{Ph} with respect to Q equal to zero.

However, before this can be done note that if C_T and ΔT are fixed, any variation of Q must be offset by compensating changes in N_S (see Eq. 2). Thus, we must explicitly show the dependence of N_S on Q. From (2) we have that

$$N_S = -\frac{1}{\Delta T} \ln\left(1 - \frac{C_T \Delta T Q}{\ln Q}\right). \quad (4)$$

Now, substituting (4) into (3) and differentiating we obtain the necessary condition

$$\frac{Z(Q)}{1 - Z(Q)}\left[1 - \frac{1}{\ln Q}\right] + \ln\left[1 - Z(Q)\right]\Big|_{Q=Q^*} = 0 \quad (5)$$

where

$$Z(Q) = \frac{C_T \Delta T Q}{\ln Q}. \quad (6)$$

Thus, once we specify the product $\alpha \triangleq C_T \Delta T$ (which is equivalently the capacity per slot), Q^* can be determined by solving Eq. (5) numerically.

Table 1 shows the results of such calculations for a wide range of α's. Both Q^* and $C_T \Delta T Q^*$ are shown for each α. Clearly, as α decreases there is a compensating increase in Q^* such that for most values of α, $C_T \Delta T Q^*$ is slightly less than 2.

We will now interpret these results in an even more interesting way. From Eqs. (1) and (2) we recognize that $C_T \Delta T Q$ is simply C_S, the channel capacity in nats/channel use. Thus, $C_T \Delta T Q^*$ is nothing more than C_S evaluated at the most energy-efficient operating point. We shall denote this quantity C_S^*. Additionally, we note that if α decreases, either ΔT decreases (bandwidth used increases) for fixed C_T or the required throughput capacity decreases for fixed bandwidth. Both statements are equivalent to saying that the ratio of available bandwidth to information bandwidth is increasing. In Fig. 1 C_S^* is plotted as a function of this bandwidth expansion. In the appendix we prove that $C_S^* < 2$ and approaches 2 in the limit. Thus, we have established the following fundamental property:

For the noiseless optical PPM channel, the most energy-efficient use of the channel results in an information per channel use rate C_S^* of less than 2 nats per channel use. Furthermore, C_S^* approaches 2 nats per channel use as the bandwidth expansion factor approaches ∞.

III. Discussion

It is well known that the capacity of the noiseless PPM channel *measured in nats/photon* can be made infinite by allowing the word size (and hence the bandwidth expansion) to go to infinity. It is therefore surprising that the capacity *in nats/channel use* limits out at 2. This is because, as α decreases, Q^* increases, Z^* goes to zero and the average energy per pulse (i.e., per channel use) also goes to zero as seen by Eq. (4). Thus

$$C_{Ph}^* = \frac{C_S^*}{N_S^* \Delta T}$$

goes to infinity because $N_S^* \Delta T$ goes to zero.

The formulation of C_S^* bears a striking resemblance to the Shannon Limit for the additive white gaussian noise channel. For the AWGN Shannon showed that the energy required to transmit reliably one bit of information, E_b, normalized by the one-sided noise power spectral density N_0 is lower bounded by

$$\frac{E_b}{N_0} > \ln 2$$

and that E_b/N_0 can be made to approach this bound as the bandwidth expansion of the signal approaches ∞. For the noiseless optical PPM Channel, N_0 vanishes (quantum noise does not) so the energy required per bit can be made arbitrarily small. However, the capacity per power efficient use of the channel is still limited and approaches 2 nats/channel use as the bandwidth expands. As in the gaussian channel case, the optical channel limiting behavior is obtained by a sequence of increasing complexity orthogonal (PPM in this case) modulation schemes.

Reference

1. Butman, S. A., Katz, J., and Lesh, J. R., "Practical Limitation on Noiseless Optical Channel Capacity," *TDA Progress Report 42-55*, Jet Propulsion Laboratory, Pasadena, Calif., Feb. 15, 1980.

Table 1. Optimized values of Q and $C_T\Delta TQ$

α	Q^*	$C_T\Delta TQ^*$
10^{0}	0	0
$10^{-0.7}$	7.13	1.42
10^{-1}	15.7	1.57
10^{-2}	176	1.76
10^{-3}	1.83×10^{3}	1.83
10^{-4}	1.87×10^{4}	1.87
10^{-5}	1.89×10^{5}	1.89
10^{-6}	1.91×10^{6}	1.91
10^{-7}	1.92×10^{7}	1.92
10^{-8}	1.93×10^{8}	1.93
10^{-9}	1.94×10^{9}	1.94
10^{-10}	1.94×10^{10}	1.94
10^{-11}	1.95×10^{11}	1.95
10^{-12}	1.95×10^{12}	1.95
10^{-14}	1.96×10^{14}	1.96
10^{-20}	1.97×10^{20}	1.97
10^{-30}	1.98×10^{30}	1.98

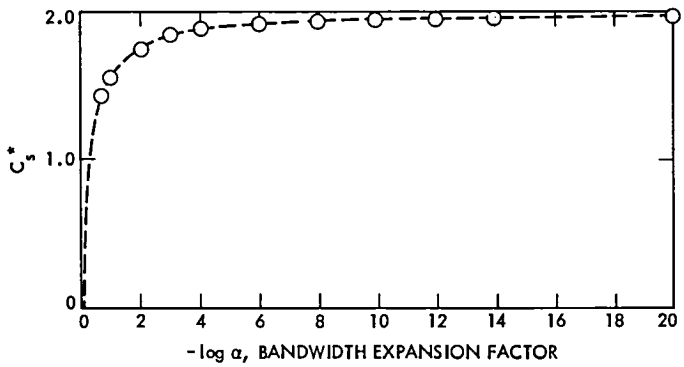

Fig. 1. Variation of energy-efficient channel capacity/channel use with bandwidth expansion

Appendix

We wish to show that $C_S^* < 2$ and asymptotically approaches 2 as $\alpha \to 0$. From (5) we have that the optimizing Q for any α satisfies the relation

$$\frac{Z^*}{1-Z^*}\left[1-\frac{1}{\ln Q^*}\right]+\ln(1-Z^*)=0$$

where

$$Z^* = \frac{C_T \Delta T Q^*}{\ln Q^*} = \frac{C_S^*}{\ln Q^*}.$$

Using this last equality we can rewrite the optimality condition as

$$C_S^* = f(Z^*)$$

where

$$f(Z) = \frac{Z^2}{Z+(1-Z)\ln(1-Z)}$$

From (2) we see that

$$Z = 1 - e^{-N_S \Delta T}$$

so that $0 < Z < 1$. ($Z = 1$ corresponds to infinite energy per pulse whereas $Z = 0$ corresponds to no energy per pulse.) We now claim that $f(Z) < 2$ for all $Z \in (0, 1)$. To prove this we ask if

$$\frac{Z^2}{Z+(1-Z)\ln(1-Z)} \overset{?}{<} 2 \qquad \text{(A-1)}$$

We will prove in a moment that $Z + (1 - Z)\ln(1 - Z) > 0$ for $Z \in (0, 1)$. Thus, (A-1) can be rewritten as

$$\frac{\left(\frac{Z^2}{2}-Z\right)}{1-Z} \overset{?}{<} \ln(1-Z)$$

Now, by expanding $1/1 - Z$ and $\ln(1 - Z)$ in their corresponding power series representations on the open interval of Z yields

$$\left(\frac{Z^2}{2}-Z\right)\sum_{n=0}^{\infty} Z^n \overset{?}{<} -\sum_{n=1}^{\infty}\frac{Z^n}{n}$$

Expanding and cancelling common terms gives

$$\frac{Z^3}{2}+\frac{Z^4}{2}+\frac{Z^5}{2}+\cdots \overset{?}{>} \frac{Z^3}{3}+\frac{Z^4}{4}+\frac{Z^5}{5}+\cdots$$

Each term on the left dominates the corresponding term on the right, so the assertion is clearly true whenever

$$Z+(1-Z)\ln(1-Z) > 0.$$

By the same procedure, this is true if

$$\frac{Z}{1-Z} > -\ln(1-Z)$$

Expanding both sides gives

$$Z+Z^2+Z^3+Z^4+\cdots > Z+\frac{Z^2}{2}+\frac{Z^3}{3}+\frac{Z^4}{4}+\cdots$$

which is clearly true.

Finally, we note that as the bandwidth expansion factor increases, α decreases and $Z \to 0$. This is true whether or not Q^* increases (which it does) by virtue of the fact that $C_T \Delta T Q^*$ is bounded. For this reason we are interested in $f(0)$. By applying L'Hospital's rule twice to $f(Z)$ we see that $f(0)$ does indeed equal 2. Thus, C_S^* is less than 2 and approaches 2 in the limit as $\alpha \to 0$.

On the Group Delay Effect of DSN Microwave Components on Multimegabit Telemetry

P. J. Lee
Communications Systems Research Section

*In this article a method of determining the group delay effect of DSN microwave components on multimegabit telemetry detection is described. That is, when the gain and phase shift characteristics of the overall system between the modulator and demodulator are given, the group delay effect for the intended data rate can be assessed by examining the equation for the recovered signal (equation *) for several rectangular pulse inputs with different duty cycles. For example, the group delay loss of 30 Mbit/sec telemetry with only a Block II X-band maser is less than 0.2 dB even with a 10-MHz center frequency offset.*

I. Introduction

A simplified model for the transmission and reception of multimegabit telemetry is shown in Fig. 1. The modulating signal $x(t)$ is a unit amplitude random binary data signal with bit duration T_b. The phase-modulated signal $y(t)$ is

$$y(t) = K \sin [2\pi f_c t + \phi x(t)]$$

where $f_c(=1/T_c)$ is the carrier frequency ($T_c \ll T_b$), and ϕ is the modulation index. The K in $y(t)$ is the signal amplitude, and will be taken as unity for convenience. If the channel is ideal, then $r(t) = y(t)$,

$$y(t) \cos (2\pi f_c t - \beta_1) = \sin (\phi x(t) + \beta_1) + \sin (4\pi f_c t + \phi x(t) - \beta_1)$$

and

$$\hat{x}(t) = \sin (\phi x(t) + \beta_1)$$

where β_1 is the phase difference between the two reference oscillators at the modulator and demodulator and will also be ignored for later calculations. The modulation index ϕ is *usually* chosen to be less than $\pi/2$ for both maximizing energy of recovered signal $\hat{x}(t)$ and efficient carrier referencing. Since we are only interested in the modulation component, we assume $\phi = \pi/2$.

The overall system between the modulator and demodulator (any combinations of amplifiers, mixers, diplexers, filters, antennas, waveguides, transmission lines, etc.) can be considered as an effective channel bandpass filter. Typical gain and phase shift characteristics of the resulting channel are shown in Fig. 2. Let f_0 be the center of frequency of BPF; $g(f)$ and $\beta(f)$ are the relative gain and phase shift at frequency f to those at f_0. Usually they have symmetry such that

$$g(f_0 - \Delta f) = g(f_0 + \Delta f) \text{ and } \beta(f_0 - \Delta f) = -\beta(f_0 + \Delta f) .$$

It is well known that when a signal $y(t)$ containing components throughout the frequency band of the BPF is divided into a set of narrowband signals, each of these will be subject to a different time delay. Hence the output signal must have a different waveform from the input, and phase distortion appears along with the amplitude distortion.

It is very difficult to analyze the effect of group delay for a random data signal. Hence for analysis we suggest the use of periodic rectangular pulse modulating signals with period $Ts(=1/fs = nT_b)$ and duty cycle $1/n$, for several different n's, instead of the actual random data signal. Since in most cases the bit time-bandwidth product BT_b is not smaller than one, the group delay together with amplitude distortion of one bit affects only itself and its adjacent neighbors.

In the next section, we describe the way of finding the recovered signal $\hat{x}(t)$ including the case where the center frequency of the effective bandpass filter is not matched to the carrier frequency of the incoming signal. Then we show that the group delay effect can be determined by the losses of the integrated values of $\hat{x}(t)$ with group delay compared to those of $\hat{x}(t)$ without group delay.

II. The Recovered Signal x̂(t)

The Fourier series representation of a periodic signal $z(t)$ with period $T(=1/f)$ is

$$z(t) = \sum_{k=-\infty}^{\infty} Z(kf)\, e^{jk2\pi ft} \underset{\mathcal{F}^{-1}}{\overset{\mathcal{F}}{\rightleftharpoons}} Z(kf) = \frac{1}{T}\int_T z(t)\, e^{-jk2\pi ft}\, dt .$$

Let $f_c = mnf_s$ $(T_s = mnT_c)$ where m represents the number of carrier cycles per bit time and n represents the number of bit times over which the bit stream is periodic. The m and n are assumed to be integers so that $y(t)$ is also a periodic signal with period T_s (see Fig. 3) and the Fourier series representation can be used. Then $y(t)$ with $f_c = mnf_s$ and its kth Fourier coefficient $Y_{mn}(kf_s)$ are

$$y(t) = \sin\left[2\pi mnf_s t + \frac{\pi}{2}\, x(t)\right]$$

where

$$x(t) = \begin{cases} 1, 0 \leq |t - \ell Ts| < T_s/2n \\ \\ -1, T_s/2n \leq |t - \ell T_s| < T_s/2 \end{cases} \qquad \ell = 0, \pm 1, \pm 2, \ldots ,$$

and

$$Y_{mn}(kf_s) = \frac{\sin[(mn - k)\pi/n]}{(mn - k)\pi} + \frac{\sin[(mn + k)\pi/n]}{(mn + k)\pi} - \frac{\sin[(mn - k)\pi]}{(mn - k)2\pi} - \frac{\sin[(mn + k)\pi]}{(mn + k)2\pi}$$

Note that

$$Y_{mn}(-kf_s) = Y_{mn}(kf_s) \text{ and } Y_{mn}(mnf_s) \approx \frac{1}{\pi}\left(\frac{1}{n} - \frac{1}{2}\right).$$

Also, when $mn >> \ell > 0$

$$Y_{mn}[(mn + \ell)f_s] \approx Y_{mn}[(mn - \ell)f_s] \approx \frac{\sin(\ell\pi/n)}{\ell\pi}$$

Therefore

$$y(t) \approx \left(\frac{1}{n} - \frac{1}{2}\right)\cos(mn2\pi f_s t) + \sum_{\ell=1}^{m'} \frac{\sin(\ell\pi/n)}{\ell} \{\cos[(mn + \ell)2\pi f_s t] + \cos[(mn - \ell)2\pi f_s t]\}$$

where m' is some number less than $mn/2$. Also

$$r(t) \approx \left(\frac{1}{n} - \frac{1}{2}\right)\cos(mn2\pi f_s t)$$

$$+ \sum_{\ell=1}^{m''} \frac{\sin(\ell\pi/n)}{\ell} \cdot \left(g[(mn + \ell)f_s] \cdot \cos\{(mn + \ell)2\pi f_s t - \beta[(mn + \ell)f_s]\}\right.$$

$$\left. + g[(mn - \ell)f_s] \cdot \cos\{(mn - \ell)2\pi f_s t - \beta[(mn - \ell)f_s]\}\right)$$

where m'' is determined by the bandwidth of BPF which is usually much less than m'.

Then finally

$$\hat{x}(t) = \text{const.} + \sum_{\ell=1}^{m''} \frac{\sin(\ell\pi/n)}{\ell} \left(g[(mn + \ell)f_s] \cos\{\ell 2\pi f_s t - \beta[(mn + \ell)f_s]\}\right.$$

$$\left. + g[(mn - \ell)f_s] \cos\{\ell 2\pi f_s t + \beta[(mn - \ell)f_s]\}\right)$$

$$= \text{const.} + \sum_{\ell=1}^{m''} \frac{\sin(\ell\pi/n)}{\ell} R_{mn}^{(\ell)} \cos\left(\ell 2\pi f_s t - \theta_{mn}^{(\ell)}\right) \qquad (*)$$

where

$$R_{mn}^{(\ell)} = \left(g^2[(mn + \ell)f_s] + g^2[(mn - \ell)f_s] + 2g[(mn - \ell)f_s] \cdot g[(mn - \ell)f_s]\right.$$

$$\left. \cdot \cos\{\beta[(mn + \ell)f_s] + \beta[(mn - \ell)f_s]\}\right)^{1/2}$$

and

$$\theta_{mn}^{(\ell)} = \tan^{-1}\left(\frac{g[(mn+\ell)f_s]\ \sin\ \{\beta[(mn+\ell)f_s]\} - g[(mn-\ell)f_s]\ \sin\ \{\beta[(mn-\ell)f_s]\}}{g[(mn+\ell)f_s]\ \cos\ \{\beta[(mn+\ell)f_s]\} + g[(mn-\ell)f_s]\ \cos\ \{\beta[(mn-\ell)f_s]\}}\right).$$

The additive constant is just the dc bias term. If the BPF has symmetry, i.e., $g(f_0 - \Delta f) = g(f_0 + \Delta f)$ and $\beta(f_0 - \Delta f) = -\beta(f_0 + \Delta f)$ and if $f_0 = f_c$, then $R_{mn}^{(\ell)} = 2g((mn+\ell)f_s)$ and $\theta_{mn}^{(\ell)} = \beta[(mn+\ell)f_s]$.

III. Example and Conclusion

To see the group delay effect on 30 Mbit/sec telemetry with a Block II X-band maser, the shapes of $\hat{x}(t)$ are shown in Figs. 4 and 5 for $n = 2$ and 10 respectively, using the data from Fig. 6 of Ref. 1 and equation (*) with $f_c = f_0$ ($m = 281$). The same signal conditions are repeated in Figs. 6 and 7 with $f_c = f_0 - 15$ MHz. The dotted lines in Fig. 4 to Fig. 7 are the shapes of $\hat{x}(t)$'s without group delay; i.e., only amplitude distortions are considered. When we use an integrator for detection of $\hat{x}(t)$ with integrating duration T_s/n, the losses of the integrated values of $\hat{x}(t)$ with group delay compared to those of $\hat{x}(t)$ without group delay are shown in Fig. 8 for various center frequency offsets. From these observations, we can conclude that the group delay effect on 30 Mbit/sec telemetry with Block II X-band maser is not significantly deleterious even with a substantial center frequency offset.

Reference

1. Trowbridge, D. L., "X-band Traveling Wave Maser Amplifier," in *DSN Progress Report 42-28*, Jet Propulsion Laboratory, Pasadena, Calif., pp. 69-77.

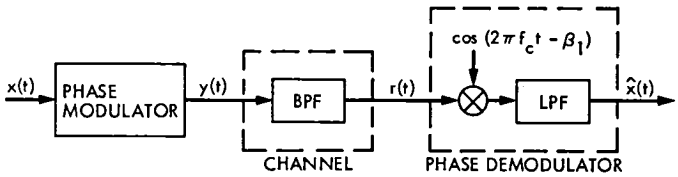

Fig. 1. System model

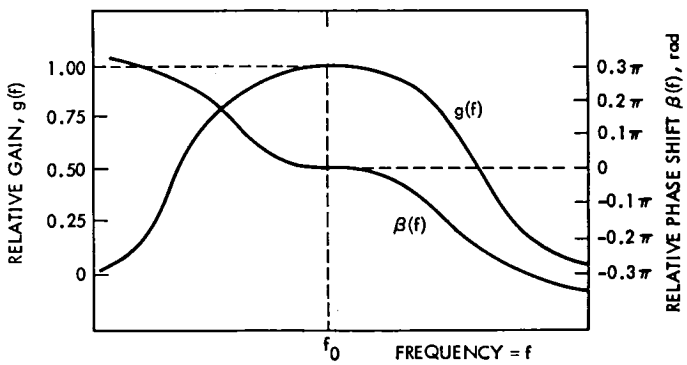

Fig. 2. Typical gain and phase shift characteristics of the channel

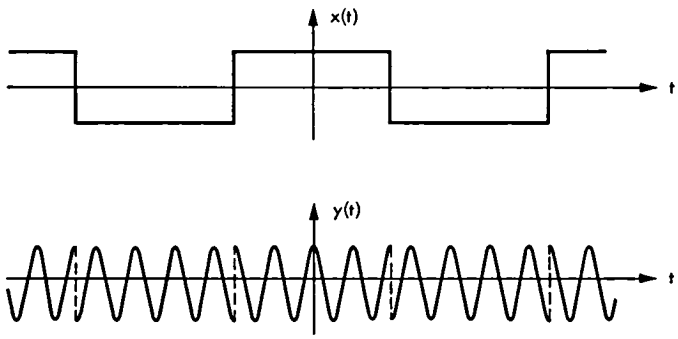

Fig. 3. Example of modulating and modulated signal, $n = 2$, $m = 4$

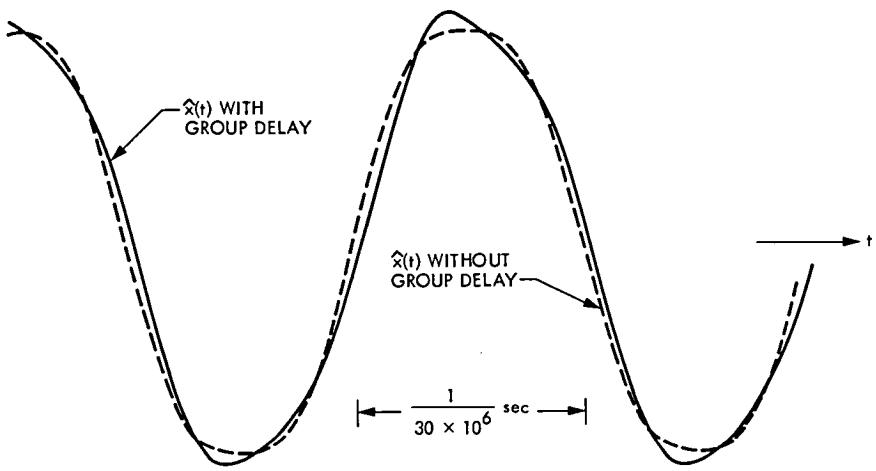

Fig. 4. The shapes of $\hat{x}(t)$, $n = 2$, $f_c = f_0$

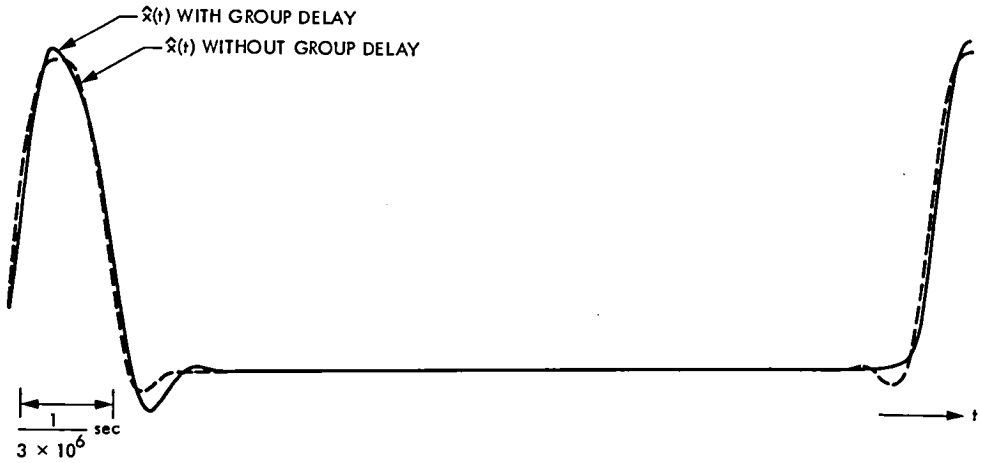

Fig. 5. The shapes of $\hat{x}(t)$, $n = 10$, $f_c = f_0$

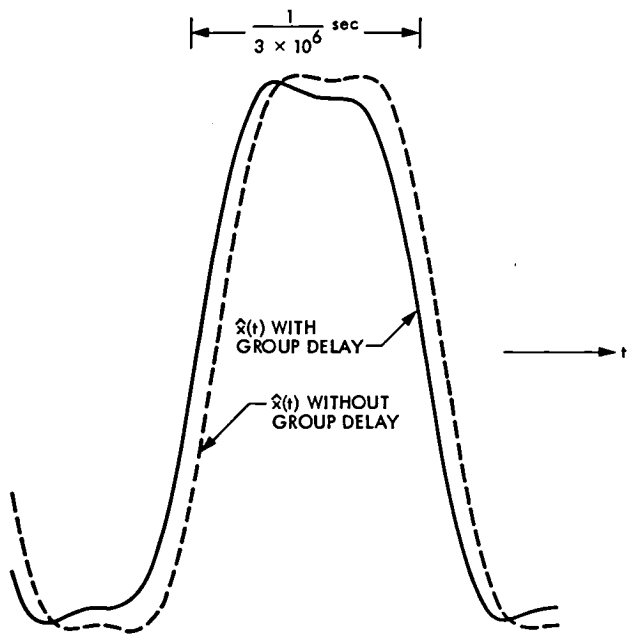

Fig. 6. The shapes of $\hat{x}(t)$, $n = 2$, $f_c = f_0 - 15$ MHz

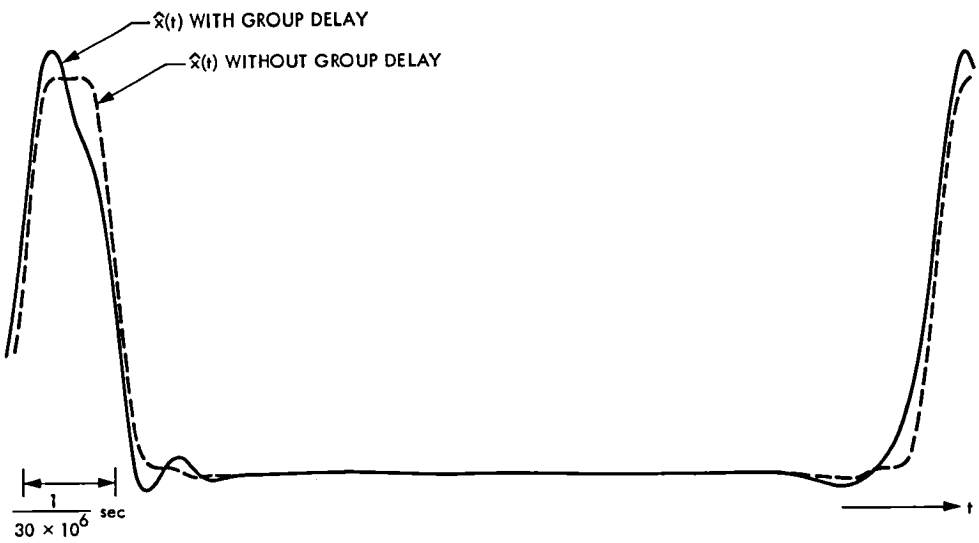

Fig. 7. The shapes of $\hat{x}(t)$, $n = 10$, $f_c = f_0 - 15$ MHz

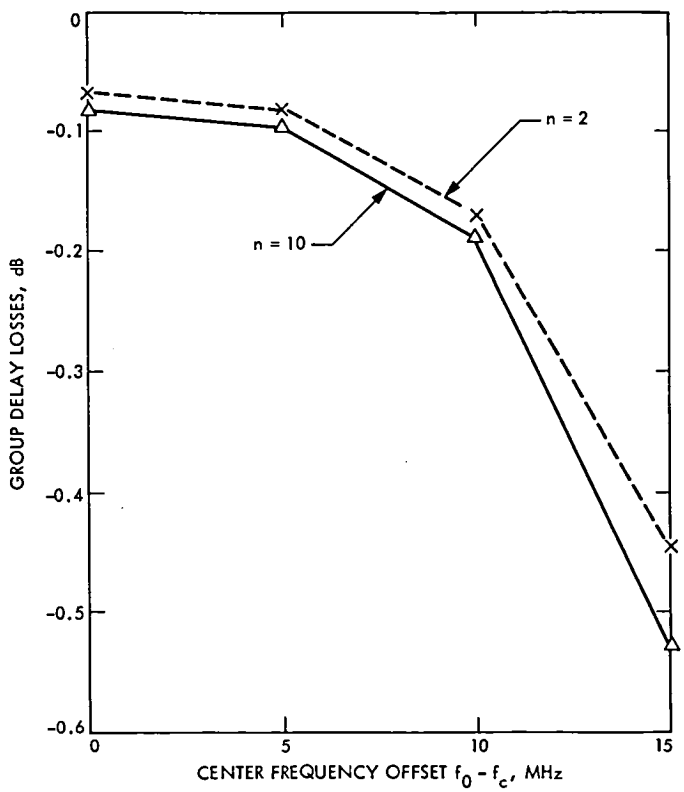

Fig. 8. Group delay losses vs center frequency offset

Improving the Computer-Human Interface: The Qualitative Monitor Display

H. W. Baugh and A. I. Zygielbaum
DSN Data Systems Section

This article describes a new technique for displaying the information needed by DSN operators for monitoring station performance. Known as a "Qualitative Monitor," it presents continuous variables in quasi-analog form on a digital cathode ray tube (CRT) display. Color changes, field reverses and blinking symbols assist the operator in identifying variables that are within acceptable limits and in performing corrective action when needed.

I. Motivation

A significant part of a Deep Space Station (DSS) or Network Operations and Control Center (NOCC) operator's task is to determine if the station equipment is performing as it should, and to take corrective action if it is not. In many cases the assessment of performance requires the operator to study numbers on a CRT display and try to determine if they are within specified limits and if they are rising, falling or stationary. If he decides that a change is needed and starts to move a control, there is the additional question as to which way to move the control to get the desired effect. When the displayed number is a multidigit quantity, and perhaps displayed in "floating-point" format because this made the programmer's task easier, it is sometimes hard to decide just what the variable is doing, especially if the quantity is jittering around a threshold for change of scaling.

The Qualitative Monitor Display presents a key set of variables to the operator in a uniform format which permits him to tell at a glance the state of the information presented and whether any further study is need. Additionally, the display aids the operator in taking any necessary corrective action.

II. History

Although the DSN has made significant progress in the processing of data and in the available throughput of information, it has made significant but unsatisfactory choices in the manner in which information is presented to people operating or monitoring equipment and system performance. In this section, an analog is drawn by examining data presentation in aviation. It seems clear that DSN programmers took technically sound display approaches which did not yield a good computer-human interface.

Through the early history of aviation until about the middle 1950's, instruments were all analog devices: fuel gauges, oil temperature indicators, artificial horizon gyroscopes, etc. Safe operating limits were usually shown by colored striping on the meter face, usually green for "good," and yellow and red for "marginal" and "bad." The pilot could tell with a quick glance at the instruments if all the needles were "in the green" leaving him free to concentrate on maneuvering and navigation.

As the science of digital instrumentation developed, engineers were attracted by digital numeric displays that could

show numbers that represented the variables and could do this more "accurately," i.e., with more resolution. However, it developed that this was not the sort of information the pilot needed for control. When landing or taking off, he wanted to know if the engine was performing within required margins, not the exact temperature at a cylinder head or the precise oil temperature. For the actual control of the plane, a digital presentation of the heading added another complication: if your heading is now 303 degrees, and you want to turn to a heading of 129 degrees, should you turn right or left? In particular, the pilot must be able to immediately tell the attitude of the aircraft in instrument (within clouds) conditions. He could not afford the luxury of a complex interpretation of complex but accurate digital information. Hence the aircraft is instrumented with analog artificial horizons and a circular heading compass.

The numeric displays in aircraft are usually accompanied by bar-graph displays, colored regions on the face of an instrument or "good/bad" signal lights. Although CRT's are now in use on the more sophisticated aircraft, flight control information is presented as the old-fashioned artificial horizon, flight director, or digital gyroscope on the face of the screen. The analog display now is being built of electrons instead of cams, levers, gears, etc. The reason is quite simple: humans can interpret analog displays of complex information much more easily than digital displays.

III. Approach

The Qualitative Monitor Display is made up of a series of horizontal lines. A portion of each line represents the scale of an analog meter, with a rectangular marker moving back and forth like the pointer on an edge-view meter. The "meter" excursions are limited to 21-character positions, corresponding to scale values of −10 to +10 at the edges and 0 at the center. At the left of each line is a label which identifies the variable, for example, NOISE or S-DOPPLER. At the right of the scale, the numeric value is shown with limited scaling, and at the extreme right there is a three-character label that identifies a more detailed display where the operator can find further information on the variable presented in that line. An example of the qualitative display is shown in Fig. 1.

On any particular line, as the marker moves along its scale, it changes color; between +/− 5, it is green for "good" values, between 5 and 7 and between −5 and −7 it is blue for "marginal," and at the outer extremes it is red for "danger" or "bad." The variable being plotted is hard-limited so that off-scale values all show in the most extreme position overlaid with a > or < symbol that blinks to attract the eye. If a variable is so far out of limits that it cannot be reasonably scaled, then it is presented in its log base 10 form with the cursor overlaid with a blinking "?". Thus, the variable will always be visible on the line and the variable's state is always apparent to the operator.

Note that the display format of one quality bar above the other also facilitates rapid interpretation of the state of the entire set of data on the display. If everything is performing within specification, the operator's eye sees the pattern of a vertical column of green cursors. If any single cursor or set of cursors is "out-of-line" it is readily visible. Hence the operator can quickly assess the condition of many diverse data types without exact interpretation of any of them.

IV. An Example

In order to assess the usefulness of the display, an example was programmed into the software supporting the Metric Data Display (MDA), the DSN subsystem which acquires and processes tracking data. Although the display is general and easily implemented on any computer system, the specific example to be examined was programmed on the Modcomp II used as the processor for the MDA.

The variables to be displayed usually have predicted values and tolerances associated with them. To create the display, the variables are first biased so the predicted value will appear at the 0 position on the line and multiplied by a scale factor derived from the tolerance so that the values that are within the tolerance will appear in the middle 50% of the line. The scaled value determines the cursor position. If the value is in the range −10 to +10, the cursor is placed in one of the 21 available character positions on the line. If the value is greater than 10 or less than −10, the cursor is placed at the extreme of the line with a flashing ">" or "<" symbol as appropriate.

If the absolute value exceeds a certain value, recall that its logarithmic representation is presented. For the Modcomp, the maximum integer value is 32767; hence that is the selected limit. If the variable exceeds that value, the line cursor is overlaid with a flashing question mark and the integer part of the exponent is used to position the cursor.

A general-purpose Modcomp II qualitative display subroutine was written and has been tested in the MDA. The subroutine, named QMD, first resets the current DSN display terminal, a Megadata, to put it into a known state. Next, the characters which create the lines are formatted and sent to the terminal. Any line that represents a variable is sent in four parts: the label field with appropriate scaling information; the marker in its appropriate position and with the flashing "?", ">", or "<" overlays; the numerical value of the variable; and the key to a more detailed display. On successive displays, the new marker position is computed and compared against the

old position, and if the marker need not be moved, only the numerical value is updated.

The Fortran program for the Qualitative Monitor Display was developed in two main phases. The first was to establish the exact control sequences needed to command the various Megadata functions, and then to test several alternative schemes for making the line and marker. Various strategies for handling labels and scaling were tried. This phase was performed in the Section 338 laboratory using any of the several Modcomp II machines.

The next phase was to incorporate the features of the QMD in an overlay to be called by the MDA operational program. This necessitated adding QMD to the list of allowable directives, modifying the executive routine so that it would call the appropriate overlay and cataloging the QMD overlay into the load module.

The specific display used to test the QMD concept, shown in Fig. 2, combined variables from two frequently used MDA displays; doppler residuals and pseudo-DRVID were extracted from the appropriate data base. All values were scaled appropriate to their expected values. During tuning operations, however, the doppler residual could be very large. The logarithmic display feature, however, allows the observer to make use of the cursor position, even though it is far off scale, to adjust the received frequency appropriately to "zero" the residual.

The developmental version of the MDA program has been extensively tested in the DSN Data Systems Section lab, on the MDA at CTA 21, and it is expected to be taken to Goldstone for real-life testing.

V. Results and Conclusion

The display has been demonstrated to a broad spectrum of potential DSN users. The comments received have been very encouraging and the authors expect to see the display used for various subsystems in the DSN's Mark IVA (Networks Consolidation) upgrade. DSN consultants in the area of the human interface have reviewed the display and were very pleased with the concept in terms of rapid and concise interpretation of information.

The qualitative monitor technique can be a useful one for the DSN, particularly for monitor and control. The monitor and control operator must observe many data values from many different pieces of equipment and usually in different formats and ranges of values. The qualitative monitor offers a concise and consistent means to observe station operation.

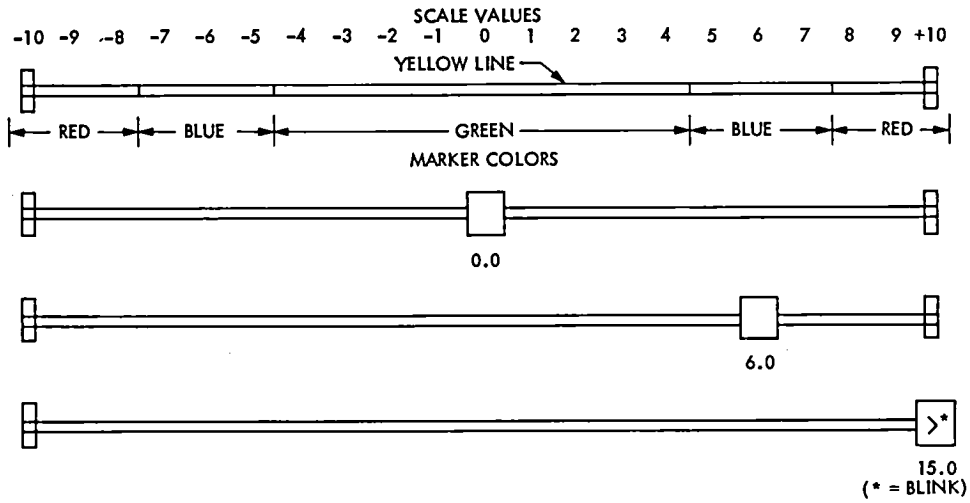

Fig. 1. Qualitative Monitor details

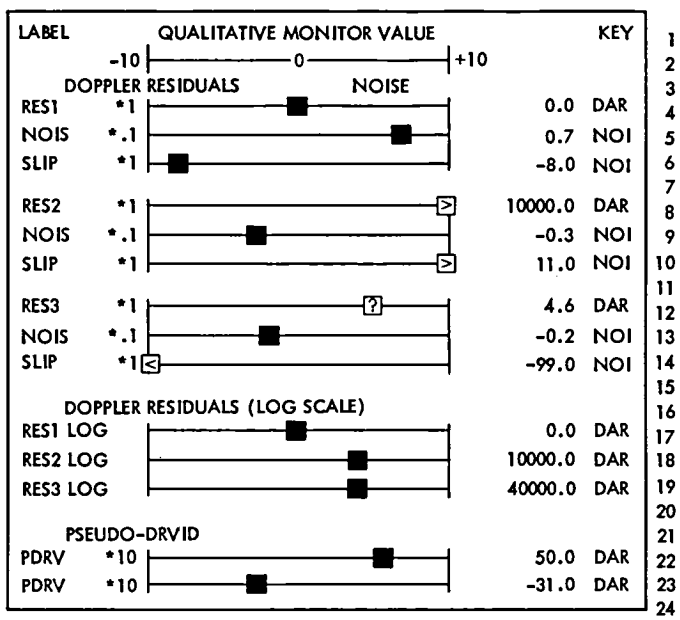

Fig. 2. Qualitative Monitor Display for MDA

Master Timing System Measurements

E. F. Endsley
Communications Systems Research Section

This article describes the test results obtained for the Master Timing System (MTS) manufactured for Goddard Space Flight Center and deployed at the Tracking and Data Relay Satellite Systems Station in White Sands, N.M.

I. Introduction

The tests described in this article were performed on the Master Timing System (MTS) presently in use at the Tracking and Data Relay Satellite Systems (TDRSS) Ground Station at White Sands, N.M. This system was manufactured for Goddard Space Flight Center (GSFC) by TRAK Systems, and is similar in all respects to the master clocks to be utilized in the MK IVA Frequency and Timing Subsystem. Three of these clocks are being purchased by GSFC to be transferred to JPL upon consolidation of the DSN and STDN. The fourth clock is being procured by JPL for future implementation into the DSN. Operating parameters and performance criteria were necessary to ensure subsystem performance and institute design changes for the new clocks.

This report is a composite of two test runs performed on the MTS. The primary tests were conducted on 9 December 1980 through 11 December 1980. These tests were inconclusive due to test equipment malfunctions. Follow-up tests were conducted on 3 February 1981 through 5 February 1981, with all results being verified.

II. Test Descriptions

During the two test runs, the following tests were performed and the results of these tests explained.

(1) *Port-to-port isolation.* The output ports were tested for isolation by observing the output while subjecting the adjacent ports to varying loads, i.e., open load to short circuit. Both amplitude and phase of the test ports were monitored. The first trial of this test produced a complete failure of all outputs; however, subsequent exhaustive tests failed to produce any perturbations. No significant change in amplitude or phase could be measured at any output port.

(2) *Sine wave outputs.* All sine wave outputs were measured for isolation, amplitude and distortion. Distortion was not measured by a qualitative means; however, no distortion could be detected on a 400-MHz storage oscilloscope. All outputs were within specified limits for isolation (<0.1% change in amplitude with any output open or shorted) and amplitude (adjustable from 2 to 5 V(p-p)), and the distortion could be stated to be below five percent.

(3) *Serial time codes.* The serial time codes were clean and within specifications. The amplitude was measured to be 3 V(p-p), and the mark-space ratio was adjustable from 2:1 to 4:1.

(4) *Timing pulses.* Pulse amplitude, wave shape, rise time, and jitter were measured, and the results of each category are presented below. All measurements were made with the output terminated into 50 ohms.

(a) *Amplitude.* The positive or "on" portion of each pulse was measured to be +3.5 ±0.2 V and the negative or "off" portion was +0.2 + 0.1 V.

(b) *Wave shape.* Each set of pulses displayed a different shape, which can best be described by drawings of those waveforms. These drawings are presented in Fig. 1.

(c) *Rise time.* Rise time was measured utilizing a 400-MHz storage oscilloscope. All pulses displayed a rise time of less than 15 nsec between the 10 and 90% points.

(d) *Jitter.* Pulse jitter was measured by redundant systems utilizing an HP 5370 time interval counter and a standard clock with an HP 9835 computer doing the controlling and data reduction for each of the two systems. The in-house frequency standard was utilized for external synchronization of the counters and clocks to insure maximum coherence of each test channel. The standard clocks were measured to have pulse jitter of less than 50 picosec. The pulse output of the MTS was compared against these standard clocks for this test. The data were taken at 100-sample increments and an accumulation of the drift, rms (1σ deviation), positive and negative peak deviation was compiled by the computers. Plots of the reduced data are presented for each of the pulse rates in Figs. 2 through 5. The maximum accumulated values for each pulse rate are given in fractional seconds below:

Pulse rate, pps	RMS jitter	Positive peak jitter	Negative peak jitter
1	4.73×10^{-10}	1.25×10^{-9}	-1.44×10^{-9}
10	4.75×10^{-9}	1.47×10^{-9}	-9.34×10^{-9}
100	8.03×10^{-10}	2.24×10^{-9}	-3.05×10^{-9}
1000	4.41×10^{-9}	1.08×10^{-8}	-9.24×10^{-9}

(e) *Duty cycle.* The pulses displayed at 80% on-time and a 25% off-time duty cycle as specified by Goddard. This can be modified to provide a 10-μsec pulse width to meet JPL requirements.

(f) *Slew rates.* All pulse slew rates were surprisingly accurate; even the 50-nsec/sec rate was exactly 50 nsec per step.

(g) *Pulse coincidence.* The timing coincidence between different output ports was less than 5 nsec between the slowest and fastest pulse of a set (e.g., all 1 pps ports).

(h) *Zero crossing coincidence.* The worst case offset of the zero crossings of the 5-MHz reference signal and the leading or rising edge of the 1 pps was less than 50 nsec.

III. Conclusion

The test results indicate that the system performs within the specifications established by Goddard Space Flight Center. The overall system appears to be well designed and built to a good commercial grade. The Triple Redundant Time Code Generators, whose outputs are majority voted, performed adequately as far as could be determined on an operational system. The automatic fault isolation circuitry could not be tested, due to the system being in an operational situation.

This timing system has been in operation at the TDRSS station for more than one year with no reported failures.

The failure noted in paragraph II (1) apparently was caused by a disturbed reference cable or loose connection external to the clock.

The inconclusive results obtained during the first test run were caused by a perturbation in the data, for which the cause could not be determined. The first test run did not utilize redundant test systems.

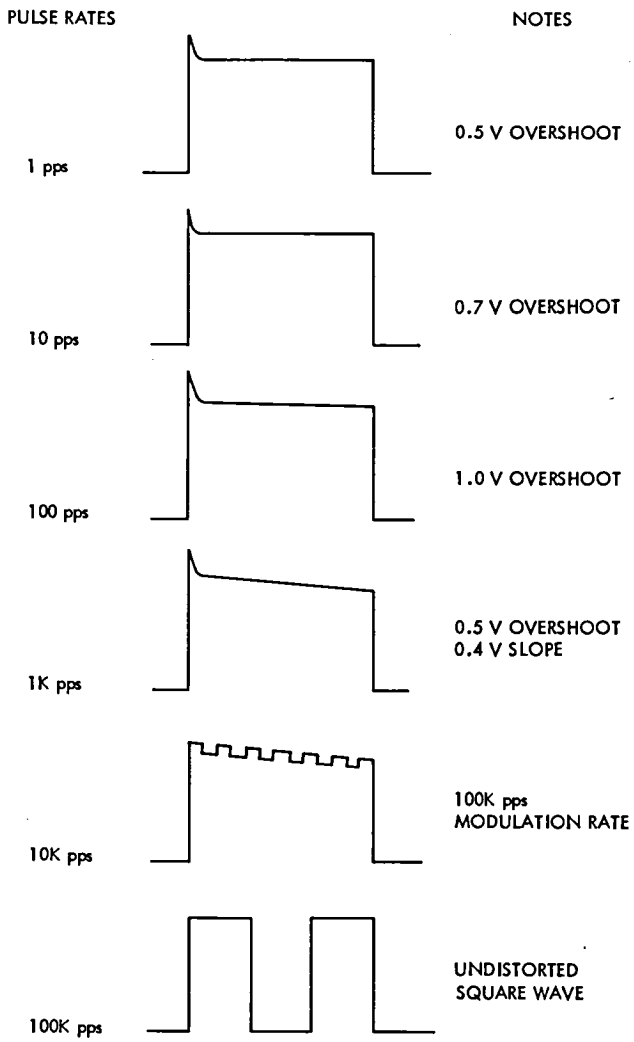

Fig. 1. Timing pulse waveforms

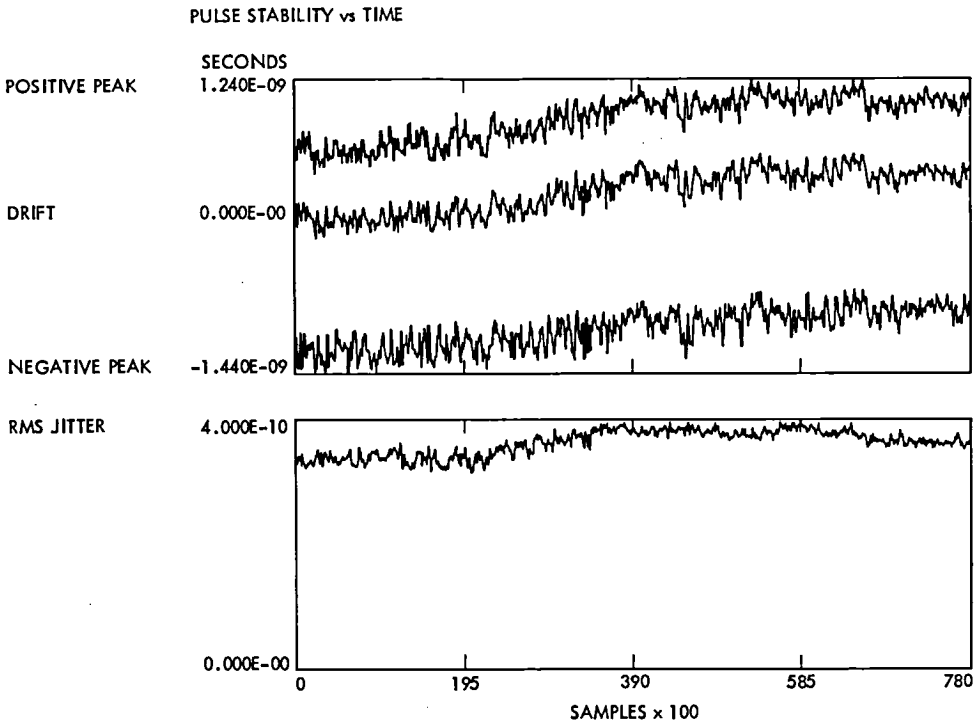

Fig. 2. 1-pps timing pulse

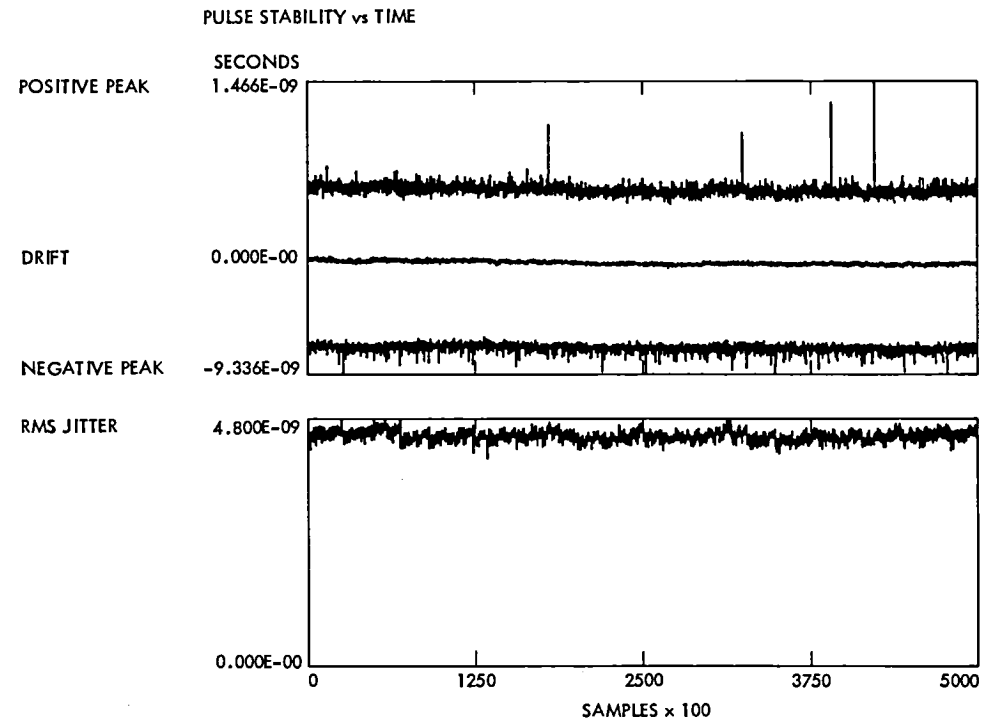

Fig. 3. 10-pps timing pulse

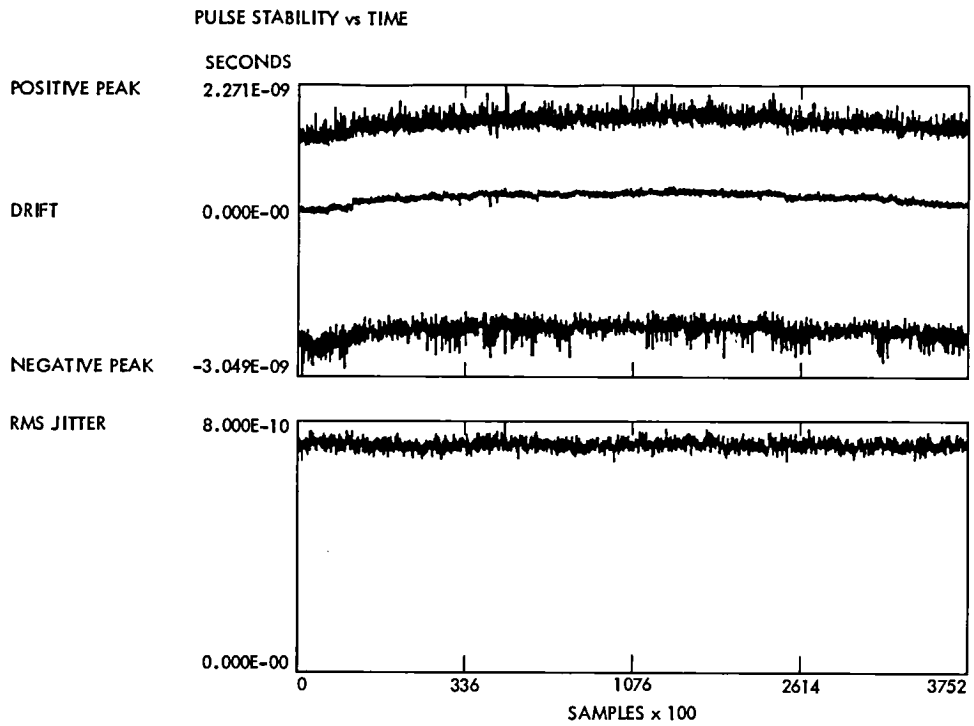

Fig. 4. 100-pps timing pulse

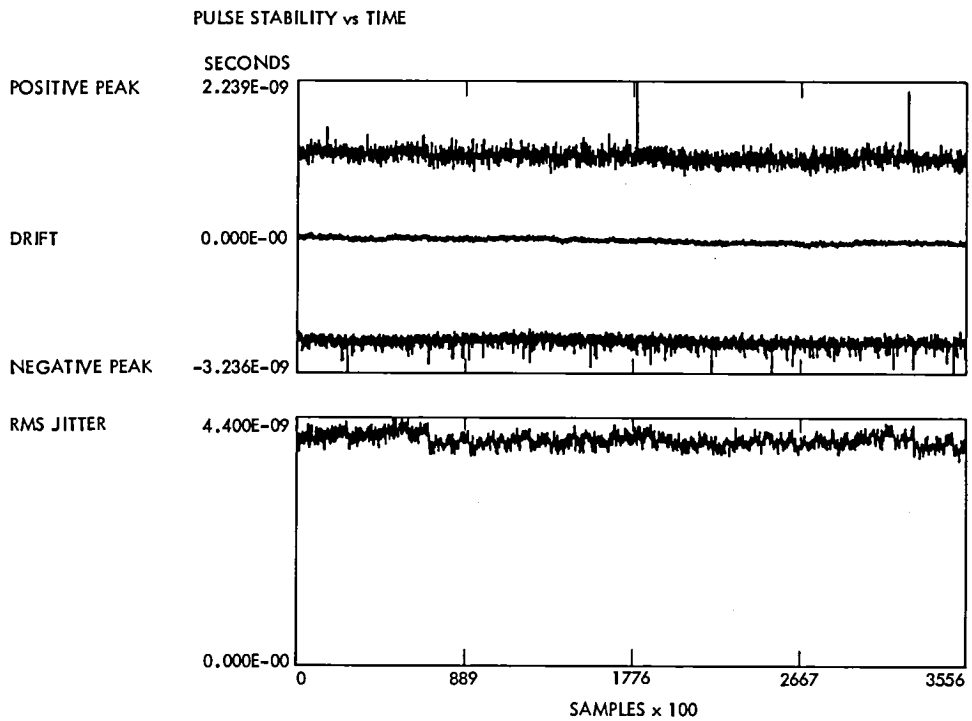

Fig. 5. 1000-pps timing pulse

Optimum Equipment Maintenance/Replacement Policy Part 2. Markov Decision Approach

T. Charng
DSN Engineering Section

This is the second article on the subject of Optimum Equipment Maintenance and/or Replacement Policy which employs the optimization technique called Markov Decision Process. In the first article, dynamic programming was utilized as an alternative optimization technique to determine an optimal policy over a given time period. According to a joint effect of the probabilistic transition of states and the sequence of decision making, the optimal policy is sought such that a set of decisions optimizes the long-run expected average cost (or profit) per unit time. Provision of an alternative measure for the expected long-run total discounted cost is also considered. A computer program based on the concept of the Markov Decision Process was developed and tested. The program code listing, the statement of a sample problem, and the computed results are presented in this report.

I. Introduction

In the first article (*TDA Progress Report 42-66: September and October 1981*), an optimal decision-making policy utilizing the dynamic programming technique was presented. The aim was to make optimal decisions, over a finite number of time periods, regarding the equipment maintenance and/or replacement for a given system.

When a system is required to be existing indefinitely, a best operation policy which gives the optimal long-run cost (or profit) may be estimated by successive approximations with dynamic programming techniques, providing a very large number of time periods is assumed. However, there is no way of knowing when to terminate the successive approximations; there is no procedure for deciding how large a number of time periods is sufficient.

This report presents another decision-making technique to obtain a long-run optimal policy utilizing the Markov Decision Process Concept. The optimal policy is evolved over time periods according to the joint effect of the probabilistic transition of the condition of the system and the sequence of decision making. It is assumed that for a system under consideration, there exists a policy at any time period. The system changes to a new state at the next time period according to a known probability after a decision is made at the present time period and at the present state.

In such decision making, different transition matrixes result, corresponding to the decisions made at each observed time period. Accordingly, a change of state as well as the associated value of cost (or profit) of the system in the next time period is governed by the transition matrix. The optimal

is sought such that the set of decisions made will optimize the long-run expected average cost (or profit) per unit time period.

However, in systems involved with a long time-horizon, the changing time value of money is of importance, and the expected long-run total discounted cost (or profit) should be determined with respect to a specific discount factor. The discount factor a is the present value of one unit money in one time period, expressed as:

$$a = \frac{1}{1+i} \tag{1}$$

where i is the rate of return on the money for one time period. After M periods, a unit of money will be worth a^M.

Derivation of mathematical equations, discussion of the policy-improvement computational algorithm, and a sample problem are presented in the following sections. A computer program employing the discussed algorithm is given in Appendix A.

II. Theoretical Model

Brief descriptions of the Markov Decision Process and the necessary equations are discussed as follows. More detailed derivations of the equations may be found in Refs. 1, 2.

Consider a system which at a particular time period ($t = 1, 2, 3, \ldots$) is in one state i out of M states. The system changes from one of these admissible states, i, to another state, j, ruled by a transition matrix, $P = (p_{ij})$. The elements, p_{ij}, are defined as the probabilities the system is in state j at t, given that it was in state i at $(t-1)$. Further, it is assumed that the transition matrix P is not time-dependent.

Let $q_{ij}(k)$ be the expected cost (or profit) incurred when the system, which originally is in state i, changed after a decision k is made to a state j at the next observed time period. Then,

$$C_{ik} = \sum_{j=1}^{M} q_{ij}(k)\, p_{ij}(k) \tag{2}$$

where C_{ik} is the cost incurred at the first observed time period as a result of the current state i and the decision $D_i(R) = k$ when operating under policy R.

By introducing $V_i^N(R)$ as the total expected cost of a system starting in state i (at the first observed time period) and evolving for N time periods following a policy R, the recursive equation can be written as

$$V_i^N(R) = C_{ik} + \sum_{j=1}^{M} p_{ij}(k)\, V_j^{(N-1)}(R) \tag{3}$$

The second term on the right-hand side of Eq. (3) is the total expected cost of the system evolving over the remaining $(N-1)$ time periods.

Let $g(R)$ be the long-run expected average cost per unit time following a policy R. As one of the Markovian properties, it can be shown that the $g(R)$ is independent of the starting state i as the number of time periods N approaches infinity. Hence, $V_i^N(R)$ may be approximated by

$$V_i^N(R) \cong N\, g(R) + V_i(R) \tag{4}$$

where $V_i(R)$ can be interpreted as the effect on the total expected cost due to starting in state i. Thus, from Eq. (4)

$$V_i^N(R) - V_j^N(R) \cong V_i(R) - V_j(R) \tag{5}$$

the term $[V_i(R) - V_j(R)]$ is a measure of the effect of starting in state i rather than state j. Substituting the linear, approximate relations of Eqs. (4, 5) into Eq. (3) leads to the recursive equation

$$g(R) + V_i(R) = C_{ik} + \sum_{j=1}^{M} p_{ij}(k)\, V_j(R) \tag{6}$$

Equation (6) represents one of the M equations corresponding to the state i for $i = 1, 2, \ldots, M$.

When a system operates according to the Markov chain, there are needed $(M+1)$ values of $g(R)$, $V_1(R)$, $V_2(R)$, $\ldots$, $V_M(R)$ which satisfy the set of M equations of the form Eq. (6). Note that there are M equations and $(M+1)$ unknowns; one of the unknowns, say $V_M(R)$, can be arbitrarily set to equal zero. Following a given policy R, the corresponding values of $g(R)$, $V_1(R)$, $V_2(R)$, $\ldots$, $V_{(M-1)}(R)$ can then be obtained by solving the set of M simultaneous linear equations.

In principle, all policies can be enumerated to find the policy which optimizes the $g(R)$. However, even for a moderate number of states and decisions, this enumeration

technique is cumbersome. A different approach called Policy-Improvement can be used to evaluate policies and find the optimal set of decisions without a complete enumeration. The mechanism of this algorithm is presented in the next section.

III. Computational Algorithm

The Policy-Improvement algorithm consists of two steps: the Value-Determination step and the Policy-Improvement step. These steps are described as follows.

(1) Value-Determination Step: For an arbitrary policy R_1 (with decisions $D_i(R_1) = k_1$, and the corresponding values of $p_{ij}(k_1)$, C_{ik_1}, and $V_M(R_1) = 0$), this step solves the set of M equations of Eq. (6), or

$$g(R_1) + V_i(R_1) = C_{ik} + \sum_{j=1}^{M} p_{ij}(k_1)\, V_j(R_1) \qquad (7)$$

for $i = 1, 2, \ldots, M$. Hence, values of the $g(R_1)$, $V_1(R_1)$, $V_2(R_1), \ldots, V_{(M-1)}(R_1)$ are obtained under policy R_1.

(2) Policy-Improvement Step: Using the above calculated values of the V's, find the alternative policy R_2 such that for each state i, $D_i(R_2) = k_2$ is the decision which optimizes $g(R_2)$, with

$$g(R_2) = C_{ik} + \sum_{j=1}^{M} p_{ij}(k_2)\, V_j(R_1) - V_i(R_1) \qquad (8)$$

That is, for each state $i = 1, 2, \ldots, M$, find the appropriate value of k_2 such that

$$\underset{k_2 = 1, 2, \ldots, K}{\text{OPTIMUM}} \quad [g(R_2)] \qquad (9)$$

In turn, let $D_i(R_2)$ be equal to the optimal value of k_2, which defines a new policy R_2.

Using the new policy R_2, the Value-Determination step is repeated. This iterative procedure continues until two successive iterations lead to identical policies, which signifies that the optimal policy has been obtained.

If the expected long-run total discounted cost is of interest, the above algorithm can be used with a modification to the recursive equation Eq. (6). With a specified discount factor a, the recursive relation of Eq. (6) can be modified as

$$V_i(R) = C_{ik} + a \sum_{j=1}^{M} p_{ij}(k)\, V_j(R) \qquad (10)$$

for $i = 1, 2, \ldots, M$. Here, the $V_i(R)$ is the expected long-run total discounted cost of the system starting in state i and continuing indefinitely. The $V_i(R)$ can be evaluated in a similar fashion as computing the average cost.

A computer program is written to incorporate both the average cost of Eq. (6) and the discount cost of Eq. (10). The optimal policy is determined utilizing the Policy-Improvement algorithm. This BASIC program code is presented in Appendix A. A sample problem, adapted from Ref. 2 and presented in the next section, is used for testing purposes. The calculated results of both the averaged cost and the discounted cost are presented in Figs. 1 and 2, respectively.

IV. Sample Problem

For the purpose of testing the computer program, a sample problem is taken from Ref. 2 and summarized as follows.

The condition of a given system is inspected and classified into one of four possible states as shown in Table 1. It is also assumed that the state of the system evolves according to some known probabilistic transition matrix given in Table 2. After each periodic inspection of the system, a decision must be made as to which action to take: Decision 1 is doing nothing; Decision 2 is overhauling the system; Decision 3 is replacing the system.

In addition, the following assumptions are made:

(1) When the system becomes inoperable (State 4) and replaced (Decision 3), the system is found to be in State 1 at the time of regular inspection. It is assumed that the total cost incurred when the system is in State 4 is the sum of a replacement cost of \$4000 and a cost of lost production of \$2000.

(2) When the system is overhauled, the system is returned to State 2 (operable with minor deterioration) at the time of regular inspection at the end of next time period. The cost of the overhaul process is taken as \$2000 and requires one time period to complete.

(3) When the system is in States 2 or 3, defective items may be produced during the following operating period. The expected costs due to producing defective items are \$1000 when the system is operable with minor deterioration and \$3000 when the system is operable with major deterioration.

(4) The total expected cost incurred per one time period depends on the state the system is in and the decision made. The total expected costs (the maintenance cost, the cost due to producing defective items, and the cost from lost production) are tabulated in Table 3.

The above information completed the necessary inputs to the computer program. Figure 1 presents the optimal policies and the expected average cost of the sample problem. As the result of the Markov Decision Process, an average cost of $1667 can be expected when the policy is to do nothing when the system is found to be in States 1 and 2, to overhauling the system when it is in State 3, and to replace the system when it is in State 4.

In the second case, as presented in Fig. 2, an interest rate of 11% (or discount factor of 0.9) was assigned. However, with the same policy as in Case 1, a discounted cost of $14,950 can be expected if the system started in State 1, $16,260 if it started in State 2, etc.

V. Summary

The Policy-Improvement algorithm using a Markov Decision Process is incorporated in a computer program and tested with a sample problem on a Hewlett-Packard 2647A terminal. This computer program is capable of finding the best maintenance policy with respect to an optimal long-run average cost or the long-run discounted cost for a system with known transition probabilities.

From the standpoint of management and operation, the algorithm provides a useful tool in obtaining an optimal maintenance schedule which gives the best return on capital invested.

Acknowledgment

The author thanks Dr. F. L. Lansing, who made a number of helpful suggestions in the study preparation.

References

1. Bellman, R. E., and Dreyfus, S. E., *Applied Dynamic Programming*, Princeton University Press, Princeton, N.J., 1962.
2. Hillies, F. S., and Lieberman, G. J., *Introduction to Operations Research*, 3rd Edition, Holden-Day, Inc., San Francisco, Calif., 1980.

Table 1. States of the system

State	Condition
1	Good as new
2	Operable with minor deterioration
3	Operable with major deterioration
4	Inoperable

Table 2. Transition matrix of the system

State	1	2	3	4
1	0	7/8	1/16	1/16
2	0	3/4	1/8	1/8
3	0	0	1/2	1/2
4	0	0	0	1

Table 3. Total expected cost per one time period

	Decision		
State	1	2	3
1	0	$4000	$6000
2	$1000	$4000	$6000
3	$3000	$4000	$6000
4	–	–	$6000

```
* * * * * INPUT INFORMATION * * * * *


MSTATE      4
NDECISION   3
MAXTRIAL    10
MAXIMUM     0
DISCOUNT    0

STATE       DECISION   TIE-BREAKER
  I           D(I)       TIED(I)
-----       --------   -----------
 1            1           0
 2            1           0
 3            1           0
 4            3           0


* * * * * * *   FINAL RESULTS   * * * * * * *



LONG-TERM AVERAGE COST/RETURN= 1666.67

STATE       POLICY     VALUE
-----       ------     -----
 1            1         1666.67
 2            1         1666.67
 3            2         1666.67
 4            3         1666.67
```

Fig. 1. Expected average cost

```
* * * * * INPUT INFORMATION * * * * *


MSTATE      4
NDECISION   3
MAXTRIAL    10
MAXIMUM     0
DISCOUNT    11.1111

STATE       DECISION   TIE-BREAKER
  I           D(I)       TIED(I)
-----       --------   ------------
 1           1          0
 2           1          0
 3           1          0
 4           3          0


* * * * * * *   FINAL RESULTS   * * * * * * *




STATE       POLICY     VALUE
-----       ------     -----
 1           1          14948.6
 2           1          16261.6
 3           2          18635.5
 4           3          19453.7
```

Fig. 2. Expected discounted cost

Appendix A

Computer Program Listing

```
1 REM.....REM
2 REM.....REM
3 REM.....          EQUIPMENT MAINTENANCE POLICY          .....REM
4 REM.....          MARKOVIAN DECISION ALGORITHM          .....REM
5 REM.....                                                .....REM
6 REM.....REM
10 DIM Irow(10),Jcol(10),Jord(10),Y(10)
11 DIM Dd(10),D(10),P(5,5,5),R(5,5,5),Sum(5,5),Tied(10),Q(5,5)
15 LONG A(11,11),X(10),Eps,Simul
16 INTEGER D,Dd,Trial,Tied
20 REM
100 REM.....  BEGIN OF DATA LIST  .....REM
102 DATA 0,6                    !  ASSIGN I/O DEVICES
105 DATA 0                      !  PRINTOUT OPTION
110 DATA 4                      !  NUMBER OF STATES IN CONSIDERATION
120 DATA 3                      !  NUMBER OF DECISION ALTERNATIVES
130 DATA 0                      !  MAXIMIZE COST/RETURN IF >=1
140 DATA 10                     !   MAXIMUM TRIALS ALLOWED
150 DATA 11.1111                !  DISCOUNT RATE IN WHOLE NUMBER
160 REM.....  PROBABILITY MATRIX,  P(I,J,K)  .....REM
170 DATA 0,.875,.0625,.0625
180 DATA 0,1,0,0
190 DATA 1,0,0,0
200 DATA 0,.75,.125,.125
210 DATA 0,1,0,0
220 DATA 1,0,0,0
230 DATA 0,0,.5,.5
240 DATA 0,1,0,0
250 DATA 1,0,0,0
260 DATA 0,0,0,1
262 DATA 0,1,0,0
264 DATA 1,0,0,0
270 REM.....  COST/RETURN MATRIX ( R(I,J,K) )  .....REM
280 REM     DATA 0,0,0,00
290 REM     DATA 0,4000,0,0
300 REM     DATA 6000,0,0,0
310 REM     DATA 0,1000,1000,1000
320 REM     DATA 0,4000,0,0
322 REM     DATA 6000,0,0,0
330 REM     DATA 0,0,3000,3000
340 REM     DATA 0,4000,0,0
350 REM     DATA 6000,0,0,0
360 REM     DATA 0,0,0,1.E30
370 REM     DATA 0,1.E30,0,0
380 REM     DATA 6000,0,0,0
381 REM.....  COST/RETURN MATRIX, Q(I,K)=(P(I,J,K)*R(I,J,K).REM
382 DATA 0,4000,6000
383 DATA 1000,4000,6000
384 DATA 3000,4000,6000
385 DATA 1E30,1E30,6000
390 REM.....  TIE-BREAKER, TIED(I)  .....REM
395 DATA 0,0,0,0
400 REM.....  INITIAL POLICY, D(I)  .....REM
410 DATA 1,1,1,3
500 REM.....  END OF DATA LIST  .....REM
998 REM                                                   REM
```

```
1000 REM.............  GENERAL INPUT  ..............................REM
1005 READ Ki,Ko
1010 REM.............  ASSIGN READ/PRINT FILES  ....................REM
1015 ASSIGN "OUTPUT" TO #Ko
1020 IF Ki<=0 THEN 1190
1025 ASSIGN "INPUT" TO #Ki
1030 READ #Ki;Iprint
1035 READ #Ki;Mstate
1040 READ #Ki;Ndecision
1045 READ #Ki;Maxi
1050 READ #Ki;Maxtrial
1055 READ #Ki;Discount
1060 REM.............  INPUT TRANSITION MATRIX  ....................REM
1065 FOR I=1 TO Mstate
1070 FOR K=1 TO Ndecision
1075 FOR J=1 TO Mstate
1080 READ #Ki;P(I,J,K)
1085 NEXT J
1090 NEXT K
1095 NEXT I
1100 REM.............  INPUT COST/PROFIT MATRIX  ...................REM
1105 FOR I=1 TO Mstate
1110 FOR K=1 TO Ndecision
1115 REM    FOR J=1 TO Mstate
1120 REM    READ #5;R(I,J,K)
1125 REM    NEXT J
1130 READ #Ki;Q(I,K)
1135 NEXT K
1140 NEXT I
1145 REM.............  INPUT TIE-BREAKER FLAG  .....................REM
1150 FOR I=1 TO Mstate
1155 READ #Ki;Tied(I)
1160 NEXT I
1165 REM.............  INPUT INITIAL POLICY  .......................REM
1170 FOR I=1 TO Mstate
1175 READ #5;D(I)
1180 NEXT I
1185 GOTO 1350
1186 REM.....................................................................REM
1190 READ Iprint
1195 READ Mstate
1200 READ Ndecision
1205 READ Maxi
1210 READ Maxtrial
1215 READ Discount
1220 REM.............  INPUT TRANSITION MATRIX  ....................REM
1225 FOR I=1 TO Mstate
1230 FOR K=1 TO Ndecision
1235 FOR J=1 TO Mstate
1240 READ P(I,J,K)
1245 NEXT J
1250 NEXT K
1255 NEXT I
```

```
1260 REM.............  INPUT COST/PROFIT MATRIX  ..................REM
1265 FOR I=1 TO Mstate
1270 FOR K=1 TO Ndecision
1275 REM    FOR J=1 TO Mstate
1280 REM    READ R(I,J,K)
1285 REM    NEXT J
1290 READ Q(I,K)
1295 NEXT K
1300 NEXT I
1305 REM.............  INPUT TIE-BREAKER FLAG  ..................REM
1310 FOR I=1 TO Mstate
1315 READ Tied(I)
1320 NEXT I
1325 REM.............  INPUT INITIAL POLICY  ....................REM
1330 FOR I=1 TO Mstate
1335 READ D(I)
1340 NEXT I
1345 REM.....................................................REM
1350 FOR I=1 TO Mstate
1355 FOR K=1 TO Ndecision
1360 IF Q(I,K)<>0 THEN 1425
1365 NEXT K
1370 NEXT I
1375 FOR I=1 TO Mstate
1380 FOR K=1 TO Ndecision
1385 Q(I,K)=0
1390 FOR J=1 TO Mstate
1395 Q(I,K)=Q(I,K)+P(I,J,K)*R(I,J,K)
1400 NEXT J
1405 NEXT K
1410 NEXT I
1415 REM.....................................................REM
1420 REM
1425 GOSUB 10205                !  PRINT INPUT INFORMATION
1430 REM
1435 REM.....................................................REM
1440 Discount=1/(1+Discount/100)
2000 REM.....................................................REM
2032 IF Iprint>0 THEN GOSUB 10410
2034 Trial=0
2035 Trial=Trial+1
2036 IF Iprint>0 THEN GOSUB 10510
2050 REM.............  VALUE DETERMINATION  ....................REM
2060 FOR I=1 TO Mstate
2070 K=D(I)
2090 FOR J=1 TO Mstate
2100 A(I,J)=-P(I,J,K)*Discount
2110 IF I=J THEN A(I,J)=1+A(I,J)
2122 NEXT J
2124 IF Discount=1 THEN A(I,Mstate)=1
2125 A(I,Mstate+1)=Q(I,K)
2130 NEXT I
2140 N=Mstate
2141 Indic=1
2142 Eps=1E-20
```

```
2150 IF Iprint>1 THEN GOSUB 10610
2170 GOSUB 5000
2180 IF Discount<1 THEN 2300
2190 G=X(Mstate)
2220 X(Mstate)=0
2300 IF Iprint>0 THEN GOSUB 10710
3010 REM.............  POLICY IMPROVEMENT  .........................REM
3020 FOR I=1 TO Mstate
3025 FOR K=1 TO Ndecision
3026 Sum(I,K)=0
3030 FOR J=1 TO Mstate
3040 Sum(I,K)=Sum(I,K)+P(I,J,K)*X(J)
3041 NEXT J
3042 Sum(I,K)=Sum(I,K)*Discount+Q(I,K)
3054 IF Discount=1 THEN Sum(I,K)=Sum(I,K)-X(I)
3058 NEXT K
3060 E=Sum(I,1)
3070 Dd(I)=1
3106 FOR K=2 TO Ndecision
3110 IF Maxi>0 THEN 3150
3120 IF E<=Sum(I,K) THEN 3170
3130 E=Sum(I,K)
3140 Dd(I)=K
3142 GOTO 3200
3150 IF E>=Sum(I,K) THEN 3170
3160 GOTO 3130
3170 IF Sum(I,K)<>E THEN 3200
3190 IF Tied(I)>0 THEN Dd(I)=K
3200 NEXT K
3202 IF Iprint>0 THEN GOSUB 10810
3310 NEXT I
3320 FOR I=1 TO Mstate
3330 IF D(I)<>Dd(I) THEN 3360
3340 NEXT I
3350 GOTO 10905
3360 IF Iprint>0 THEN GOSUB 11010
3362 FOR I=1 TO Mstate
3370 D(I)=Dd(I)
3380 NEXT I
3390 IF Trial<Maxtrial THEN 2035
3410 GOTO 11110
5000 REM
5005 REM
5006 REM . . . . . FUNCTION SIMUL ( N,A,X,EPS,INDIC,NRC )
5007 REM
5008 REM   INDIC=-1, COMPUTE THE INVERSE OF THE N X N MATRIX
5009 REM   INDIC= 0, THE SET OF EQUATIONS A(N,N)*X(N)=A(N+1,N+1) IS
5010 REM             SOLVED AND THE INVERSE IS COMPUTED
5011 REM   INDIC=+1, THE SET OF EQUATIONS A(N,N)*X(N)=A(N+1,N+1) IS
5012 REM             SOLVED BUT THE INVERSE IS NOT COMPUTED
5013 REM
5014 REM   EPS  =MINIMUM ALLOWABLE VAULE FOR A PIVOT ELEMENT
5015 REM   A    =AUGMENTED MATRIX OF COEFFICIENT, A=A(I,J)
5016 REM
```

```
5017 REM   N     =NUMBER OF ROWS IN A
5018 REM
5019 REM   X     =SOLUTION VECTOR, X=X(I)
5020 REM
5021 Max=N
5022 IF Indic)=0 THEN Max=N+1
5023 REM
5024 REM . . . . . IS N LARGER THAN 50 . . . . .
5025 IF N(=50 THEN 5031
5026 PRINT #6;"     N IS GREATER THAN 50"
5027 Simul=0
5028 RETURN
5029 REM
5030 REM . . . . . BEGIN ELIMINATION PROCEDURE . . . . .
5031 Deter=1
5032 FOR K=1 TO N
5033 Km1=K-1
5034 REM
5035 REM . . . . . SEARCH FOR THE PIVOT ELEMENT . . . . .
5036 Pivot=0
5037 FOR I=1 TO N
5038 FOR J=1 TO N
5039 REM
5040 REM . . . . . SCAN IROW AND JCOL ARRARYS FOR INVALID PIVOT SUBSCRIPTS
5041 IF K=1 THEN 5048
5042 FOR Iscan=1 TO Km1
5043 FOR Jscan=1 TO Km1
5044 IF I=Irow(Iscan) THEN 5052
5045 IF J=Jcol(Jscan) THEN 5052
5046 NEXT Jscan
5047 NEXT Iscan
5048 IF ABS(A(I,J))(=ABS(Pivot) THEN 5052
5049 Pivot=A(I,J)
5050 Irow(K)=I
5051 Jcol(K)=J
5052 NEXT J
5053 NEXT I
5054 REM
5055 REM . . . . . INSURE THAT SELECTED PIVOT IS LARGER THAN EPS . . . . .
5056 IF ABS(Pivot))Eps THEN 5062
5057 PRINT #6;"     ABS(PIVOT)=";ABS(Pivot);" IS LESS THEN ";Eps
5058 Simul=0
5059 RETURN
5060 REM
5061 REM . . . . . UPDATE THE DETERMINANT VALUE . . . . .
5062 Irowk=Irow(K)
5063 Jcolk=Jcol(K)
5064 Deter=Deter*Pivot
5065 REM
5066 REM . . . . . NORMALIZE PIVOT ROW ELEMENTS . . . . .
5067 FOR J=1 TO Max
5068 A(Irowk,J)=A(Irowk,J)/Pivot
5069 NEXT J
5070 REM
```

```
5071 REM . . . . . CARRY OUT ELIMINATION AND DEVELOP INVERSE . . . . .
5072 A(Irowk,Jcolk)=1/Pivot
5073 FOR I=1 TO N
5074 Aijck=A(I,Jcolk)
5075 IF I=Irowk THEN 5080
5076 A(I,Jcolk)=-Aijck/Pivot
5077 FOR J=1 TO Max
5078 IF J<>Jcolk THEN A(I,J)=A(I,J)-Aijck*A(Irowk,J)
5079 NEXT J
5080 NEXT I
5081 NEXT K
5082 REM
5083 REM . . . . . ORDER SOLUTION VALUES (IF ANY) AND CREAT JORD ARRAY
5084 FOR I=1 TO N
5085 Irowi=Irow(I)
5086 Jcoli=Jcol(I)
5087 Jord(Irowi)=Jcoli
5088 IF Indic>=0 THEN X(Jcoli)=A(Irowi,Max)
5089 NEXT I
5090 REM
5091 REM . . . . . ADJUST SIGN OF DETERMINANT
5092 Ich=0
5093 Nm1=N-1
5094 FOR I=1 TO Nm1
5095 Ip1=I+1
5096 FOR J=Ip1 TO N
5097 IF Jord(J))=Jord(I) THEN 5102
5098 Jtemp=Jord(J)
5099 Jord(J)=Jord(I)
5100 Jord(I)=Temp
5101 Ich=Ich+1
5102 NEXT J
5103 NEXT I
5104 IF Ich/2*2<>Ich THEN Deter=-Deter
5105 Simul=Deter
5106 REM
5107 REM . . . . . END OF SUBROUTINE . . . . .
5108 RETURN
5109 REM
10100 REM.....REM
10110 PRINT #Ko
10120 PRINT #Ko
10130 PRINT #Ko
10140 RETURN
10200 REM.....REM
10205 COMMAND "M F H Hp-Ib#1"
10210 PRINT #Ko;LIN(2);TAB(10);"* * * * * INPUT INFORMATION * * * * *"
10220 PRINT #Ko;LIN(2);TAB(10);"MSTATE    ";Mstate
10225 PRINT #Ko;TAB(10);"NDECISION ";Ndecision
10230 PRINT #Ko;TAB(10);"MAXTRIAL  ";Maxtrial
10235 PRINT #Ko;TAB(10);"MAXIMUM   ";Maxi
10240 PRINT #Ko;TAB(10);"DISCOUNT  ";Discount
10250 PRINT #Ko;LIN(1);TAB(10);"STATE","     ";"DECISION","TIE-BREAKER"
10255 PRINT #Ko;TAB(10);"  I  ","     ";"  D(I)  ","  TIED(I)  "
```

```
10260 PRINT #Ko;TAB(10);"-----","     ";"--------","-----------"
10265 FOR I=1 TO Mstate
10270 PRINT #Ko;TAB(10);I,"     ";D(I),Tied(I)
10275 NEXT I
10280 IF Iprint<2 THEN RETURN
10300 PRINT #Ko;LIN(1);TAB(10);"  STATE   "," DECISION "," STATE   "
10302 PRINT #Ko;TAB(10);"  STATE   "," DECISION "," STATE "
10304 PRINT #Ko;TAB(10);"AT CURRENT","AT CURRENT"," AT NEXT  ","PROBABILITY"
10306 PRINT #Ko;TAB(10);"  STAGE   ","   STAGE  "," STAGE   "," P(I,J,K) "
10308 PRINT #Ko;TAB(10);"  ( I )   ","   ( K )  "," ( J )   "," P(I,J,K) "
10310 PRINT #Ko;TAB(10);"----------","----------","----------","-----------"
10312 FOR I=1 TO Mstate
10314 PRINT #Ko
10316 FOR K=1 TO Ndecision
10318 PRINT #Ko
10320 FOR J=1 TO Mstate
10322 PRINT #Ko;TAB(10);I,"",K,J,P(I,J,K)
10324 NEXT J
10326 NEXT K
10328 NEXT I
10330 PRINT #Ko;LIN(2);TAB(10);"  STATE   "," DECISION "
10332 PRINT #Ko;TAB(10);"AT CURRENT","AT CURRENT"
10334 PRINT #Ko;TAB(10);"  STAGE   ","   STAGE  ","COST/PROFIT"
10336 PRINT #Ko;TAB(10);"  ( I )   ","   ( K )  ","   Q(I,K)  "
10338 PRINT #Ko;TAB(10);"----------","----------","-----------"
10340 FOR I=1 TO Mstate
10344 FOR K=1 TO Ndecision
10346 PRINT #Ko;TAB(10);I,"",K,Q(I,K)
10348 NEXT K
10350 PRINT #Ko
10352 NEXT I
10360 RETURN
10400 REM.....................................................................REM
10410 PRINT #Ko;LIN(2);TAB(10);"  * * * * * INTERMEDIATE RESULTS * * * * *"
10420 RETURN
10500 REM.....................................................................REM
10510 PRINT #Ko
10520 PRINT #Ko;" .........  TRIAL =";Trial
10530 RETURN
10600 REM.....................................................................REM
10610 PRINT #Ko
10640 FOR I=1 TO Mstate
10650 FOR J=1 TO Mstate+1 STEP 4
10660 PRINT #Ko;TAB(10);"A(";I;",";J;")=";A(I,J);"A(";I;",";J+1;")=";A(I,J+1);
10665 PRINT #Ko;"A(";I;",";J+2;")=";A(I,J+2);"A(";I;",";J+3;")=";A(I,J+3)
10670 NEXT J
10675 PRINT #Ko
10680 NEXT I
10690 RETURN
10700 REM.....................................................................REM
10710 PRINT #Ko
10720 IF Discount=1 THEN PRINT #Ko;TAB(10);"G      =";G
10730 FOR I=1 TO Mstate
10740 PRINT #Ko;TAB(10);"V(";I;")=";X(I)
10750 NEXT I
```

```
10760 PRINT #Ko
10770 RETURN
10800 REM.....................................................................REM
10810 PRINT #Ko;LIN(1);TAB(10);"STATE","DECISION","VALUE"
10820 PRINT #Ko;TAB(10);"-----","--------","-----"
10830 FOR K=1 TO Ndecision
10840 PRINT #Ko;TAB(10);I,K,Sum(I,K)
10850 NEXT K
10860 RETURN
10900 REM.....................................................................REM
10905 PRINT #Ko;LIN(3);
10910 PRINT #Ko;TAB(10);"* * * * * * *   FINAL RESULTS   * * * * * * * "
10915 PRINT #Ko;LIN(3)
10920 IF Discount=1 THEN PRINT #Ko;TAB(10);"LONG-TERM AVERAGE COST/RETURN=";G
10925 PRINT #Ko;LIN(2);TAB(10);"STATE","     ";"POLICY","VALUE"
10930 PRINT #Ko;TAB(10);"-----","     ";"------","-----"
10935 FOR I=1 TO Mstate
10940 K=D(I)
10945 PRINT #Ko;TAB(10);I,"     ";D(I),Sum(I,K)
10950 NEXT I
10955 GOTO 11210
11000 REM.....................................................................REM
11010 PRINT #Ko;LIN(2)
11012 FOR L=1 TO Mstate
11014 PRINT #Ko;TAB(10);"OLD-D(";L;")=";D(L),"NEW-D(";L;")=";Dd(L)
11016 NEXT L
11020 RETURN
11100 REM.....................................................................REM
11110 PRINT #Ko;LIN(3);TAB(20);"$$$$$$$$$$$$$$$$$$$$$$$$$$$$$$$$$$$$$$$$$$$$$$$"
11120 PRINT #Ko;TAB(20);"EXCEEDED THE MAXIMUM NUMBER OF TRIALS =";Maxtrial
11130 PRINT #Ko;TAB(20);"$$$$$$$$$$$$$$$$$$$$$$$$$$$$$$$$$$$$$$$$$$$$$$$$"
11200 REM.....................................................................REM
11210 PRINT #Ko;LIN(5);TAB(20);"* * * * * END OF TASK * * * * *"
11220 COMMAND "M f h hp-Ib#1"
60000 END
```

Global Positioning System Timing Receivers in the DSN

P.A. Clements
Communications Systems Research Section

The Global Positioning System (GPS) is a worldwide navigation system using a constellation of earth satellites with onboard clocks. The GPS is also usable to transfer time and frequency. JPL has provided part of the funding to the National Bureau of Standards (NBS) to build GPS timing receivers. Preliminary tests with the breadboard receiver at NBS has produced remarkable precision in time and frequency transfer between the United States Naval Observatory (USNO) and NBS. JPL plans to install receivers in the DSN to demonstrate their ability to transfer time and frequency within the DSN and between the DSN and outside agencies.

I. Introduction

JPL is procuring two Global Positioning System (GPS) satellite timing receivers from the National Bureau of Standards (NBS). JPL has funded a large part of the development of the receiver design at NBS. The GPS timing receivers are to be evaluated for use in the DSN as a method of time and frequency transfer among the stations of the DSN, and between the DSN and world time and frequency standards.

JPL plans to demonstrate the use of a GPS timing receiver system as a method of significantly reducing the cost of meeting the functional requirements for time and frequency transfer.

II. The Global Positioning System

The GPS is a Department of Defense worldwide navigation system that uses a constellation of orbiting Earth satellites, each of which carries an onboard clock (Ref. 1). Stored on each space vehicle (SV) is information on its position with respect to an Earth-based rectilinear coordinate system. If this time and position data were transmitted to an Earth-based station with its own clock, then the difference in time, neglecting relativistic effects, would be the propagation delay of the signal. Hence the observer can determine his position as being somewhere on a sphere which has its center at the spacecraft. By viewing three SVs and by having a reasonably good clock, an observer can determine his position exactly. By viewing four SVs, the observer can determine his position using a poor clock.

The GPS satellite configuration calls for 24 SVs. This number has been reduced to 18 due to budgetary considerations. The SVs are distributed in three orbital planes inclined 63° with respect to the Earth's equatorial plane, and offset from each other by 120° longitude. Each SV is in 12-hour prograde orbit. This distribution is meant to maximize the number of SVs visible to an observer anywhere on the earth at any time.

The GPS SV signal is at two frequencies: link 1 at 1575.42 MHz and link 2 at 1227.6 MHz. These frequencies are multiples of 10.23 MHz, namely:

$$\text{link 1} = 1575.42\ \text{MHz} = 10.23\ \text{MHz} \times 154$$

$$\text{link 2} = 1227.6\ \text{MHz} = 10.23\ \text{MHz} \times 120.$$

This is a particularly good frequency region for a couple of reasons. First, there is little use at these frequencies, so it is relatively easy to obtain an allocation. Second, the effects of the ionosphere on the propagation delay are smaller than at lower frequencies.

The GPS SV transmits two PN codes on link 1; they are named the P code and the C/A code. The GPS timing receiver uses only the C/A code. The C/A code is 1023 bits long and is transmitted at a 1023-Mbps rate; hence its duration is 1 ms. Each SV's code is unique so that all the SVs can use the same RF carrier frequency and yet a receiver can pick out a particular SV's signal. The data are transmitted at a 50-bps rate, so there are 20 C/A code sequences for each data bit. The data consist of 4 blocks. Data Block 1 contains the clock corrections for the SV clock with respect to GPS time. Data Block 2 contains ephemeris information for that particular SV. There is a message block that contains any messages that might be needed. Finally Data Block 3 contains an almanac of the locations of all of the SVs in the GPS constellation. The complete message takes 6 seconds to transmit.

III. Description of the Receiver

The NBS GPS timing receiver system consists of three chassis which are rack-mountable and a separate low-noise amplifier and down-converter which are mounted at the antenna. The rack-mountable chassis take a combined vertical rack space of about 18 inches, a keyboard which takes about 4 inches more and a printer which takes about 6 inches.

A 100-MHz local oscillator frequency is sent to the antenna-mounted down-converter. This signal is subsequently multiplied (×15) and mixed with a 1.57542 GHz out of the wide band front end amplifier to produce a 75.42 MHz IF frequency.

The balance of the receiver is what is known as a Tau Dither Delay Lock Receiver (Ref. 1). The receiver has two loops. The inner loop is a delay lock loop. Its function is to lock to the incoming PN code, thereby producing a signal the outer phase lock loop can lock to.

The receiver must perform a cross correlation operation to extract a signal from a particular SV. To do this, the PN code of the particular SV is replicated in the receiver. Then the replicated code is shifted (delayed) until a correlation is found. With correlation, the receiver locks to the code with the delay lock loop and to the signal with a phase lock loop.

IV. Timing and Frequency Transfer

A. Synchronization

One fundamental aspect of time is that of simultaneity.[1] A definition given by NBS for simultaneity is: "Two events are simultaneous if equivalent signals, propagating in a given media, arrive coincidentally at a common point in space which is geometrically an equal distance from the source of each event. In practice a much broader definition is often used for clock synchronization; i.e., two clocks have the same reading in a specific reference frame" (Ref. 2).

If two clocks are beating simultaneously, in a specific reference frame, they are said to be synchronized. All of us have synchronized one clock to another by setting our wristwatch to the mantel clock. We make the time reading (date) of one clock agree with the date of another clock.

If clocks are located some distance from one another, the problems of accurate synchronization become difficult. Of course we use radios and telephones to get the date, but these methods are not usable to transfer the date with an accuracy of microseconds or nanoseconds.

Early in the 17th century Galileo devised a method of date transfer using observations of the moons of Jupiter. The Jovian satellite system is a clock that is observable from any place on the Earth. All one needed was an ephemeris table and a reasonable telescope and he could synchronize any clock on Earth. This is an application of the first definition of simultaneity. Note that every place on Earth is approximately the same distance to Jupiter. This technique was used extensively for over 100 years for map-making; however, it was not usable on ships at sea because of the difficulty of looking through a telescope from a pitching deck.

With good portable cesium clocks the definition of synchronization of widely separated clocks is a "clock trip" from one clock to the other, then back to the first clock. This is called a clock closure. This method invokes the second definition of synchronization. The most careful clock trips take into account the path of the traveling clock to correct for relativistic effects and refer the clocks to the same reference frame

[1] There are three aspects of time: time interval, date (the clock reading), and simultaneity.

(Ref. 3). This is one of the methods presently used in the DSN.[2]

Over the last several years people have been getting back to Galileo's method of using satellites for time transfer. For example NBS has been using the GOES weather satellites for time transfer. The DSN has used a technique of bouncing timing pulses off the Moon. Now both NBS and the United States Naval Observatory (USNO) are using the GPS satellites for time transfer.

The GPS can be used in several ways to accurately transfer time between two or more known locations on the Earth. I shall describe two methods which are planned during the JPL/NBS demonstration.

The first of these two methods is a simultaneous common view (mutual view) of a single GPS satellite. With this technique the common mode ephemeris errors cancel, and the satellite clock error contributes nothing. If the two or more clocks are within 3000 km of each other so that the observation angles are high, one can expect a measurement accuracy of 10 nanoseconds time difference between the observers' clocks. If the propagation and ephemeris errors can be reduced, the accuracy can be reduced to 1 nanosecond.

The specific procedure for a mutual view observation is quite simple. The observers agree to observe a given satellite at a given time. Alernatively, if an observer knows another's observation schedule, he only has to make his schedule agree with the other's. The data of a complete observation of a satellite would include the date of the observation to the second and the time offset from the observer's clock to the GPS clock. At some time later the observers can exchange data.

Ideally an observatory's daily observation schedule would be on sidereal time.[3] This would mean that the SV would appear in the same position in the sky every day at observation time. The advantage of this method is the elimination of variables associated with direction. As the two clocks are separated, the angles of mutual view of the satellites become more shallow. As this happens, the ephemeris and propagation errors become larger, so the measuring accuracy is decreased.

The second method is to make successive observations of the same SV clock (sequential view). The first observer synchronizes his clock with the SV clock when the SV is at a good viewing angle. A second observer then synchronizes his clock to the same SV at some time which is less than 12 hours later than the first observation, and when the SV is at a good viewing angle for him. If the SV that is observed has a cesium clock, then the date uncertainty will be about 5 ns over a 12-hour period. The ephemeris errors will tend to cancel because the same SV is used.

As in the case of portable clock trips, the relativisitic effect needs to be taken into account for a precision time transfer (Ref. 3).

B. Syntonization

Closely related to synchronization is the concept of syntonization. Syntonization is the act of putting two oscillators on the same frequency (tone). It is a musical term and is found in some dictionaries so defined. The term syntonization accuracy refers to a number $(f - f_0)/f_0 = \Delta f/f$, which is a measure of how close the frequency of one oscillator is to that of another, where f_0 is the frequency of the reference oscillator and f is the frequency of the measured oscillator.

As presently conceived, the operation of the GPS receiver would be used to take a reading of time offset once a day between two clocks. If clock A's oscillator is running fast with respect to clock B's oscillator, then clock A's value of date will advance with respect to clock B's value of date. Therefore, by taking daily clock offset readings one can determine the difference in rates between the two clocks oscillators, given $\Delta f/f$.

V. Present Performance of the Receivers

At present NBS and USNO are conducting daily mutual view observations of SVs. This means that NBS acquires and receives data from the same SV at the same time USNO is doing so. NBS is using a breadboard version of a receiver of NBS design. USNO is using a receiver purchased from Stanford Telecommunications Incorporated (STI).

USNO observes five SVs daily. The offsets between GPS time and USNO Master Clock (MC) are published weekly in a USNO Bulletin (Fig. 1). In addition, the data are available daily by telephone using a MODEM and a terminal. The data consist of the offset in nanoseconds between GPS time calculated by each satellite and the time of the MC. Also the data includes the date to the second that the data were taken.

[2]In addition to clock closures, VLBI methods are now being used between the DSN stations. In Spain the Loran-C navigation system is used and in Australia television synchronization signals are used to transfer time.

[3]Sidereal time is the time used by astronomers. It uses observations on the fixed stars rather than the Sun. A sidereal day is about 4 minutes shorter than a mean solar day; hence the time of observation would advance about 4 minutes per day mean solar time.

The USNO measures the offset between GPS time and MC. The MC is the physical realization of UTC (USNO)[4] and is designated UTC (USNO, MC). Because of the present method of steering the MC, the time scale UTC (USNO, MC) differs from UTC (USNO) by some small amount (several nanoseconds). This offset is available on the telephone on a daily basis in the same way as the GPS data.

NBS observes four SVs daily, scheduled so that it has a mutual view of USNO. The SVs are SV-5 and SV-9, which have cesium clocks on board, and SV-6 and SV-8 which have rubidium clocks. NBS measures the offset between GPS time by each SV and NBS clock 9 [(UTC (NBS, CL9))].

In the same way, UTC (USNO, MC) has some offset from UTC (USNO), UTC (NBS, C19) as some small offset from UTC (NBS). These data are not published but are available from NBS.

There is a bit of a scheduling problem in the mutual view exercise between NBS and USNO. The NBS receiver corrects its viewing time 4 minutes a day to make up the difference between mean solar time and sidereal time. The USNO receiver on the other hand is corrected 28 minutes once a week. This means there is a slight departure from sidereal time as the week wears on. I understand that USNO will eventually operate the receiver on sidereal time. At the present NBS has to change the schedule every day.

The big advantage of viewing the SV on a sidereal schedule is that it will appear in the same position in the sky every day. This is important if there are any multipath problems and with respect to syntonization. To measure frequency offset, the important thing is change in time. If we look at the SV in the same place in the sky every day, a lot of variables cancel.

Present measurements between USNO and NBS have shown that the short-term characteristics of the GPS signal have white noise phase modulation (white PM) as a limiting noise process. The method of determining this was a new technique called the Modified Allan Variance (mod $\sigma^2 y(\tau)$). Mod $\sigma^2 y(\tau)$ as its name implies is a modification of the traditional method of characterizing frequency stability, the Allan Variance. Using mod $\sigma^2(\tau)$, one can easily distinguish between white PM and flicker phase noise (Flicker PM). Flicker PM is a type of power spectral density which is inversely proportional to the spectral frequency $\omega/2\pi$. If Flicker PM noise is present then there is a logarithmic divergence of the standard deviation which increases with the number of samples taken (Ref. 4). So it is important to determine if this noise process is present.

Knowing the limiting noise process to be white PM, one can safely proceed using the statistics of the normal distribution. The results of this analysis have shown that one can measure time differences to less than one nanosecond for averaging times of 4 minutes (Ref. 5). The data from the two receivers are being analyzed by both NBS and JPL. Results have been published by NBS (Ref. 7). Figure 2 is a graph of UTC (USNO) – UTC (NBS) versus days. The graph covers about a four-month period. During this period several clock trips were made between USNO and NBS. The agreement is shown on the graph.[5]

The syntonization between the rates of UTC (USNO) and UTC (NBS) can be measured using the GPS timing receivers. If a set of time difference measurements are made using a single SV, then a slope can be found of time difference versus time, by finding a least square linear fit to the data. This assumes that the noise causing the variations in readings is white. This procedure is repeated for several SVs which produces a set of slopes (Fig. 3a,b,c,d). The slopes are a measure in the difference in rates of the two clocks as measured by using different SVs.

A second assumption is now made; that is, the measures of these slopes are independent. Next, the mean and standard deviation and the standard deviation of the mean are found for the set of slopes.

For the period 5 Sept 81 to 16 Sept 81[6] the slopes of [UTC (USNO)] – [UTC (NBS)] by the several SVs are:

by SV 5 −11.32 nanosec/day

by SV 9 −11.35 nanosec/day

by SV 6 −10.73 nanosec/day

by SV 8 −11.87 nanosec/day

The mean is	−11.07 nsec/day
The standard deviation is	−0.67 nsec/day
The standard deviation of the mean is	−0.33 nsec/day

[4]UTC universal coordinated time. The new UTC was adopted by the International Radio Consultive Committee (CCIR) in 1971 and put into effect 1 Jan. 1972. In this system all clocks run at the same rate, based on an atomic cesium clock.

[5]The measurement of the time offset via GPS has an offset of +445 nanosec with respect to the clock closure. The reason is unknown at this time; it is probably due to design differences in the USNO and NBS receivers. The offset was removed from the GPS data.

[6]These dates are arbitrarily taken. The period happens to be a set of continuous data. Other sets have produced better results.

The standard deviation of the mean is found by

$$\frac{SD}{\sqrt{N}} = \frac{0.67}{\sqrt{4}} = -0.33 \text{ nsec/day}$$

where SD is the standard deviation and N is the number of degrees of freedom. Since it was assumed that the measurements via the different SVs were independent, this number is 4, the number of SVs.

The value of 0.33 nanosecond per day corresponds to

$$\frac{0.33 \times 10^{-9} \text{ sec/day}}{86{,}400 \text{ sec/day}} = -3.82 \times 10^{-15} \frac{\Delta f}{f}$$

which is a measure of syntonization.

VI. The GPS Timing Receivers in the DSN

The GPS timing receivers will be deployed in the DSN in several steps. The first step will be to establish time and frequency transfer between NBS and the Time Standard Ensemble located at Goldstone. The final step will be to establish time and frequency transfer throughout the DSN.

The first step of the demonstration will be to install the two GPS receivers at the Goldstone clock ensemble at Goldstone. The receivers will be scheduled to perform mutual view observations with NBS and USNO.

This configuration and procedure will repeat the demonstration that is presently being performed between NBS and USNO. There will be a receiver at each of these two clock ensembles. The ensembles are located some distance from each other but not so great a distance that the mutual viewing angles are shallow. Finally there is a regular traveling clock trip between these clock ensembles. This demonstration will not only confirm the NBS-USNO experiment, but it will establish a time and frequency transfer between the DSN and NBS. The immediate results of this configuration and procedure will be to reduce the necessity of clock trips between the Goldstone clock ensemble and NBS from every 120 days to once a year or even less often. It is planned to permanently have one of the receivers at the Goldstone clock ensemble. Therefore this saving can be continually realized.

Another saving will be realized when the Goldstone clock ensemble is moved to DSS 14. This move is planned for sometime in 1983. The presence of a GPS receiver will greatly help maintain time and frequency during the move.

The reason for placing two GPS receivers at the same place is to check the receivers themselves and act as a control for the Goldstone-NBS experiment. The two receivers should give identical results if their antennas are in the same location. In addition this will give us a chance to check the receiver before it is sent to another station in the DSN.

I plan to repeat the procedures that are now being done between NBS and USNO. The difference is time and frequency transfer from NBS to the Goldstone clock ensemble rather than USNO. In addition time comparisons will be made between the two GPS receivers which are located next to one another at the Goldstone clock ensemble. These measurements should be identical except for any errors in the receivers themselves.

Beyond repeating the NBS to USNO demonstration and the establishment of time and frequency transfer from NBS to the Goldstone clock ensemble, an even more informative measurement will be available. If the NBS, USNO and the Goldstone clock ensemble GPS receivers are all on the same schedule, for mutual view, then a three-station measurement closure will be available. This will be somewhat akin to the three baseline VLBI closures reported in Ref. 8 except that all of the stations will be located in the continental U.S.

This will allow a simultaneous measurement of the time offset [UTC (USNO) – UTC (DSN)], [UTC (USNO) – UTC (NBS)] and [UTC (USNO) – UTC (DSN)]. There will be two checks of the accuracy of time transfer using the GPS receivers. First the offsets [UTC (USNO) – UTC (NBS)] and [UTC (NBS) – UTC (DSN)] are well-known and kept with traveling clocks.[7] Second, by the closure measurement it should be possible to get a measure of the absolute accuracy of the GPS receiver system independent of clock trips.

The second step will be to move one of the GPS timing receivers to DSS 63 in Spain. Spain was chosen as the second installation because it is closer to Goldstone GTS than DSS 43 in Australia. The great circle distance between GTS and Madrid is approximately 85° whereas the great circle distance between Goldstone and Canberra is approximately 110°.

It is also possible to complete a closure of measurements which includes DSS 63. USNO is approximately 55° great

[7] All times have been subtracted from UTC (USNO). This corresponds to using USNO as the Standard. This is done for convenience. JPL traditionally uses NBS as the Standard for the DSN because of its proximity.

circle distance from Madrid. There will be mutual view measurements (once per day, it is hoped) among the four locations USNO, NBS, Goldstone and DSS 63. This daily mutual view might involve some low viewing angles from DSS 63 because of nonconformance to USNO's schedule. Daily mutual or sequential view between Goldstone and DSS 63, which is independent of outside agencies, is being planned.

There are plans by NBS to install a receiver in Paris, France, at the Bureau International de l'Heure (BIH), sometime in 1982. Paris is only 10° great circle distance from Madrid; therefore one could expect the same performance as between USNO and NBS. This assumes a daily high angle observation from BIH.

The third step will be to install a receiver at DSS 43. This is the most difficult step because of the distance. The great circle distance from GTS to DSS 43 is approximately 110° and from DSS 43 to DSS 63 approximately 160°. Mutual views at these distances are right above the horizon; therefore a schedule of sequential views will probably be the more useful. Because JPL will have only two receivers we are planning to use one of NBS's receivers for the DSS 43 demonstration.

An exciting experiment will be a three-station closure of DSS 43, DSS 63 and GTS. The results of this will be compared to the VLBI three station closure in 1979 (Ref. 7). The DSN receivers will be scheduled to make a three-station closure every day if possible. Certainly we will make an offset measurement, [UTC (DSN) – UTC (DSS 43)] and [UTC (DSN) – UTC (DSS 63)], every day.

VII. Conclusion

It is no mean task to determine the accuracy of time transfer over intercontinental distances using the GPS receivers. Suppose a sequential view of a SV is taken by two receivers anyplace on the Earth. Furthermore, suppose the SV is equipped with a cesium clock. Then time transfer accuracies of 10 nsec to 50 nsec are anticipated (Ref. 8). This means for a three-station closure the expected error is $\sqrt{3}$ times the individual experiment error or, 17 – 86 nsec. By using multireceiver closures, and repeating the short distance (<4000 km), transfers which were demonstrated in the continental U.S., the accuracies can certainly be confirmed.

The obvious way to determine the accuracy of GPS receiver time transfer is to make an independent measurement using established methods. Data on the regular clock closures give errors of 300 nsec, which is too large to measure GPS receiver performance. A careful clock closure could yield an error of 35 nsec for a trip of <40 hours each way, with three such trips 2 months apart. Frequency could be measured with an error of $1 \times 10^{-14}\ \Delta f/f$.

The other method of time transfer used in the DSN is VLB1. Present VLB1 errors are approximately 100 nsec from DSS 14 to DSS 63, and 200 nsec from DSS 14 to DSS 43. The DSS 43 to DSS 63 baseline measurement is not done often but the accuracy of that baseline is approximately 300 nsec. Within the next few months, there are plans to implement new techniques that are expected to decrease the errors from one to two orders of magnitude (Refs. 9, 10). This would mean that VLB1 could be used as an independent measurement of the time offsets between the clocks in the DSN.

Acknowledgement

Appreciation is expressed for the technical assistance and data provided by Mr. David W. Allan and Mr. Dick D. Davis of the National Bureau of Standards.

References

1. Spilker, J. J., *Digital Communication by Satellite*, Thomas Kailath, editor, Prentice-Hall Inc., Chapter 17, 18.
2. "Time and Frequency Theory and Fundamentals," NBS Monograph 140, National Bureau of Standards, U.S. Department of Commerce, Byron E. Blair, editor, page 208.
3. Ashby, N., and Allan, D., "Practical Implication of Relativity for a Global Coordinate Time Scale," *Radio Science*, Vol. 14, pp. 649-669, July-August 1979.
4. Allan, D. W., "Statistics of Atomic Frequency Standards," *Proc. IEEE*, Feb. 1966, pp. 221-230.
5. Allan, D. W., and Barnes, J., "A Modified Allan Variance With Increased Oscillator Decharacterization Ability," 35th Proceedings of the Annual Symposium on Frequency Control, 1981.
6. Davis, D. D., et al., "Construction and Performance Characteristics of a Prototype NBS/GPS Receiver," Proceedings of the 35th Annual Symposium on Frequency Control, 1981.
7. Allan, D. W., and Weiss, M. A., "Accuracy Time and Frequency Transfer During Common View of a GPS Satellite," Proceedings of the 34th Annual Frequency Control Symposium, 1980.
8. Cheetham, C. M., et al., "Demonstration of Remote Clock Monitoring by VLBI, With Three Baseline Closures," in *DSN Progress Report 42-53, July-August 1979*, Jet Propulsion Laboratory, Pasadena, Calif., Oct. 15, 1979.
9. Wilcher, J. H., "Block I Phase 1 Very Long Baseline Interferometry Implementation," in *The Deep Space Network Progress Report 42-58*, Jet Propulsion Laboratory, Pasadena, Calif., Aug. 15, 1980.
10. Wilcher, J. H., "Block 1 Phase 2 Very Long Baseline Interferometry Implementation," in *The Tracking and Data Acquisition Progress Report 42-66*, Jet Propulsion Laboratory, Pasadena, Calif., Dec. 15, 1981.

GLOBAL POSITIONING SYSTEM (GPS)

VALUES PRESENTED BELOW FOR NAVSTAR GPS SATELLITES ARE THE RESULT OF A LINEAR FIT THROUGH APPROXIMATELY 100 DATA POINTS, REFERRED TO THE BEGINNING OF THE TRACKING PERIOD (TIME OF MEASUREMENT). SATELLITES ARE TRACKED FOR APPROXIMATELY TEN MINUTES.

		NAVSTAR 1 SV# 4	NAVSTAR 3 SV# 6	NAVSTAR 4 SV# 8	NAVSTAR 5 SV# 5	NAVSTAR 6 SV# 9
	MJD	MC-GPS UT	MC-GPS UT	MC-GPS UT	MC-GPS UT	MC-GPS UT
NOV. 9	44917*	-	-	-	-	-
10	44918	-49.805(180448)	-49.877(175330)	-49.879(174224)	-49.866(191530)	-49.867(190530)
11	44919	-49.697(180430)	-49.805(175330)	-49.811(174230)	-49.798(191548)	-49.792(190430)
12	44920	-49.705(180442)	-49.743(175354)	-49.755(174230)	-49.737(191548)	-49.732(190430)
13	44921	-49.621(180448)	-49.677(175330)	-49.688(174230)	-49.673(191554)	-49.676(190448)
14	44922	-49.538(180430)	-49.592(175330)	-49.607(174230)	-49.599(191530)	-49.595(190430)
15	44923	-49.419(180424)	-49.544(175400)	-49.545(174218)	-49.534(191548)	-49.546(190424)
16	44924	-49.434(180454)	-49.475(175348)	-49.480(174218)	-49.472(184830)	-49.458(183818)
17	44925	-49.306(173730)	-49.404(172630)	-49.412(171518)	-49.381(184830)	-49.398(183730)
18	44926	-49.253(173730)	-49.352(172654)	-49.353(171530)	-49.775(184830)	-49.012(183730)

*NO DATA DUE TO RECEIVER MALFUNCTION

Fig. 1. Time differences between USNO master clock minus GPS time (from a U.S. Naval Observatory publication)

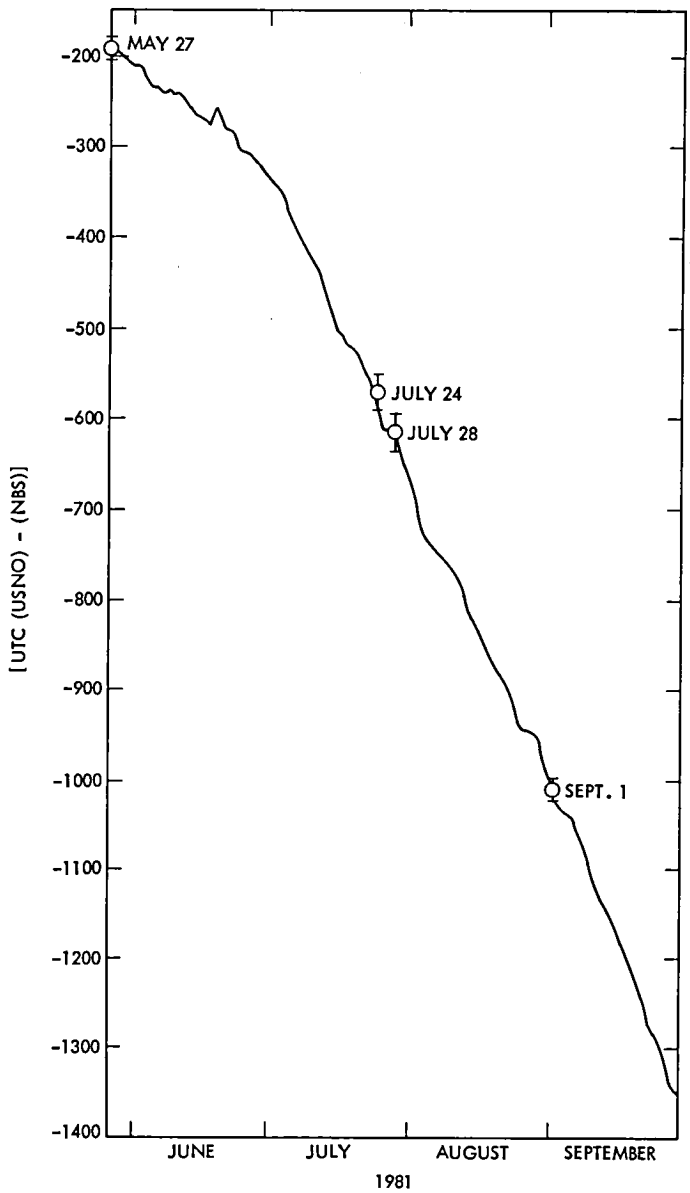

Fig. 2. UTC (USNO) minus UTC (NBS) vs time

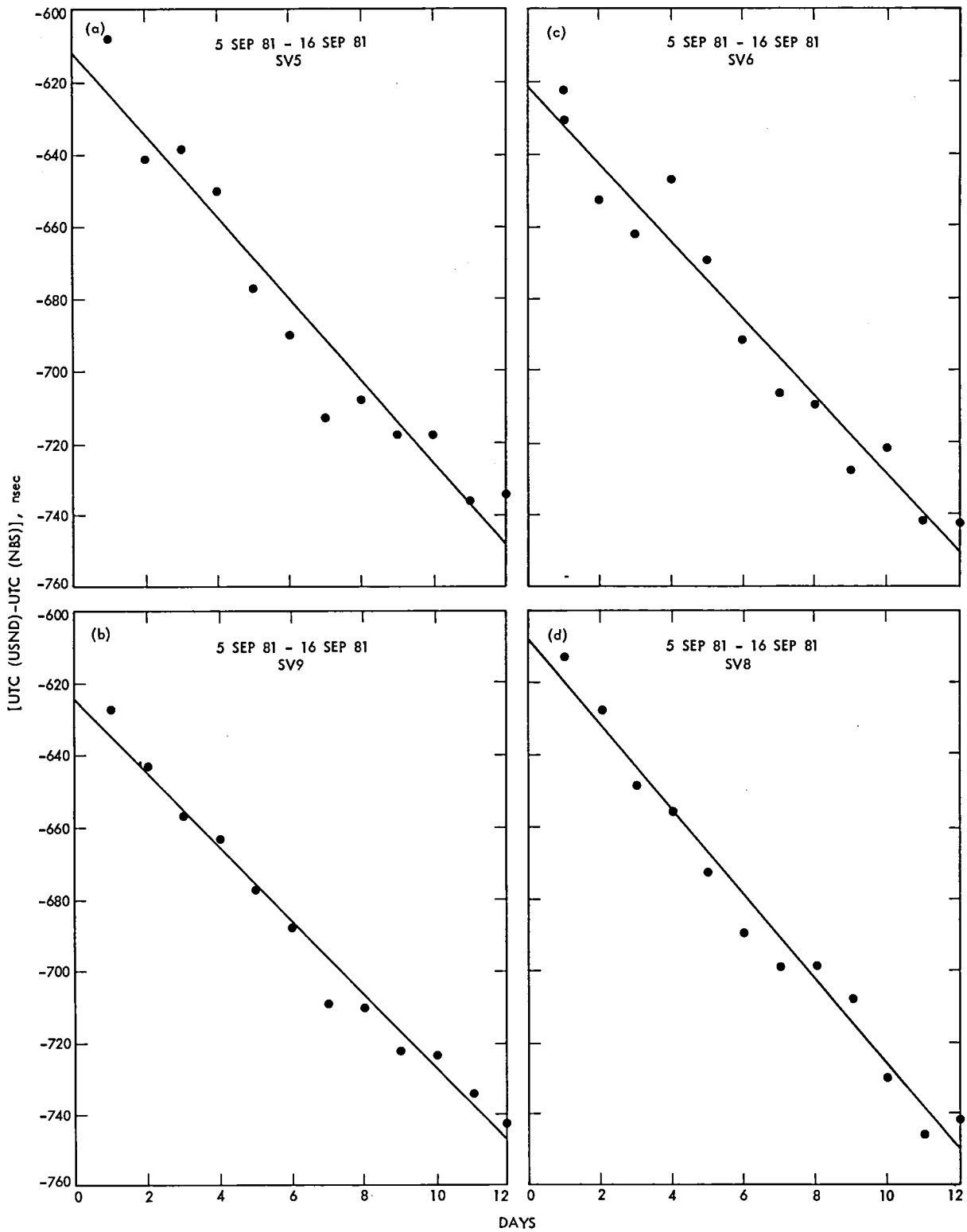

Fig. 3. UTC (USNO) minus UTC (NBS) vs time for four SVs

Noise Temperature and Noise Figure Concepts: DC to Light

C. T. Stelzried
TDA Mission Support Office

Deep Space communication systems require extremely sensitive receiving systems. The NASA Deep Space Network is investigating the use of higher operational frequencies for improved performance. Noise temperature and noise figure concepts are used to describe the noise performance of these receiving systems. It is proposed to modify present noise temperature definitions for linear amplifiers so they will be valid over the range $(hf/kT) \ll 1 \ll (hf/kT)$. *This is important for systems operating at high frequencies and low noise temperatures, or systems requiring very accurate calibrations. The suggested definitions are such that for an "ideal" amplifier,* $T_e = (hf/k) = T_q$ *and* $F = 1$. *These definitions revert to the present definition for* $(hf/kT) \ll 1$. *Noise temperature calibrations are illustrated with a detailed example. These concepts are applied to system signal-to-noise analysis. The fundamental limit to a receiving system sensitivity is determined by the thermal noise of the source and the quantum noise limit of the receiver. The sensitivity of a receiving system consisting of an "ideal" linear amplifier with a 2.7 K source, (−194.3 dBm/Hz assuming* $(hf/kT) \ll 1$*) degrades significantly at higher frequencies.*

I. Introduction

Deep space communication systems require extremely sensitive receiving systems (Ref. 1). The Deep Space Network is investigating the use of higher operational frequencies for improved performance. Noise temperature and noise figure concepts are used to describe the noise performance of these receiving systems (Refs. 2, 3, 4). These concepts are reviewed for application to higher frequencies by removal of the low-frequency restriction, $(hf/kT) \ll 1$.

II. Theory

The available thermal (Refs. 5, 6, 7) noise power from a source at the amplifier output ($G \gg 1$) is given by

$$P_n = kTBG\left(\frac{hf/kT}{e^{hf/kT}-1}\right) \tag{1}$$

where

T = source temperature, K

h = Planck's constant = 6.6256×10^{-34} J-S

k = Boltzman's constant = 1.3805×10^{-23} J/K

f = operating frequency, Hz

$B = \frac{1}{G} \int_0^\infty G(f)df$ = noise bandwidth, Hz

$G(f)$ = available power gain, ratio

G = maximum available power gain, ratio

The amplifier output is approximately (disregarding the contribution of the amplifier: $hf << kT$)[1]

$$P_n = kTBG \tag{2}$$

Eqs. (1) and (2) are shown plotted in Fig. 1 for a large range of hf/kT values. Most microwave applications with $(hf/kT) << 1$ are restricted to the region near the origin.

It is computationally convenient to define a temperature T' such that

$$P_n = kT'BG = kTBG \left(\frac{hf/kT}{e^{hf/kT} - 1} \right)$$

T' can be conveniently found by subtracting a correction T_c (Ref. 8) from T

$$(P_n/kBG) = T' = T - T_c \tag{3}$$

where

$$T_c = T \left(1 - \frac{hf/kT}{e^{hf/kT} - 1} \right)$$

or conveniently

$$T_c \cong 0.024f\,(\text{GHz}) - 0.000192\,[f(\text{GHz})]^2/T + \cdots \tag{4}$$

[1]Note that $(hf/kT) \approx 0.048\,f\,(\text{GHz})/T(k) \approx 0.00048$ at 1 GHz and 100 K and ≈ 1 at 208 GHz and 10 K indicates that Eq. (2) is an extremely good approximation for most microwave applications.

These correction terms are shown plotted in Fig. 2. For example, at 32 GHz, the cosmic background temperature (Refs. 9, 10) of $\cong 2.7$ K, correctly defined for use with Eq. (1) is "corrected" to $\cong 2.0$ K for use with Eq. (2).

The quantum noise limit (Ref. 7, 11) of a linear amplifier (where both phase and amplitude information is retained), a manifestation of the quantum mechanics uncertainty principle, is given by[2]

$$P_n = hfBG \tag{5}$$

Fundamental limits of an ideal receiving system sensitivity are determined by the sum of the source thermal noise and the quantum noise limit of an ideal amplifier (since these noise sources are uncorrelated (Ref. 7)).

$$P_n = kTBG \left(\frac{hf/kT}{e^{hf/kT} - 1} \right) + hfBG = k(T' + T_q)\,BG \tag{6}$$

or

$$(P_n/kBG) = T' + T_q$$

This is plotted if Figs. 1, 3 and 4 as functions of (hf/kT), f and T. In Fig. 4, the value of P_n/kBG for $(hf/kT >> 1)$ is given by hf/k (or T_q) and for $(hf/kT << 1)$, by $T + hf/2k$ (or $T + T_q/2$). It is easily shown (Fig. 1) that the quantum noise limit and thermal noise are equal when $(hf/kT) = \ln 2 \cong 0.69$.

III. Noise Temperature and Noise Figure: $(hf/kT) << 1$

A receiving system noise performance is characterized by the operating noise temperature (Refs. 2, 3, 4, 13) defined by (linear amplifier, single channel, matched source, $G >> 1$)

$$T_{op} = N_{T_o}/kBG \tag{7}$$

[2]Eq. (5) is appropriate only for linear amplification. At optical frequencies, using discrete photons, techniques may exist (Ref. 7) to circumvent this limitation. Equating kTB to quantum noise hfB results in an equivalent quantum noise temperature, $T_q = (hf/k)$. Although T_q is a fictitious temperature, it is useful for computational analysis and can be used with Eq. 2 to compute P_n.

where

N_{T_o} = receiver system total output noise power, within the frequency band B, excluding output load noise, W

Also

$$T_{op} = T_i + T_e \tag{8}$$

where

T_i = input source noise temperature, K

T_e = effective input noise temperature of the receiver, K

The definition (Refs. 2, 3, 4) of an amplifier noise figure is

$$F = N_{T_o}(T_i = T_o)/kT_oBG \tag{9}$$

where

$N_{T_o}(T_i = T_o)$ = receiver total output noise power with input termination at temperature T_o, W

T_o = 290 K

From Eqs. (7), (8) and (9)

$$F = 1 + (T_e/T_o) \tag{10}$$

or

$$T_e = (F - 1)\,T_o$$

For an "ideal" amplifier, $T_e = 0$, $F = 1$, and

$$T_{op} = T_i$$

IV. Noise Temperature and Noise Figure: $0 \leq (hf/kT) \leq \infty$

As before,

$$T_{op} = N_{T_o}/kBG \tag{11}$$

Substituting T_i' for T_i in Eq. (8)[3]

$$T_{op} = T_i' + T_e \tag{12}$$

where

$$T_i' = T_i\left(\frac{hf/kT_i}{e^{hf/kT_i} - 1}\right)$$

Following the spirit ($F = 1$ for an "ideal" amplifier) of Eq. (9), define

$$F = N_{T_o}(T_i = T_o')/k\,(T_o' + T_q)\,BG \tag{13}$$

where

$N_{T_o}(T_i = T_o')$ = receiver total output noise power with input termination at temperature T_o', W

$$T_o' = T_o\left(\frac{hf/kT_o}{e^{hf/kT_o} - 1}\right)$$

T_o = 290 K

From Eqs. (11), (12) and (13)

$$F = (1 + T_e/T_o')/(1 + T_q/T_o') \tag{14}$$

or

$$T_e = (F - 1)\,T_o' + FT_q$$

For an "ideal" amplifier $T_e = T_q$, $F = 1$, and

$$T_{op} = T_i' + T_q$$

These equations all revert to present definitions, Section III, when $(hf/kT) \ll 1$; i.e., $T_q = 0$, $T_i' = T_i$, $T_o' = T_o$.

[3] T_e is obtained by analysis or measurement as shown in Appendix A. For an ideal amplifier, $T_e = hf/k = T_q$.

V. Noise Temperature and Noise Figure: $(hf/kT) >> 1$

As before,

$$T_{op} = N_{T_o}/kBG \tag{15}$$

At these very high frequencies, thermal noise is negligible compared to T_q, so that $T_i' = T_o' \to 0$, and from Eq. (12)

$$T_{op} = T_e \tag{16}$$

and from Eq. (13),

$$\begin{aligned} F &= N_{T_o}/kT_qBG \\ &= N_{T_o}/hfBG \end{aligned} \tag{17}$$

From Eqs. (15), (16), and (17), or directly from Eq. (14),

$$F = T_e/T_q \tag{18}$$

or

$$T_e = FT_q$$

For an "ideal" amplifier, $F = 1$, $T_e = T_q$, and

$$T_{op} = T_q$$

VI. System Performance

The output signal-to-noise power ratio for a receiving system is given by $((hf/kT) << 1)$,

$$\begin{aligned} (S_o/N_o) &= \left(S_iG/N_{T_o}\right) \\ &= S_i/kT_{op}B \\ &= S_i/k\,(T_i + T_e)\,B \\ &= S_i/k\,(T_i + (F-1)\,T_o)\,B \end{aligned} \tag{19}$$

where

S_i = input signal power, W

For $(0 \leqslant (hf/kT) \leqslant \infty)$,

$$\begin{aligned} (S_o/N_o) &= S_i/kT_{op}B \\ &= S_i/k\,(T_i' + T_e)\,B \\ &= S_i/k\,(T_i' + (F-1)\,T_o' + FT_q)\,B \end{aligned} \tag{20}$$

and for $(hf/kT) >> 1$,

$$\begin{aligned} (S_o/N_o) &= S_i/(kT_{op}B) \\ &= S_i/kT_eB \\ &= S_i/FkT_qB \\ &= S_i/FhfB \end{aligned} \tag{21}$$

The performance of a receiving system composed of an "ideal" amplifier ($T_e = T_q$) and a source at the cosmic background temperature ($T_i = 2.7$ K), is shown in Table 1 and Fig. 5. S_i is the input signal power required for $(S_o/N_o) = 1$. Table 1 and Fig. 5 demonstrate the loss in sensitivity at very high frequencies relative to low frequencies for a conventional receiving system with an "ideal" linear receiver.

VII. Conclusion

The equations developed in the previous sections are tabulated in Table 2. The use of noise temperature and noise figure concepts require special consideration when $(hf/kT) \neq << 1$. This is usually important for systems operating at high frequencies with low noise temperatures, or systems requiring precise calibrations.

Fundamental limits to a receiving system are determined by the thermal noise of the source and the quantum noise limit of the amplifier. The sensitivity of a receiving system consisting of an "ideal" linear amplifier with a 2.7 K source (-194.3 dBm/Hz assuming $(hf/kT) << 1$) degrades significantly at higher frequencies. Of course, there are tremendous advantages

at higher frequencies, such as greater potential bandwidth, less spectrum crowding, link security, smaller antennas, photon counting schemes, etc.

A frequent end goal of using the more complicated equations of Section IV is to obtain the most accurate value of T_{op} for use with system performance evaluation such as in Section VI. T_{op} consists of the sum of T_i' and T_e. The decrease of T_i' and increase of T_e with frequency tends to cancel, minimizing the error in T_{op}. Therefore, the techniques of Section III can be used to very good accuracy to extremely high frequencies (see Table A-1 and Fig. A-2) for calculation of T_{op}.

However, for precise calibrations, the proposed equations of Section IV should be used.

Acknowledgment

Helpful discussions were held with R. C. Clauss, E. C. Posner, P. N. Swanson, T. Sato, J. A. McNeil, J. M. Stacey and M. S. Shumate.

References

1. Reid, M. S., et al., "Low Noise Microwave Receiving System in a Worldwide Network of Large Antennas," *Proc IEEE*, Vol. 61, No. 9, p. 1330, Sept. 1973.
2. Haus, H. A., et al., "IRE Standards on Electron Tubes: Definition of Terms," 1962 (62 IRE 7.52), *Proc IEEE*, Vol. 51, 1963.
3. Adler, R., et al., "Description of the Noise Performance of Amplifiers and Receiving Systems," *Proc IEEE*, Vol. 51, 436, 1963.
4. Mumford, W. W., and Scheibe, E. H., "*Noise Performance Factors in Communication Systems*," Horizon House Microwave Inc., 1968.
5. Johnson, J. B., *Phy Rev.*, Vol. 32, 97, 1928.
6. Nyquist, H., *Phy. Rev.*, Vol. 32, 110, 1928.
7. Pierce, J. R., and Posner, E. C., *Introduction to Communication Science and Systems*, Plenum Press, New York, 1980.
8. Viggh, E. V., "How Noisy is that Load," *Microwaves*, p. 54, Jan. 1976.
9. Penzias, A. A., and Wilson, R. W., "A Measurement of Excess Antenna Temperature at 4080 Mc/s," *Astrophys. J.*, Vol. 142, pp. 419-421, July 1965.
10. Otoshi, T. Y., and Stelzried, C. T. "Cosmic Background Noise Temperature Measurement at 13-cm Wavelength," *IEEE Instr. and Meas.*, Vol. 24, No. 2, June 1975.
11. Oliver, B. M., "Thermal and Quantum Noise," *Proc IEEE*, p. 436, May 1965.
12. Stelzried, C. T., "Operating Noise Temperature Calibrations of Low Noise Receiving Systems," *Microwave Journal*, Vol. 14, No. 6, p. 44, June 1961.
13. Siegman, A. E., "Thermal Noise in Microwave Systems, Part III, Practical Problems and Ultimate Limits on Amplifier Noise Figure," *Microwave Journal*, May 1961, p. 93.
14. Stelzried, C. T., "Microwave Thermal Noise Standards," *IEEE MTT-16*, No. 9, Sept. 1968.

Table 1. Tabulation of the sensitivity of an "ideal" receiver ($T_e = T_q$) with an input source temperature of 2.7 K as a function of frequency

Parameter	Equations (8), (19)	Equations (12), (20)				Equations (16), (21)
	Frequency, GHz					
	0.0	32	200	400	2000	20,000 (λ = 15 μm)
T_i', K	2.7	2.0	0.3	0.0	0.0	0.0
$T_e = T_q$, K	0.0	1.5	9.6	19.2	96.0	960.0
T_{op}, K	2.7	3.5	9.9	19.2	96.0	960.0
S_i, dBm/Hz	−194.3	−193.1	−189.0	−185.8	−178.8	−168.8

Table 2. Summary of noise temperature and noise figure concepts: dc to light (Linear amplifier, single channel, matched source, $G >> 1$)

Parameter	$(hf/kT) = Tq/T$		
	$0 \leq (hf/kT) \leq \infty$	$(hf/kT) << 1$	$(hf/kT) >> 1$
$T_{op} = N_{T_o}/kBG$	$= T_i' + T_e$	$= T_i + T_e$	$= T_e$
	$= *[T_i' + T_q]$	$= *[T_i]$	$= T_q$
F	$= N_{T_o}(T_i = T_o')/k(T_o' + T_q)BG$	$= N_{T_o}(T_i = T_o)/kT_oBG$	$= N_{T_o}/hfBG = N_{T_o}/kT_qBG$
	$= (1 + T_e/T_o')/(1 + T_q/T_o')$	$= 1 + (T_e/T_o)$	$= 1 + (T_e/T_q)$
	$= *[1]$	$= *[1]$	$= *[1]$
(S_o/N_o)	$= S_i/k(T_i' + T_e)B$	$= S_i/k(T_i + T_e)B$	$= S_i/kT_eB$
	$= S_i/k(T_i' + (F-1)T_o' + FT_q)B$	$= S_i/k(T_i + (F-1)T_o)B$	$= S_i/FhfB = S_i/FkT_qB$
	$= *[S_i/k(T_i' + T_q)B]$	$= *[S_i/kT_iB]$	$= *[S_i/hfB = S_i/kT_qB]$

*[ ] "Ideal" amplifier (i.e., $T_e = T_q, F = 1$)

S_i = Input signal power, W

N_{T_o} = Total output noise power within bandwidth B, W

$$T_i' = T_i \left(\frac{T_q/T_i}{e^{T_q/T_i} - 1} \right)$$

$$T_o' = T_o \left(\frac{T_q/T_o}{e^{T_q/T_o} - 1} \right)$$

T_o = 290 K

$T_q = (hf/k) \cong 0.048f$ (GHz)

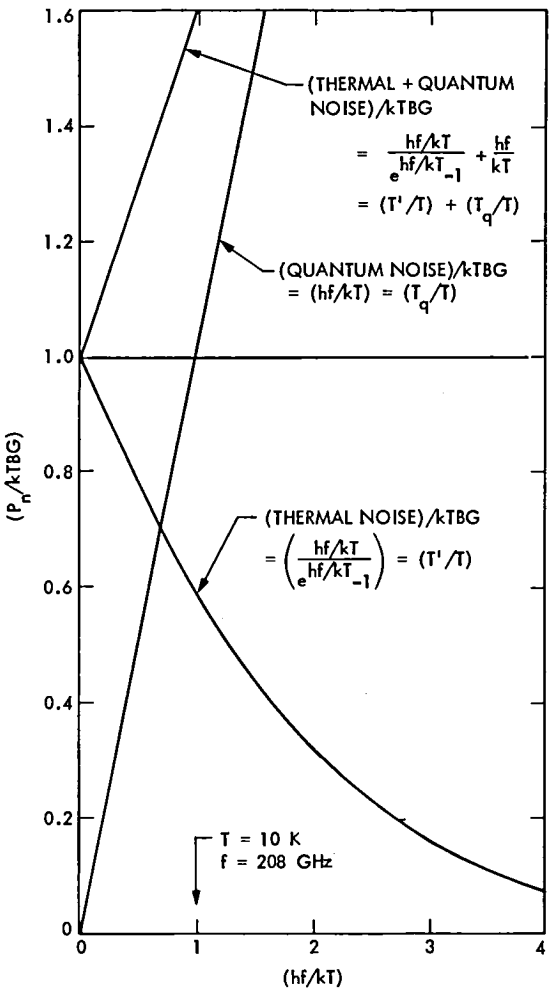

Fig. 1. (P_n /$kTBG$) vs (hf/kT), showing the thermal and quantum noise contributions

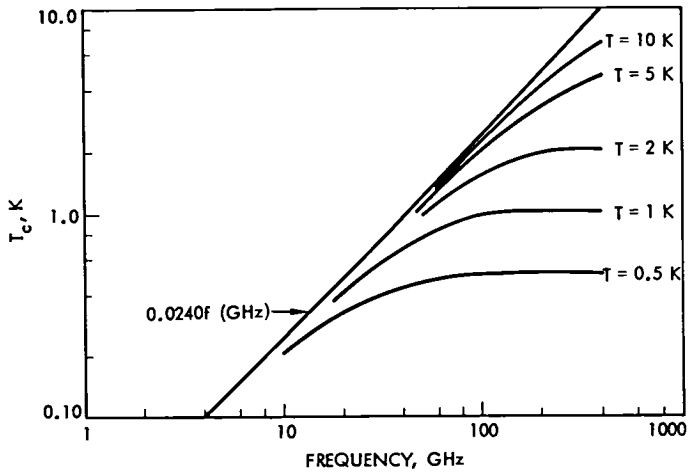

Fig. 2. Thermal noise temperature correction T_C as a function of frequency and temperature

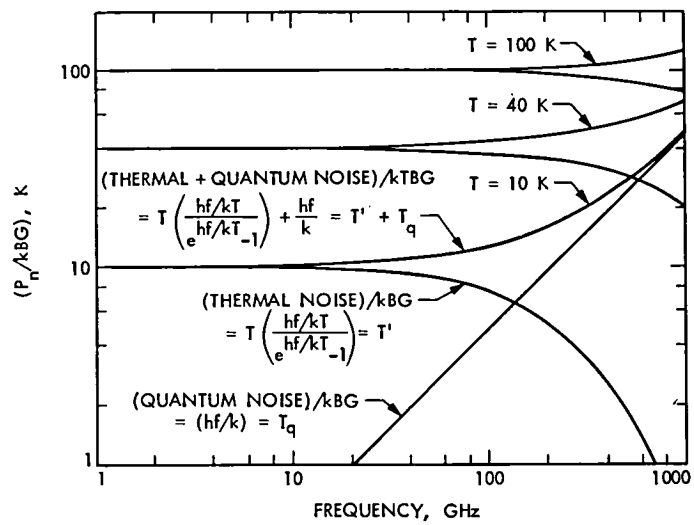

Fig. 3. (P_n/$kTBG$) vs frequency for various temperatures, showing thermal and quantum noise contributions

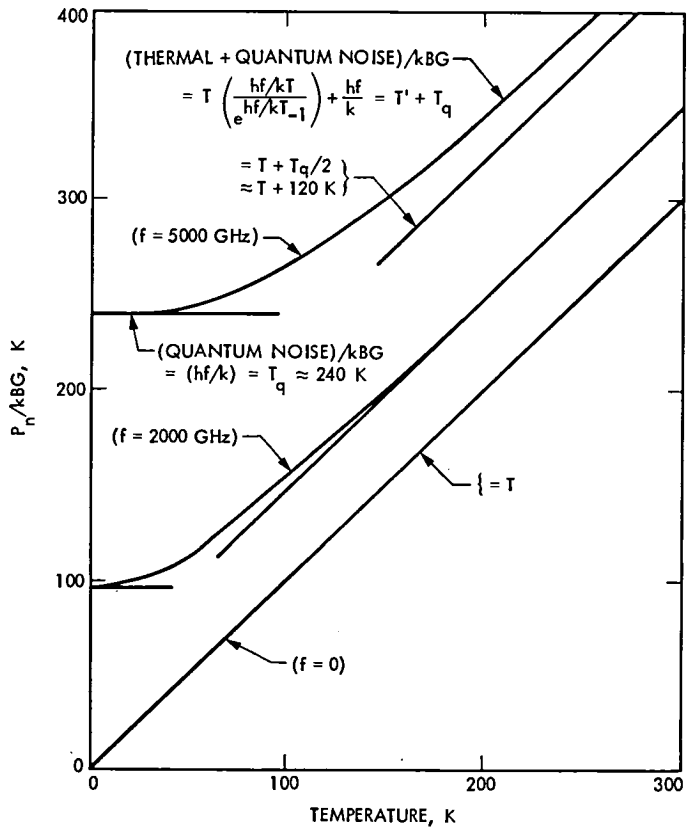

Fig. 4. (P_n/kBG) vs temperature for various frequencies

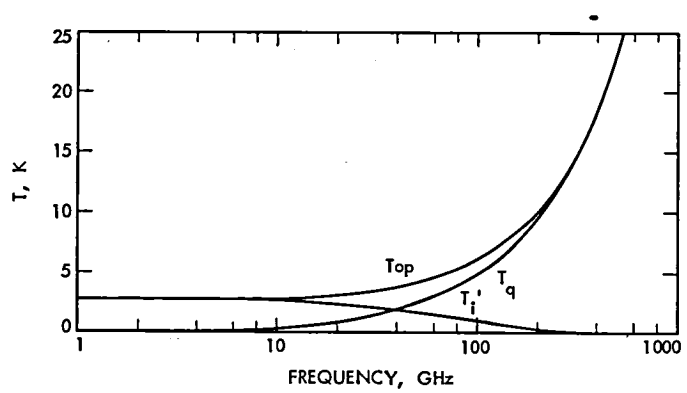

Fig. 5. T'_i, T_q and T_{op} vs frequency using an "ideal" receiver ($T_e = T_q$) with an input source temperature of 2.7 K.

Appendix A

Amplifier Noise Temperature Calibration

Consider the Y factor equations for the amplifier in the test configuration shown in Fig. A-1 using two matched calibration terminations at physical temperatures T_2 and T_1.

Case 1: $(hf/kT) \ll 1$

$$Y = \frac{T_2 + T_e}{T_1 + T_e} \tag{A-1}$$

Solving

$$T_e = \frac{T_2 - YT_1}{Y - 1} \tag{A-2}$$

Case 2: $0 \leqslant (hf/kT) \leqslant \infty$

$$Y = \frac{T_2' + T_e}{T_2' + T_e} \tag{A-3}$$

Solving

$$T_e = \frac{T_2' + YT_1'}{Y - 1} \tag{A-4}$$

where

$$T_2' = T_2 \left(\frac{hf/kT_2}{e^{hf/kT_2} - 1} \right)$$

$$T_1' = T_1 \left(\frac{hf/kT_1}{e^{hf/kT_1} - 1} \right)$$

Consider the following parameters applicable to Fig. A-1.

$T_1 = 100\,\text{K}$ $\quad T_i = 10\,\text{K}$

$T_2 = 400\,\text{K}$ $\quad Y = 3.7$

These values are used with Eqs. (A-2) and (A-4) for a wide range of frequencies. The results are tabulated in Table A-1 and plotted in Fig. A-2. T_i' and T_q can be estimated from Fig. 3. For these parameters, T_i decreases with frequency, while T_e increases. Since T_{op} is the sum of T_i' and T_e, there is a compensatory effect; however, there is a resultant net increase in T_{op} with frequency. For these parameters, the amplifier is nearly "ideal" at 400 GHz.

Table A-1. Tabulation of receiver and system parameters, using test parameters: T_1 = 100 K, T_2 = 400 K, T_i = 10K and Y = 3.7

	Equations (A-1), (8)	Equations (A-2), (12)		
		Frequency GHz		
Parameter, K	0.00	32	200	400
T'_1	100	99.23	95.28	90.71
T'_2	400	399.23	395.22	390.48
T'_i	10	9.25	5.96	3.30
$T_q = (hf/k)$	0.0	1.54	9.60	19.20
T_e	11.11	11.88	15.81	20.32
T_{op}	21.11	21.13	21.77	23.62

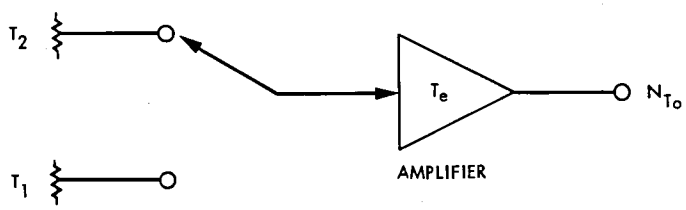

Fig. A-1. Block diagram of amplifier test configuration

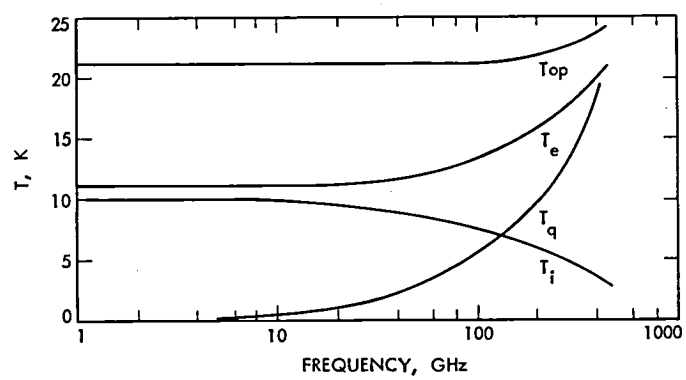

Fig. A-2. T'_i, T_e, T_q and T_{op} vs frequency assuming T_I = 10K and Y = 3.7

TIGER Reliability Analysis in the DSN

J. M. Gunn
Deep Space Network Support Section

TIGER is a computer program designed to simulate a system over a period of time to evaluate system reliability and availability. Results can be used in the Deep Space Network for initial spares provisioning and system evaluation. This article describes the TIGER algorithm, the inputs to the program and the output.

I. Introduction

Efficient spares provisioning is a continuing problem in the Deep Space Network (DSN). Correct determination of equipment to be spared, spares stock and optimal network allocation becomes increasingly critical as budgetary restrictions reduce the margin of error. The Deep Space Network Support Section (377) has modified a computer program developed by the Department of the Navy to evaluate system reliability and availability which can aid in this process. Known as TIGER, this program's applications in the DSN include initial spares provisioning, system reliability and availability evaluation and maintenance planning. A major asset is the program's ability to model a wide range of systems. Systems as complex as an entire tracking station to the simplest station subsystem can be accommodated. Models can be simulated on the network, complex, station, system and subsystem level.

Presently the DSN relies on the engineering judgment of the Cognizant Design Engineer and Cognizant Operations Engineer, aided with results from the DSN Efficient Sparing Program, to provision spares for the Deep Space Stations in its tracking network. By taking into account factors such as failure rates, repair rates and shipping time, TIGER can provide the engineers with an analytic tool that takes into consideration all major system parameters.

II. Simulation Theory

TIGER uses Monte Carlo simulation methods to model the system. This procedure assumes a constant failure rate over a period of time for the system equipment. The probability of a failure occurring before time t can therefore be determined by the exponential distribution function $F(t) = 1 - e^{-Lt}$, where L is the failure rate and t is the time to failure (TTF). Substituting the reciprocal of the mean time between failure (MTBF) for L and solving for t, the equation used in the TIGER algorithm is derived: $TTF = -(1/MTBF) \ln [1 - F(t)]$. To obtain an equipment TTF a random number between zero and one is generated and substituted into the equation for $[1 - F(t)]$ (Fig. 1).

Similarly, equipment time to repair (TTR) is simulated by drawing from an exponential distribution with the mean equal to the mean time to repair (MTTR). Here the random number is substituted into the equation $TTR = -(1/MTTR) \ln [1 - F(t)]$ to generate the time of equipment repair.

The system is simulated over a meaningful period of operating time, referred to as a mission. System up and down times are determined by generating a TTF for each lowest replaceable element (LRE) in the system. Initially each LRE is in an upstate. To detect system failure before completion of the

operational period simulated, the system is tested as each LRE fails. With each failure a TTR is generated for the LRE and a spare, if available, is put in its place. A new TTF is generated for each LRE experiencing repair to allow further failure after repair. This procedure continues until the mission aborts or the specified mission period is exceeded. The mission is aborted if the specified allowable downtime is exceeded due to lack of a critical equipment or subsystem. A new set of randomly generated values is used to determine equipment TTF and the program is rerun. At the end of each set of 50 mission simulations, reliability and availability figures are computed. Running a large number of missions (typically 500-1000) and averaging the results gives a high degree of accuracy.

TIGER is designed to simulate systems with variations in configuration. The operational sequence simulated is comprised of one or more operational phases. Each phase represents a unique configuration for the system. A maximum of 95 phases of 6 phase types are allowed. The configuration is based on a reliability diagram of the system. The system is divided into as many levels of subsystems as appropriate with the lowest level being that for which the MTBFs and MTTRs are supplied. From a maintenance standpoint this is the LRE.

III. Program Features

Much flexibility is provided by the program. Standby equipment may be designated to come up in the event of equipment failure. Operating rules may also be specified to cause a designated string of equipment to go down if one of the string equipment fails and no spares are available. These rules may vary by phase or remain constant throughout the mission.

Duty cycle, or percent of time used, may also be specified for each LRE by phase. This option is useful in systems where some equipment is used less rigorously than other system equipment. In the DSN this might apply to subsystems that are used less heavily during nontracking periods. Variable MTTRs may also be specified to provide for situations in which an equipment cannot be repaired during a particular mode of operation.

A sophisticated logisitics system is incorporated into TIGER. Numbers and types of spares may be specified as well as at what level the spares will be stocked. Three levels of sparing and associated administrative delay times are provided for. In the DSN this generally corresponds to the station, complex and network levels.

System and subsystem maximum allowable downtimes are user-specified to define mission abort conditions. Both sustained and total downtimes are considered.

User inputs to TIGER are equipment MTBF, MTTR and system configuration. Steps to using the program are as follows:

Define operational period to be simulated and allowable downtime.

Determine subsystem reliability configuration, noting parallel and series equipment.

Determine LREs.

Break system down into subsystems as warranted.

Gather MTBF and MTTR data for LREs

Determine sparing locations and associated logistics delay times.

Determine program options desired

Code input data in TIGER acceptable form.

Run program.

IV. Program Report

In the final report estimators for total system reliability, instantaneous availability, average availability and system readiness are given. In addition, mean uptime, mean downtime and mean time between mission failures are tabulated.

TIGER uses the generally accepted definition of reliability: the probability that the system will perform its intended function for a specified interval under the stated conditions. Mathematically this is calculated by dividing the number of mission aborts by the total number of simulated missions.

Two availability estimators are calculated. The average availability is the probability the system will be in satisfactory operating condition at a random point in time. In the DSN this is functional availability, or the fraction of scheduled service time the system performs its intended function. This is calculated mathematically as:

$$\text{Average Availability} = \frac{\text{uptime}}{\text{calendar time}}$$

The instantaneous availability is the same probability for a specific point in time (i.e., the beginning and the end of the phase.)

System readiness is the probability the system will be in satisfactory operating condition when there is neither a mission abort nor a system failure. The readiness estimator is generally considered the lower bound on the availability estimator.

Most useful from a maintenance standpoint are the individual equipment unreliability and unavailability calculations. This part of the report ranks the equipment in order of contribution to system unreliability and unavailability. This isolates the major contributors to system downtime and calculates the individual equipment percent contribution to unreliability.

Spares usage is reported by LRE. Average spares used per mission and the maximum amount of spares used in a single mission are given. For initial spares provisioning, an unlimited spares stock may be specified. In this case the results would reflect the optimal spares stock for 100% system reliability if it is obtainable with the specified system components.

A more detailed report, if desired, gives a complete listing of system equipment events. Up and down times of all critical LRE are listed in chronological order.

V. Example

To demonstrate the usefulness of the TIGER analysis the program results for the command modulator assembly (CMA) are included. The system has 34 LREs of 13 types. The system consists of two CMAs, one of which must be operational to prevent system downtime (Fig. 2). CMA 801 will come up only upon the failure of CMA 800.

The first part of the report (Fig. 3a,b) lists pertinent system parameters. Two simulation report options are available. The management summary prints a message each time a mission abort occurs (Fig. 4). The phase type, phase sequence, mission number and time of mission abort are listed. The engineering summary is a more complete report that indicates each time an equipment changes status (up to down or down to up) or a phase boundary is crossed (Fig. 5).

After each set of 50 system simulations a "figures of merit summary" is printed. Reliability and availability figures are calculated for each phase of the mission and for the entire mission timeline. The system report (Fig. 6) is for 250 missions.

The equipment failures and corrective maintenance summary (Fig. 7) tabulates for each LRE the number of failures for all missions. The average number of failures per mission and the average number of corrective maintenance hours expended are listed.

The spares report lists the average number of spares used in any single mission. The report for the CMA (Fig. 8) indicates that the spares stock could be more optimally allocated since the entire stock is not used.

The critical equipment list ranks each LRE in order of greatest contribution to system unavailability and unreliability (Figs. 9 and 10). The results for the CMA indicate the subcarrier synthesizer (SC SYN) is a major contributor to both system unavailability and unreliability. Attention should be given to improving the design of the SC SYN to increase the MTBF and to procuring SC SYN spares.

VI. Conclusions

Used in combination with the DSN Efficient Sparing Program, TIGER can potentially aid the cognizant engineers in both initial and ongoing spares provisioning and improve operational availability of system equipment.

The simulation techniques used in TIGER are in wide use today for system reliability and availability evaluation. A second version of TIGER called TIGER/MANNING will soon be completed. This version will include the simulation process of the original program augmented with calculations of optimal worker allocation in system maintenance and repair duties.

The only significant disadvantage, common to all simulations of this type, is the considerable amount of computer time and storage required when a large complex system is modeled. However, most foreseeable applications of this program within the DSN are not on such a scale. Another minor problem is the inevitable random errors found in all system simulations. In actual use the major problem has been a lack of reliable failure data for system equipment. The results, of course, are limited by the accuracy of the parameters supplied.

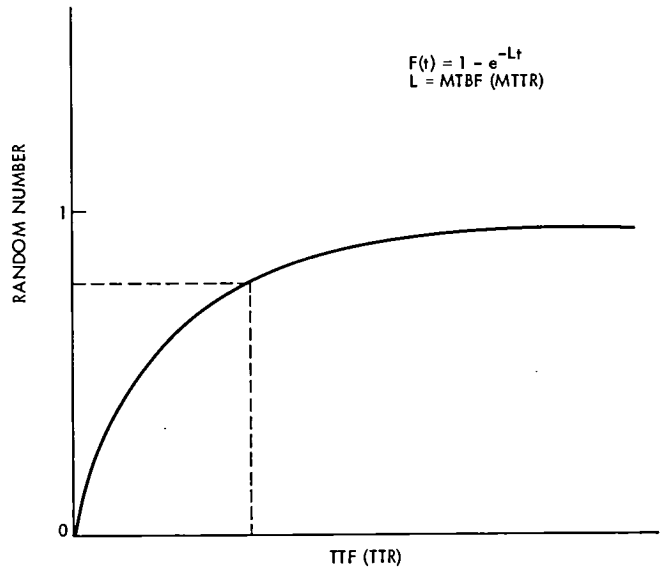

Fig. 1. Generation of time to failure (time to repair) from distribution function

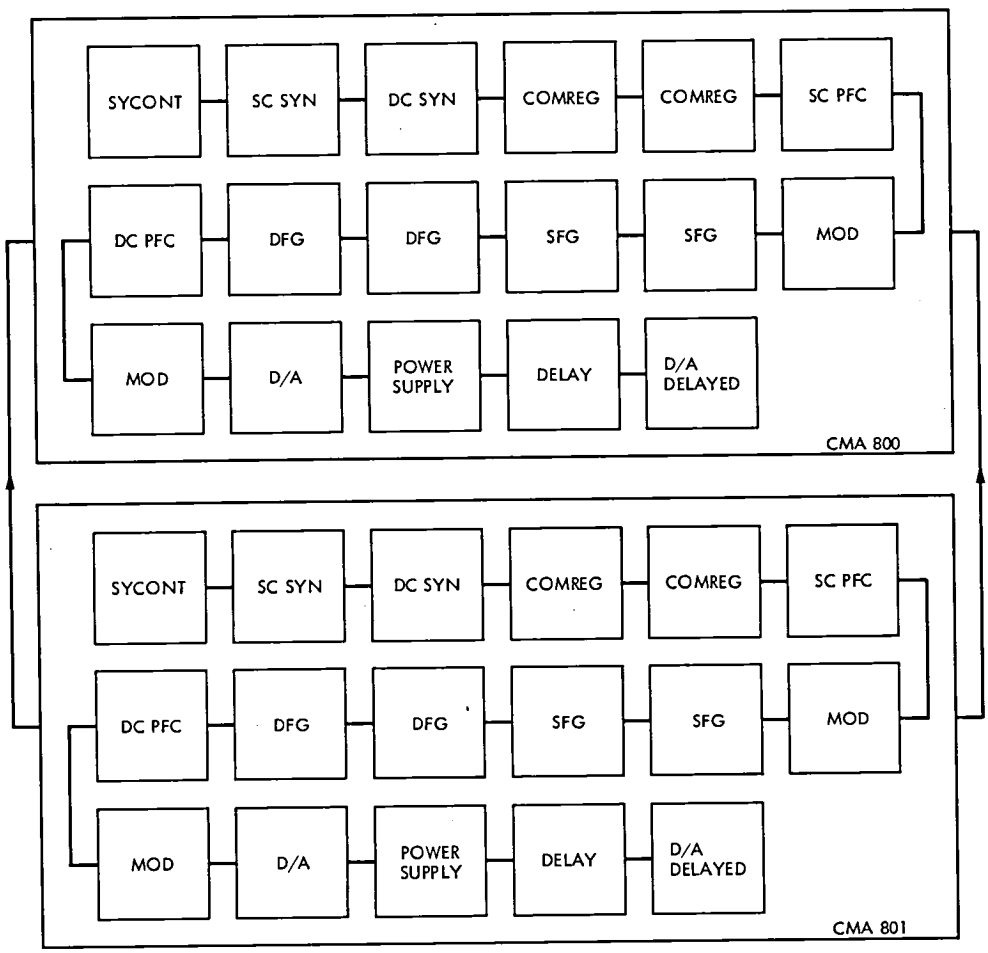

Fig. 2. Command modulator assembly reliability diagram

SIMULATION CONTROL SPECIFICATIONS

STATISTICAL PARAMETERS USED FOR THIS SIMULATION:
250 - MAXIMUM NUMBER OF MISSIONS TO BE RUN
250 - OPTIMUM NUMBER OF MISSIONS TO BE RUN
.998 - SPECIFICATION REQUIREMENT FOR RELIABILITY
1.280 - STANDARD DEVIATION TO BE USED TO CALCULATE LOWER CONFIDENCE LIMIT

985 RANDOM NUMBERS WERE REJECTED PRIOR TO SIMULATION.
SIMULATION BEGINS WITH RANDOM SEED = .94062208

1 PHASE TYPES ARE USED.
1 TIMELINE IS SIMULATED.

PHASE SEQUENCE	TYPE	DURATION	CUMULATIVE TIME
1	1	2184.00	2184.00

PRINTOUT OPTION: MANAGEMENT SUMMARY
REPAIR OPTIONS:
PHASE TYPE 1: REPAIR ALLOWED
100 PERCENT OF REPAIRS ARE PERFORMED ON STATION.

MISSION ALLOWABLE DOWNTIME IS 273.00 HOURS.

MTBF MULTIPLIER = 1.00
MTTR MULTIPLIER = 1.00
BLOCK III CMA

EQUIPMENT CHARACTERISTICS

TYPE	NOMENCLATURE	MTBF	MTTF	DUTY CYCLE	ADMIN DELAY TIME COMPLEX	ADMIN DELAY TIME NETWORK
1	SYCONT	25000.0	2.00	1.00	24.0	336.0
2	SC SYN	12000.0	2.00	1.00	24.0	336.0
3	DC SYN	12000.0	2.00	1.00	24.0	336.0
4	COMREG	25000.0	2.00	1.00	24.0	336.0
5	SC PFC	25000.0	2.00	1.00	24.0	336.0
6	DC PFC	25000.0	2.00	1.00	24.0	336.0
7	DFG	25000.0	2.00	1.00	24.0	336.0
8	SFG	25000.0	2.00	1.00	24.0	336.0
9	MOD	25000.0	2.00	1.00	24.0	336.0
10	D/A	25000.0	4.00	1.00	24.0	336.0
11	POWER SUPPLY	10000.0	2.00	1.00	24.0	336.0
12	DELAY	25000.0	2.00	1.00	24.0	336.0
13	D/A DELAYED	25000.0	4.00	1.00	24.0	336.0

TYPE	EQUIPMENT
1	1 18
2	2 19
3	3 20
4	4 12 21 29
5	5 22
6	6 23
7	7 13 24 30
8	8 14 25 31
9	9 15 26 32
10	10 27
11	11 28
12	16 33
13	17 34

SPARES COMPLEMENT — SPARES MULTIPLIER = 1.00

TYPE	STATION	COMPLEX	NETWORK
1	0	1	0
2	0	1	0
3	0	1	0
4	0	2	0
5	0	1	0
6	0	1	0
7	3	2	0
8	3	2	2
9	0	2	0
10	0	1	0
11	0	1	0
12	0	1	0
13	0	3	0

BLOCK III CMA

Fig. 3. TIGER Program output: simulation control specifications and equipment characteristics

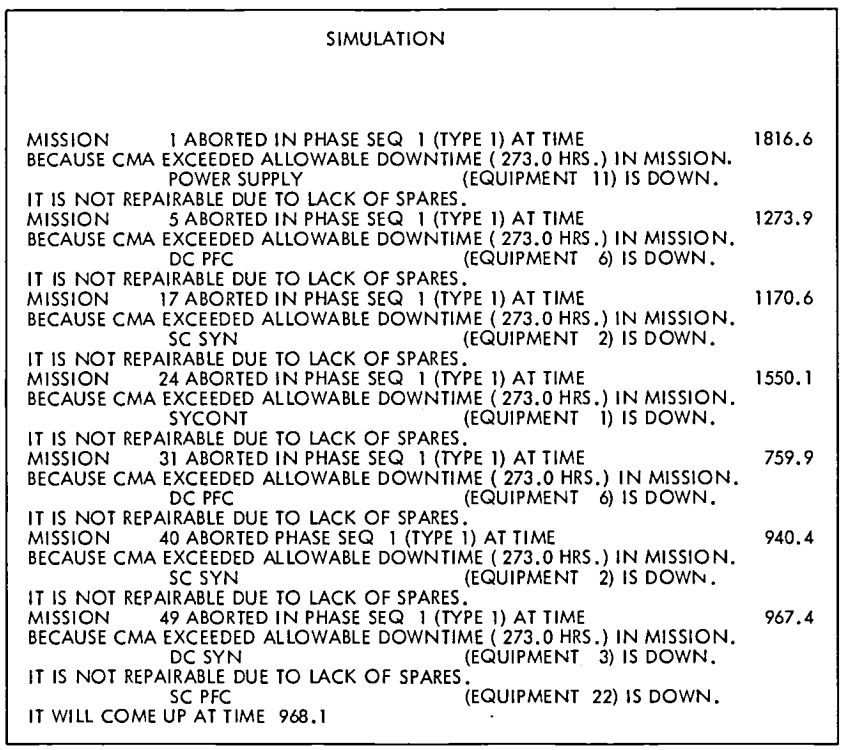

Fig. 4. TIGER Program output: management report

```
                                SIMULATION

START OF MISSION          1********************
  SFG                     (EQUIPMENT  14) FAILED AT TIME          232.1
  SFG                     (EQUIPMENT  14) CAME UP AT TIME         232.9
          SYSTEM WENT DOWN AT TIME 232.1  DOWN TIME IS              .9 HRS.
  POWER SUPPLY            (EQUIPMENT  28) FAILED AT TIME  548.5
  POWER SUPPLY            (EQUIPMENT TYPE  11) CONSUMED ALL SPARES AT TIME      548.5
  POWER SUPPLY            (EQUIPMENT  28) CAME UP AT TIME         574.7
  MOD                     (EQUIPMENT  32) FAILED AT TIME          968.9
  MOD                     (EQUIPMENT  32) CAME UP AT TIME         995.0
  POWER SUPPLY            (EQUIPMENT  11) FAILED AT TIME         1543.6
  DC SYN                  (EQUIPMENT  20) FAILED AT TIME         1906.4
MISSION ABORTED AT TIME  1816.6
  BECAUSE CMA  EXCEEDED ALLOWABLE DOWNTIME (273.0 HRS.) IN MISSION.
    POWER SUPPLY          (EQUIPMENT  11) IS DOWN.
    IT IS NOT REPAIRABLE DUE TO LACK OF SPARES.
    DC SYN                (EQUIPMENT TYPE  3) CONSUMED ALL SPARES AT TIME     1906.4
    DC SYN                (EQUIPMENT  20) CAME UP AT TIME         1930.6
          SYSTEM WENT DOWN AT TIME 1543.6  DOWN TIME IS            387.0 HRS.
    POWER SUPPLY          (EQUIPMENT  28) WILL FAIL AT TIME       2512.2
      2184.0 END OF SEQ  1 (TYPE 1).
  SYSTEM WAS DOWN FOR  253.4 HRS. IN PHASE SEQ  1
  AND REMAINED DOWN AT END OF PHASE.
  START OF MISSION        2********************
  DC SYN                  (EQUIPMENT   3) FAILED AT TIME          428.7
  DC SYN                  (EQUIPMENT TYPE  3) CONSUMED ALL SPARES AT TIME      428.7
  DC SYN                  (EQUIPMENT   3) CAME UP AT TIME         454.4
          SYSTEM WENT DOWN AT TIME  428.7  DOWN TIME IS             25.8 HRS.
  D/A DELAYED             (EQUIPMENT  17) FAILED AT TIME          1157.5
  D/A DELAYED             (EQUIPMENT  17) CAME UP AT TIME         1185.9
          SYSTEM WENT DOWN AT TIME  1157.5  DOWN TIME IS           28.4 HRS.
  SC SYN                  (EQUIPMENT  19) WILL FAIL AT TIME       2629.6
    2184.0 END OF SEQ  1 (TYPE 1).
  START OF MISSION        3********************
  D/A                     (EQUIPMENT  27) FAILED AT TIME          1270.2
  D/A                     (EQUIPMENT TYPE  10) CONSUMED ALL SPARES AT TIME     1270.2
  D/A                     (EQUIPMENT  27) CAME UP AT TIME         1297.4
  D/A                     (EQUIPMENT  27) FAILED AT TIME          2001.9
  COMREG                  (EQUIPMENT   4) FAILED AT TIME          2015.4
  COMREG                  (EQUIPMENT   4) CAME UP AT TIME         2040.9
          SYSTEM WENT DOWN AT TIME  2015.4  DOWN TIME IS           25.6 HRS.
  MOD                     (EQUIPMENT  15) WILL FAIL AT TIME       2206.0
    2184.0 END OF SEQ  1 (TYPE 1).
```

Fig. 5. TIGER Program output: engineering report

```
FIGURES OF MERIT FOR PHASE SEQUENCE  1 (PHASE TYPE 1):
  BEGINNING:    AVAILABILITY (INSTANTANEOUS) = 1.0000
  IN PHASE:
                RELIABILITY =                          .9240
                AVAILABILITY (AVERAGE) =               .9465
                READINESS =                            .9545
  END OF PHASE:  AVAILABILITY (INSTANTANEOUS) =  .8960

FIGURE OF MERIT SUMMARY FOR A GRAND TOTAL OF 250 MISSIONS:

  RELIABILITY              =  .92400          SPECIFICATION    =  .9980
    LOWER CONFIDENCE LIMIT (FOR STANDARD DEVIATION = 1.2800)  =  .9025
  AVAILABILITY (AVERAGE) =  .94648
               (INSTANT) =  .89600
  READINESS              =  .95448
  MEAN TIME BETWEEN MISSION FAILURES (MTBMF) =          27910.6
    LOWER CONFIDENCE LIMIT (90 PERCENT) =               -5101.4 (STD DEV = 1.28)
    VARIANCE =                                      665157560.0
  SYSTEM MEAN UP TIME, MUT (MTBF ESTIMATOR) =           1288.7
  SYSTEM MEAN DOWN TIME, MDT (MTTR ESTIMATOR) =           21.2
SIMULATION COMPLETE - SPECIFIED OPTIMUM NUMBER OF MISSIONS WERE RUN.
SYSTEM FAILS REQUIREMENT.
  BLOCK III CMA
```

Fig. 6. TIGER Program output: system reliability, maintainability and readiness report

EQUIPMENT FAILURES AND CORRECTIVE MAINTENANCE (CM) SUMMARY

EQUIPMENT NUMBER	EQUIPMENT TYPE	EQUIPMENT NOMENCLATURE	TOTAL FAILURES	MISSION AVERAGES FAILURES	MISSION AVERAGES CM MANHOURS
1	1	SYCONT	20	.080	.160
2	2	SC SYN	41	.164	.328
3	3	DC SYN	49	.196	.392
4	4	COMREG	25	.100	.200
5	5	SC PFC	22	.088	.176
6	6	DC PFC	21	.084	.168
7	7	DFG	19	.076	.152
8	8	SFG	20	.080	.160
9	9	MOD	15	.060	.120
10	10	D/A	20	.080	.320
11	11	POWER SUPPLY	51	.204	.408
12	4	COMREG	19	.076	.152
13	7	DFG	27	.108	.216
14	8	SFG	17	.068	.136
15	9	MOD	25	.100	.200
16	12	DELAY	17	.068	.136
17	13	D/A DELAYED	12	.048	.192
18	1	SYCONT	23	.092	.184
19	2	SC SYN	50	.200	.400
20	3	DC SYN	40	.160	.320
21	4	COMREG	20	.080	.160
22	5	SC PFC	24	.096	.192
23	6	DC PFC	18	.072	.144
24	7	DFG	13	.052	.104
25	8	SFG	24	.096	.192
26	9	MOD	14	.056	.112
27	10	D/A	20	.080	.320
28	11	POWER SUPPLY	45	.180	.360
29	4	COMREG	22	.088	.176
30	7	DFG	23	.092	.184
31	8	SFG	21	.084	.168
32	9	MOD	24	.096	.192
33	12	DELAY	16	.064	.128
34	13	D/A DELAYED	14	.056	.224
			831	3.324	7.176

BLOCK III CMA

Fig. 7. TIGER Program output: equipment failures and corrective maintenance summary

NUMBER OF SPARES PER MISSION

EQUIPMENT TYPE	EQUIPMENT NOMENCLATURE	STATION STOCK	STATION USAGE MAX	STATION USAGE AVG	COMPLEX STOCK	COMPLEX USAGE MAX	COMPLEX USAGE AVG	NETWORK STOCK	NETWORK USAGE MAX	NETWORK USAGE AVG
1	SYCONT	0	0	.00	1	1	.16	0	0	.00
2	SC SYN	0	0	.00	1	1	.32	0	0	.00
3	DC SYN	0	0	.00	1	1	.32	0	0	.00
4	COMREG	0	0	.00	2	2	.34	0	0	.00
5	SC PFC	0	0	.00	1	1	.17	0	0	.00
6	DC PFC	0	0	.00	1	1	.15	0	0	.00
7	DFG	3	3	.33	2	0	.00	0	0	.00
8	SFG	3	3	.33	2	0	.00	2	0	.00
9	MOD	0	0	.00	2	2	.30	0	0	.00
10	D/A	0	0	.00	1	1	.14	0	0	.00
11	POWER SUPPLY	0	0	.00	1	1	.33	0	0	.00
12	DELAY	0	0	.00	1	1	.13	0	0	.00
13	D/A DELAYED	0	0	.00	3	1	.10	0	0	.00

BLOCK III CMA

Fig. 8. TIGER Program output: number of spares per mission

EQUIPMENT CONTRIBUTIONS TO SYSTEM UNAVAILABILITY

EQUIPMENT NUMBER	EQUIPMENT TYPE	NOMENCLATURE	DOWNTIME HOURS	UNAVAILABILITY FRACTION	PERCENT CONTRIBUTION
2	2	SC SYN	9181.3	.01682	31.4
11	11	POWER SUPPLY	5521.9	.01011	18.9
6	6	DC PFC	3346.0	.00613	11.5
3	3	DC SYN	2995.1	.00549	10.2
10	10	D/A	2450.6	.00449	8.4
1	1	SYCONT	1714.5	.00314	5.9
5	5	SC PFC	859.3	.00157	2.9
15	9	MOD	720.3	.00132	2.5
4	4	COMREG	636.1	.00116	2.2
12	4	COMREG	501.2	.00092	1.7
16	12	DELAY	397.4	.00073	1.4
9	9	MOD	369.6	.00068	1.3
17	13	D/A DELAYED	334.1	.00061	1.1
13	7	DFG	63.5	.00012	.2
7	7	DFG	47.4	.00009	.2
8	8	SFG	44.8	.00008	.2
14	8	SFG	38.9	.00007	.1

BLOCK III CMA

Fig. 9. TIGER Program output: equipment contributions to system unavailability

EQUIPMENT CONTRIBUTIONS TO SYSTEM UNRELIABILITY

EQUIPMENT NUMBER	EQUIPMENT TYPE	NOMENCLATURE	NUMBER OF FAILURES	UNRELIABILITY FRACTION	PERCENT CONTRIBUTION
2	2	SC SYN	6	.02400	31.6
11	11	POWER SUPPLY	4	.01600	21.1
1	1	SYCONT	2	.00800	10.5
6	6	DC PFC	2	.00800	10.5
10	10	D/A	2	.00800	10.5
3	3	DC SYN	2	.00800	10.5
5	5	SC PFC	1	.00400	5.3

Fig. 10. TIGER Program output: equipment contributions to system unreliability

Special Activity Utilization of GDSCC Antennas During 1981

E. B. Jackson
Goldstone Operations Section

In addition to direct spacecraft support, the GDSCC antennas also support "special" activities. These activities can be categorized as Advanced Systems Program, Radio Astronomy Program, Crustal Dynamics Program, and Operations and Support Activities. This article briefly discusses the goals and categorizes each of the activities that received tracking support at Goldstone during 1981. All Goldstone stations (DSSs 11, 12, 13 and 14) provided a total of 2353.55 hours of support to "special" activities during the period January through December 1981.

I. Introduction

The antennas at the Goldstone Deep Space Communications Complex (GDSCC), in addition to providing telemetry, ranging, and commanding support to spacecraft projects, also support a number of other tasks which require "tracking." These special activities are categorized in this report into Advanced Systems Program, Radio Astronomy Program, Crustal Dynamics Program, and Operations and Support Activities. This report discusses the special activities which were supported with tracking by the GDSCC antennas during the period January through December, 1981.

II. Advanced Systems Program

Activities in this category are funded by NASA through the Office of Space Tracking and Data Systems (OSTDS). This is the development work which culminates in provision, to the Deep Space Network (DSN) stations, of new capability with which each spacecraft project's needs can be met. Related activities are associated and organized into Research and Technology Operations Plans (RTOPs). GDSCC activities in this category are tabulated in Table 1 with hours and stations involved.

A. RTOP 60: Radio Metric Technology Development

The goal of this effort is the development and demonstration of advanced radio metric systems for navigation and radio science, with a specific angular accuracy goal of 50 nanoradians for delta VLBI measurements.

In general, using VLBI, this RTOP generates a catalog of suitable (strength and location) extragalactic radio sources (EGRSs). Using this catalog of EGRSs, the ephemerides of the planets, particularly Mars, are tied into the "radio reference frame." Then techniques are developed for differential measurements between spacecraft and EGRSs which locate the spacecraft within the radio reference frame and hence the spacecraft with reference to the target planet(s). Table 1 lists the various activities within the RTOP for which tracking support was provided at GDSCC during 1981.

B. RTOP 65: Antenna Systems Development

In recognition of the necessity of improving antenna performance to provide increased planetary communications capability, this activity's goal is to enhance antenna technology. Specifically, this RTOP looks at possible improvements in electronic-microwave capabilities and mechanical-structural design. Application of technology to provide higher frequency operation of existing antennas, along with more sophisticated techniques of antenna pointing, is also a part of this activity.

As part of the analysis performed in this area, techniques for measurement of antenna gain were refined and used to make extensive measurements at DSS 12. These antenna gain measurements were used to quantify and evaluate the changes in microwave performance resulting from main reflector surface alignment and changes in subreflector position as a function of antenna attitude.

The particular activity supported during 1981 at DSS 13 was "Analytical Techniques and Procedures," which has as its objective the development of analysis software for application to antenna structural and mechanical performance. (An innovative application used a cooled infrared camera to obtain thermal measurements of the DSS 13 26-m antenna backup structure. These measurements supplied information on possible thermally induced structural deformations which was not heretofore available.) This activity also aims to extend the capability for automatic antenna structural design optimization and organize existing software to simplify maintenance and execution of improvements. Again, Table 1 depicts tracking support during 1981.

C. RTOP 68: Station Monitor and Control Technology

Recognizing that a substantial portion of the operating cost for DSN stations is allocated to personnel, this RTOP seeks to develop automation technology that will allow entire station operation from a remote point and prove the reliability, safety, and efficiency of unattended operation. Additionally, this RTOP plans to develop the data base with which reliability, costs, and productivity can be monitored, using DSS 13 as a demonstration unattended station.

Table 1 lists only tracking support to this activity; substantial other work was also ongoing at DSS 13 during the year as the equipment used to make DSS 13 operate in the unattended mode evolved and additional systems were added to those controlled remotely.

D. RTOP 70: High-Speed Signal Processing Research

The objective of this RTOP is to develop high-speed digital signal processing techniques for use in the DSN. A major part of this task is the development of a test bed as a research tool used to explore high-speed techniques. The test bed is to be used for demonstrations of various development capabilities, such as high-performance array processors and wideband correlation subsystems. This work also demonstrates commercial LSI signal processing building blocks and utilizes promising commercial design systems.

The particular activity supported at GDSCC during 1981 was Radar Data Acquisition, which uses various planets and asteroids as targets for demonstration of signal processing techniques.

In Table 1 are listed the various targets which were explored in 1981 as the demonstration test bed was used to develop signal processing techniques.

III. Radio Astronomy Program

In general, activities in this category are either sponsored by the Office of Space Science (OSS) or authorized by the Radio Astronomy Experiment Selection (RAES) panel.

Experimenters within NASA who desire OSS support of their activities submit an observing plan in the form of an RTOP. If approved, OSS requests OSTDS to provide support, and time is made available on suitable facilities of the DSN. Experimenters from universities who have observing plans that require NASA facilities submit their observing plan to the RAES panel. If approved, time is made available through an agreement whereby NASA makes available a percentage of the operational time on DSN facilities. Table 2 depicts the support at GDSCC in this area during 1981.

A. OSS-Sponsored Activities

1. Pulsar rotation constancy. This experiment seeks to monitor short-term variations in the period of the relatively young VELA pulsar (PSR 0833-45). Additionally, by observing 23 older, more stable pulsars, this experiment hopes to obtain data that will provide further tests of the hypothesis that pulsars are neutron stars resulting from supernova explosions, which impart high velocities to the resulting pulsar.

2. Planetary radio astronomy. This experiment has the dual objectives of studying the properties of the planet Jupiter's radio emission and measurement of the thermal emission from the atmosphere of the outer planets. A new objective is to search for a link between variations in the Io plasma Torus and Jupiter's radio emissions. These observations will aid construction of improved models of Jupiter's radiation belt environment as well as atmospheric models of the outer planets, particularly Uranus.

3. **SETI Receiving System Stability Measurements.** In anticipation of a SETI observing program (which never materialized), the phase and amplitude stability of the various receiving systems at DSS 14 was measured.

B. JPL Director's Discretionary Fund Sponsored Activities

1. **Science utilization of the Radio Frequency Interference Surveillance Subsystem (SURFISS).** As part of the task of detection and characterization of radio frequency interference, the DSN has developed a unique capability to perform high-resolution spectrum analysis. This van-mounted subsystem can perform real-time spectral analysis of a 20-MHz band of frequencies, using 2^{16} channels, resulting in a resolution of 305 Hz. The objective of this task was to develop computer programming and observing techniques which would best make use of this high-resolution, wide bandwidth capability to perform radio astronomical observations. In particular, the RFI subsystem, with altered software, would be used to observe fine structure and narrow spectral features in radio astronomical objects.

The RFI subsystem, coupled to the 26-m antenna, was used at DSS 13, to observe, among others, the H142α line in M17. This line was observed at approximately 2272.3 MHz.

C. RAES Panel Sponsored Activities

1. **VLBI investigation of SS-433 (RA-175).** SS-433 has a bizarre optical spectrum that exhibits three sets of emission lines. One of these three emission lines shows near-zero radial velocity, while the other two show large and variable shifts to the blue and the red. The variability is periodic, with a period of about 164 days.

This experiment conducts regular VLBI observations of this source, using many simultaneous baselines. These multiple baselines should enable determination of the source angular size and structure, which will aid modeling. These observations show that the compact radio structure is also variable, with a period of 164 days. The involved stations at GDSCC include DSS 13 and DSS 14, along with a number of other radio observatories in the United States and Europe.

2. **VLBI investigation of "twin" quasistellar objects (QSOs) 0957 + 561A, B (RA 176).** These QSOs, designated 0957 + 561A, B, are separated by only 6 arc seconds in angle and have equal optical redshifts and remarkable similarity in their optical spectra. This similarity is inconsistent with chance alone, so the objects are in some manner physically associated. One theory proposes that there is only one object, whose radiation is gravitationally bent about an intervening massive lens, a "gravitational lens."

This experiment uses VLBI observations with many simultaneous baselines to provide data with which detailed structure maps can be prepared. Repeated observations could monitor changes in the radio brightness distribution. At GDSCC, the involved antenna is DSS 14.

3. **Milliarcsecond nuclei in quasars and galaxies (RA-177).** The 64-m antennas at Goldstone, California, and Madrid, Spain, connected as a Very Long Baseline Interferometer (VLBI), have a detection sensitivity of 1 mJy at S-band and 2 mJy at X-band. This task uses this sensitive interferometer to determine the frequency of occurrence of milliarcsecond radio nuclei in radio quasars and radio galaxies. These two antennas, used in the VLBI configuration, generate detailed maps of the nuclei of these extragalactic objects. A knowledge of the statistical occurrence and properties of these nuclei will aid in a more detailed understanding of the role these nuclei play in the energetics and evolution of extragalactic objects.

IV. Crustal Dynamics Program

A Crustal Dynamics Program goal is the demonstration of the capability of VLBI systems to make highly accurate geodetic measurements. The particular activity supported at GDSCC during 1981 is Mobile VLBI Field Operations. The thrust of the Mobile VLBI activity is to demonstrate the geodetic performance of highly mobile (antenna size approximately 4 meters) VLBI stations while providing accurate data of significant geophysical interest. By moving around California and making VLBI measurements with base stations located at GDSCC, Owens Valley Radio Observatory, and other fixed points, the Mobile VLBI activity is able to accumulate data on regional deformation and strain accumulation, particularly as associated with the San Andreas Fault.

These measurements are usually scheduled for periods of 7 to 10 days, in excess of 24 hours observing at a time, and a number of suitable radio sources are observed simultaneously and repeatedly by all the stations involved. During the period January 1 through December 31, 1981, DSS 13 (Venus Station) provided 418.75 hours of tracking support to these measurements of crustal deformation along the San Andreas Fault.

V. Operations and Support Program

The maintenance of a capability to observe at various frequencies, on a routine basis, involves a number of activities which do not easily fit any of the specific programs supported at GDSCC, but these activities are essential to continued support of any or all programs. For the purposes of this progress

report, these activities are grouped under the heading "Operations and Support." These activities are tabulated in Table 3, along with hours and stations involved.

A. Antenna Boresight Offset Measurements

At DSS 13, where developmental Cassegrain feedcones are routinely used for program support, continued knowledge of the offset between the antenna mechanical axis and the antenna electromagnetic axis, as a function of antenna attitude, is essential. By use of suitable radio calibration sources, on which the antenna is "boresighted" (usually at 15-minute intervals of time), a table of axis offsets as a function of antenna attitude can be generated. This table can then be used to provide assurance of accurate "blind pointing" on objects such as weak radio sources where no real-time indication of correct pointing can be obtained.

B. High Resolution Analysis, Transmitter(s) Radiated Spectrum

As part of the overall electromagnetic compatibility program at DSCC, the actual radiated spectrum of the various transmitters at DSS 14 was measured. These measurements utilized the Department of Commerce radio frequency measuring van, coupled with the JPL developed high resolution spectrum analysis subsystem, usually referred to as the "RFI Van." Measurements were made on the 20- and 100-kW S-band transmitters and the 400-kW X-band transmitter. Partial measurements were also made on the 400-kW S-band transmitter. These measurements characterized the radiated spectrum of each of the transmitters, including carriers and associated spurious signals, with a maximum resolution of 305 Hz.

C. Precision Signal Strength Measurements, ISEE-3

Signal strength measurements of ISEE-3, made in the conventional fashion (using automatic gain control voltage as an analog of signal strength) were not of appropriate precision or resolution. Using equipment normally used for radio astronomy activities, DSS 12 and 13 made direct measurement of the power ratio in a narrow bandwidth (10 kHz nominal) with and without the spacecraft signal present. With knowledge of the receiving system temperature, the spacecraft signal strength can be accurately computed from these power ratios.

D. Electromagnetic Compatibility Testing (Sodium Lamp)

Nighttime illumination around the antennas is essential, but should be of minimum energy consumption. Sodium vapor lighting is efficient but the potential for radio frequency interference to the DSN antennas was unknown. At DSS 13, the sodium lamp, in the fired and unfired state, was positioned over the antenna feedhorn and, using specialized equipment, the possible level of interference was determined. It was concluded that lamps of this type are suitable for ground installation around DSN antennas.

E. Precision Signal Strength Measurements, ALSEP-16

Antenna gain measurements can be, and are, made using radio calibration sources. However, from time to time, it is desirable to have available a far-field source which radiates a strong, narrrow-band, stable signal. The radio transmitters left on the Moon by the Apollo astronauts are quite suitable for this purpose, but occasional characterization of the signals is necessary. These measurements were to determine the continued suitability of ALSEP-16 as a stable far-field signal source. On the DSS 13 26-m antenna, ALSEP-16 was measured at -110 dbm signal level.

F. VLBI Software Development

When performing VLBI measurements, which depend upon correlation of two (or more) signals, real-time information about proper functioning of the station is desirable. Utilizing RF signals generated at the DSS 14 antenna, modifications were made to in-use software to enhance its utility for real-time performance evaluation.

G. Antenna Location Determination, National Geodetic Survey

VLBI measurements of vector distances between participating stations require accurate knowledge of the geodetic location of a reference point on the antennas used to make these observations. On the DSS 13 antenna, this point is the intersection of the azimuth and elevation axes. Personnel from the National Geodetic Survey agency required access to the DSS 13 26-m antenna in order to tie this axis intersection into the continental grid locations. To aid these measurements, the 26-m antenna was intermittently positioned as required over a period of a few weeks.

Table 1. Advanced Systems Program utilization of GDSCC antennas during 1981

Activity	Station and tracking hours provided			
	11	12	13	14
RTOP 60 radio metric technology development				
Mark IV radio metric system development and demonstration			101.75	5.25
VLBI radio source identification			102.00	16.50
5 nanoradian VLBI system analysis and modeling			52.00	
Microwave phase delay calibration			44.75	14.25
Clock synchronization VLBI			14.25	
RTOP 65 antenna systems development				
Analytical techniques and procedures		140.75[a]	33.25	
RTOP 68 station monitor and control technology				
DSS 13 S/X unattended system development			22.50	
RTOP 70 high-speed signal processing research				
Radar data acquisition				
Asteroid Melpomene				6.00
Planet Mercury			4.25	58.00
Planet Saturn and Rings of Saturn				20.25
Callisto (satellite of Jupiter)				29.25
Totals		140.75	374.75	149.50

[a]Antenna gain measurements.

Table 2. Radio astronomy utilization of GDSCC antennas during 1981

Activity	Station and tracking hours provided			
	11	12	13	14
OSS sponsored activities				
Pulsar rotation constancy	117.00	3.25	184.75	81.00
Planetary radio astronomy			207.25	30.50
SETI receiving system stability measurements				26.50
JPL Director's Discretionary Fund sponsored activities				
Science utilization of the Radio Frequency Interference Surveillance Subsystem (SURFISS)			45.25	
RAES panel sponsored activities				
VLBI investigation of SS-433-RA 175			57.25	26.00
VLBI investigation of "twin" quasistellar objects (QSOs) 0957 + 561A, B and 1038 + 528A, B-RA 176				52.25
Milliarcsecond nuclei in quasars and galaxies-RA 177				15.50
Totals	117.00	3.25	494.50	231.50

Table 3. Station operations and associated activity utilization of GDSCC antennas during 1981

Activity	Station and tracking hours provided			
	11	12	13	14
Antenna boresight offset measurements			80.50	
High resolution analysis, transmitter(s) radiated spectrum				17.00
Precision signal strength measurements, ISEE-3		5.00	4.25	
Electromagnetic compatability testing (sodium lamp)			5.00	
Precision signal strength measurements, ALSEP-16			2.75	
VLBI software development				2.00
Antenna location determination, National Geodetic Survey			171.25	
Totals		5.00	263.75	19.00

Maintenance and Operations Tasks Accomplished at DSS 12 During the Antenna Panel Replacement Downtime

L. Butcher, T. Jonas, and W. Wood
Goldstone Operations Section

The heavy schedule of tracking activities at the Echo Deep Space Station (DSS 12) prevents some time-consuming maintenance tasks from being performed. Careful coordination prior to and during a mandatory task (antenna panel replacement) made it possible to do a large number of unrelated tasks that ordinarily would have to be deferred. It is not the intent to relate the activities of the antenna panel replacement but to describe the maintenance and operations tasks accomplished during the downtime.

I. Introduction

An eight-week period, from 22 February to 19 April 1981, was set aside to correct antenna gain deficiencies in the 34-meter antenna at Goldstone, California. To take advantage of the station availability during the antenna downtime, the Goldstone Maintenance and Integration Unit worked closely with DSN Engineering (Section 355). This coordination made time available to do things that would not normally be done because of the heavy tracking commitments.

II. Maintenance Activities

The following maintenance and operations tasks were accomplished during the antenna panel replacement downtime:

(1) Seven Engineering Change Orders were implemented:

Number	Title	Subsystem
79.006	Symbol Synchronizer Assembly Upgrade	40.3
79.152	Host Processor Installation	Various
79.159	Radio Frequency Power Supply Monitor	2.1
79.269	High Voltage Cable Isolation	2.0
79.272	Angle Encoder Translator Damage	6.7
79.292	Add Radiometer Experiment	Various
80.205	Generator Control Logic Modification	39.2

(2) Corrective maintenance had to be carefully scheduled and accomplished on a not-to-interfere with the antenna panel replacement work basis.

(a) All Frequency and Timing System cables were checked and rerouted to eliminate a long standing problem of intermittent failures. Included in this work was the retermination of system ground cables to reduce ground loop problems that had existed for years.

(b) The coolant lines at the 20-kW S-band transmitter were disassembled and resealed to prevent leaks.

(c) The hour angle and declination axes cable wraps were reworked to eliminate existing and future cable damage.

(d) Defective wiring in the backup S-band maser control cable was repaired by using spare wires within the existing cable.

(e) A large amount of corrective maintenance was accomplished on the Digital Instrumentation Assembly.

(3) Workmanship Assurance Discrepancy Report work. During the antenna downtime, 26 discrepancy reports, containing a total of 59 separate items, were corrected and cleared. Deep Space Station 12 is now at an alltime low in the number of outstanding Workmanship Assurance Discrepancy Reports.

(4) Systems Testing:

(a) To prepare for expected DSN support of the International Sun-Earth Explorer III (ISEE-3) satellite ranging compatibility tracks, the power klystron from the 20-kW transmitter was removed and tested at the Goldstone Microwave Test Facility. Data for retuning the klystron were obtained to permit rapid frequency changing during later operational testing.

(b) Following the completion of the antenna panel work, seven radio source star tracks were carried out to determine antenna gain and to realign the antenna subreflector for optimum performance.

(c) To assure full and complete performance of all station systems, a complete set of System Performance Tests (SPTs) was performed for telemetry, command and radio metric data.

III. Summary

With careful planning and coordination with the Engineering Task Manager, time-consuming maintenance tasks were accomplished during the major downtime activity. These tasks could not have been accomplished during the normally scheduled short maintenance periods because of tracking commitments. All scheduled maintenance and operations activities were successfully accomplished on schedule.

Bibliography

Ananda, M. P., "Lunar Gravity: A Mass Point Model," *J. Geophys. Res.*, Vol. 82, No. 20, pp. 3049-3064, July 10, 1977.

Anderson, J. D., et al., "Experimental Test of General Relativity Using Time-Delay Data From Mariner 6 and Mariner 7," *Astrophys. J.*, Vol. 200, No. 1 pp. 221-233, Aug. 15, 1975.

Anderson, J. D., et al., "Tests of General Relativity Using Astrometric and Radio Metric Observations of the Planets," *Acta Astronautica*, Vol. 5, No. 1-2, pp. 43-61, Jan.-Feb. 1978.

Barton, W. R., and Miller, R. B., *Tracking and Data System Support for the Pioneer Project: Pioneer 11–Prelaunch Planning Through Second Trajectory Correction: 'to May 1, 1973*, Technical Memorandum 33-584, Vol. II, Jet Propulsion Laboratory, Pasadena, Calif., Mar. 15, 1975.

Bartos, K. P., et al., *Implementation of the 64-Meter-Diameter Antennas at the Deep Space Stations in Australia and Spain*, Technical Memorandum 33-692, Jet Propulsion Laboratory, Pasadena, Calif., Jan. 15, 1975.

Bathker, D. A., Brown, D. W., and Petty, S. M., *Single- and Dual-Carrier Microwave Noise Abatement in the Deep Space Network*, Technical Memorandum 33-733, Jet Propulsion Laboratory, Pasadena, Calif., Aug. 1, 1975.

Bathker, D. A., *Microwave Performance Characterization of Large Space Antennas*, JPL Publication 77-21, Jet Propulsion Laboratory, Pasadena, Calif., May 15, 1977.

Beatty, R. W., and Otoshi, T. Y., "Effect of Discontinuities on the Group Delay of a Microwave Transmission Line," *IEEE Trans. Microwave Theor. Techniq.*, Vol. MTT-23, No. 11, pp. 919-923, Nov. 1975.

Benjauthrit, B., and Reed, I. S., "Galois Switching Functions and Their Applications," *IEEE Trans. Comput.*, Vol. C-25, No. 1, pp. 78-86, Jan. 1976.

Benjauthrit, B., and Reed, I. S., "On the Fundamental Structure of Galois Switching Functions," *IEEE Trans. Comput.*, Vol. C-27, No. 8, pp. 757-762, Aug. 1978.

Berlekamp, E. R., et al., "On the Inherent Intractability of Certain Coding Problems," *IEEE Trans. Inform. Theor.*, Vol. IT-24, No. 3, pp. 384-386, May 1978.

Berman, A. L., and Ramos, R., "Pioneer Venus Occultation Radio Science Data Generation," *IEEE Trans. Geosci. and Remote Sensing*, Vol. GE-18, No. 1. pp. 11-14, Jan. 1980.

Berman, A. L. and Rockwell, S. T., *New Optical and Radio Frequency Angular Tropospheric Refraction Models for Deep Space Applications*, Technical Report 32-1601, Jet Propulsion Laboratory, Pasadena, Calif., Nov. 1, 1975.

Berman, A. L. *The Prediction of Zenith Range Refraction From Surface Measurements of Meteorological Parameters*, Technical Report 32-1602, Jet Propulsion Laboratory, Pasadena, Calif., July 15, 1976.

Born, G. H., and Mohan, S. N., "Orbit Determination for Mariner 9 Using Radio and Optical Data," *J. Spacecraft Rockets*, Vol. 12, No. 7, pp. 439-441, July 1975.

Butman, S. A., "Linear Feedback Rate Bounds for Regressive Channels," *IEEE Trans. Inform. Theor.*, Vol. IT-22, No. 3, pp. 363-366, May 1976.

Butman, S. A., et al., "Design Criteria for Noncoherent Gaussian Channels With MFSK Signaling and Coding," *IEEE Trans. Commun.*, Vol. COM-24, No. 10, pp. 1078-1088, Oct. 1976.

Butman, S. A., and Lesh, J. R., "The Effects of Bandpass Limiters on *n*-Phase Tracking Systems," *IEEE Trans. Commun.*, Vol. COM-25, No. 6, pp. 569-576, June 1977.

Chao, C.-C., "Interstation Frequency Offset Determination Using Differenced 2-Way/3-Way Doppler Data," paper presented at the 1978 Spring Meeting of the American Geophysical Union, Miami, Florida, Apr. 17-20, 1978.

Christensen, C. S., and Reinold, S. J., "Navigation of the Mariner 10 Spacecraft to Venus and Mercury," *J. Spacecraft Rockets*, Vol. 12, No. 5, pp. 280-286, May 1975.

Christensen, C. S., et al., "On Achieving Sufficient Dual Station Range Accuracy for Deep Space Navigation at Zero Declination," paper presented at AAS/AIAA Astrodynamics Specialist Conference, Jackson Hole, Wyo., Sept. 7-9, 1977.

Christensen, E. J., et al., "The Mass of Phobos from Viking Flybys," *Geophys. Res. Lett.*, Vol. 4, No. 12, pp. 555-557, Dec. 1977.

Clauss, R., Flesner, L. D., and Schultz, S., "Simple Waveguide Reflection Maser with Broad Tunability," *Rev. Sci. Instrum.*, Vol. 48, No. 8, pp. 1104-1105, Aug. 1977.

A Collection of Articles on S/X-Band Experiment Zero Delay Ranging Tests, Technical Memorandum 33-747, Vol. I, Jet Propulsion Laboratory, Pasadena, Calif., Nov. 1, 1975.

Curkendall, D. W., "Algorithms for Isolating Worst Case Systematic Data Errors," *J. Guidance Contr.*, Vol. 1, No. 1, pp. 56-62, Jan.-Feb. 1978.

Dickinson, R. M., "The Beamed Power Microwave Transmitting Antenna," *IEEE Trans. Microwave Theor. Tech.*, Vol. MTT-26, No. 5, pp. 335-340, May 1978.

Downs, G. S., and Reichley, P. E., *Techniques for Measuring Arrival Times of Pulsar Signals I: DSN Observations from 1968 to 1980*, Publication 80-54, Jet Propulsion Laboratory, Pasadena, Calif., Aug. 15, 1980.

Duxbury, T. C., Johnson, T. V., and Matson, D. L., "Galilean Satellite Mutual Occultation Data Processing," *Icarus*, Vol. 25, No. 4, pp. 569-584, Aug. 1975.

Edelson, R. E., "An Observational Program to Search for Radio Signals From Extraterrestrial Intelligence Through the Use of Existing Facilities," Preprint IAF-A-76-033, Int. Astronaut. Fed. XXVII Congress, Anaheim, Calif., Oct. 10-16, 1976.

Edelson, R. E., and Levy, G. S., "The Search for Extraterrestrial Intelligence: Telecommunications Technology," *Proceedings of the 1976 National Telecommunications Conference*, Vol. I, Dallas, Tex., Nov. 29-Dec. 1, 1976.

Edelson, R. E., "An Experimental Protocol for a Search for Radio Signals of Extraterrestrial Intelligent Origin in the Presence of Man-Made Radio Frequency Sources," paper presented at the XXVIIIth International Astronautical Congress, Prague, Czechoslovakia, Sept. 25-Oct. 1, 1977.

Estabrook, F. B., and Wahlquist, H. D., "Response of Doppler Spacecraft Tracking to Gravitational Radiation," *Gen. Relat. Grav.*, Vol. 6, No. 5, pp. 439-447, Oct. 1975.

Estacion Espacial de Madrid: Madrid Space Station, Special Publication 43-26, Jet Propulsion Laboratory, Pasadena, Calif., Aug. 31, 1975.

Evans, R. H., Kent, S. S., and Seidman, J. B., *Satellite Remote Sensing Facility for Oceanographic Applications*, Publication 80-40, Jet Propulsion Laboratory, Pasadena, Calif., July 1, 1980.

Ferrari, A. J., and Ananda, M. P., "Lunar Gravity: A Long-Term Keplerian Rate Method," *J. Geophys. Res.*, Vol. 82, No. 20, pp. 3085-3097, July 10, 1977.

Fjeldbo, G., et al., "Viking Radio Occultation Measurements of the Martian Atmosphere and Topography: Primary Mission Coverage," *J. Geophys. Res.*, Vol. 82, No. 28, pp. 4317-4324, Sept. 30, 1977.

Fortenberry, J. W., Freeland, R. E., and Moore, D. M., *Five-Meter-Diameter Conical Furlable Antenna*, Technical Report 32-1604, Jet Propulsion Laboratory, Pasadena, Calif., July 15, 1976.

Freiley, A. J., Batelaan, P. D., and Bathker, D. A., *Absolute Flux Density Calibrations of Radio Sources: 2.3 GHz*, Technical Memorandum 33-806, Jet Propulsion Laboratory, Pasadena, Calif., Dec. 1, 1977.

Goldstein, R. M., and Morris, G. A., "Ganymede: Observations by Radar," *Science*, Vol. 188, No. 4194, pp. 1211-1212, June 20, 1975.

Goldstein, R. M., Green, R. R., and Rumsey, H., Jr., "Venus Radar Images," *J. Geophys. Res.*, Vol. 81, No. 26, pp. 4807-4817, Sept. 10, 1976.

Goodwin, P. S., et al., *Tracking and Data Systems Support for the Helios Project: Project Development Through End of Mission Phase II*, Technical Memorandum 33-752, Vol. I, Jet Propulsion Laboratory, Pasadena, Calif., July 1, 1976.

Goodwin, P. S., et al., *Tracking and Data Systems Support for the Helios Project: DSN Support of Project Helios April 1975 Through May 1976*, Technical Memorandum 33-752, Vol. II, Jet Propulsion Laboratory, Pasadena, Calif., Jan. 15, 1977.

Goodwin, P. S., Jensen, W. N., and Flanagan, F. M., *Tracking and Data Systems Support for the Helios Project: DSN Support of Project Helios May 1976 Through June 1977*, Technical Memorandum 33-752, Vol. III, Jet Propulsion Laboratory, Pasadena, Calif., Mar. 1, 1979.

Gulkis, S., et al., "An All-Sky Search for Narrow-Band Radiation in the Frequency Range 1-25 GHz," paper presented at the 1976 U.S. National Commission, International Union of Radio Science, Amherst, Mass., Oct. 10-15, 1976.

Harris, A. W., et al., "2290-MHz Flux Densities of 52 High-Declination Radio Sources," *Astron. J.*, Vol. 81, No. 4, pp. 222-224, Apr. 1976.

Higa, W. H., "Spurious Signals Generated by Electron Tunneling on Large Reflector Antennas," *Proc. IEEE*, Vol. 63, No. 2, pp. 306-313, Feb. 1975.

Higa, W. H., *The Superconducting Cavity-Stabilized Maser Oscillator*, Technical Memorandum 33-805, Jet Propulsion Laboratory, Pasadena, Calif., Dec. 15, 1976.

Hunter, J. A., "Orbiting Deep Space Relay Station, A Study Report," paper presented at AIAA Conference on Large Space Platforms, Future Needs and Capabilities, Los Angeles, Calif., Sept. 27-29, 1978.

Jacobson, R. A., McDanell, J. P., and Rinker, G. C., "Use of Ballistics Arcs in Low Thrust Navigation," *J. Spacecraft Rockets*, Vol. 12, No. 3, pp. 138-145, Mar. 1975.

Jurgens, R. F., and Goldstein, R. M., "Radar Observations at 3.5 and 12.6 cm Wavelength of Asteroid 433 Eros," *Icarus*, Vol. 28, No. 1, pp. 1-15, May 1976.

Jurgens, R. F., and Bender, D. F., "Radar Detectability of Asteroids," *Icarus*, Vol. 31, No. 4, pp. 483-497, Aug. 1977.

Katow, M. S., "Evaluating Computed Distortions of Parabolic Reflectors," *Record of IEEE 1977 Mechanical Engineering in Radar Symposium, Arlington, Virginia, Nov. 8-10, 1977*, IEEE Publication 77CH 1250-0 AES, pp. 91-93.

Kliore, A. J., Woiceshyn, P. M., and Hubbard, W. P., "Pioneer 10 and 11 Radio Occultations by Jupiter," *COSPAR Space Research*, Vol. XVII, pp. 703-710, Pergamon Press Ltd., Oxford, 1978.

Kliore, A., et al., "The Polar Ionosphere of Venus Near the Terminator From Early Pioneer Venus Orbiter Radio Occultation," *Science*, Vol. 203, No. 4382, pp. 765-768, Feb. 23, 1979.

Kuiper, T. B. H., and Morris, M., "Searching for Extraterrestrial Civilizations," *Science*, Vol. 196, pp. 616-621, May 6, 1977.

Lesh, J. R., "Sequential Decoding in the Presence of a Noisy Carrier Reference," *IEEE Trans. Commun.*, Vol. COM-23, No. 11, pp. 1292-1297, Nov. 1975.

Levitt, B. K., "Long Frame Sync Words for Binary PSK Telemetry," *IEEE Trans. Commun.*, COM-23, No. 11, pp. 1365-1367, Nov. 1975.

Levy, G. S., et al., "Helios-1 Faraday Rotation Experiment: Results and Interpretations of the Solar Occultations in 1975," *J. Geophys.*, Vol. 42, No. 6, pp. 659-672, 1977.

Levy, R., "Computer-Aided Design of Antenna Structures and Components," *Comput. Struc.*, Vol. 6, Nos. 4/5, pp. 419-428, Aug./Oct. 1976.

Levy, R., and McGinness, H., *Wind Power Prediction Models*, Technical Memorandum 33-802, Jet Propulsion Laboratory, Pasadena, Calif., Nov. 15, 1976.

Levy, R., and Katow, M. S., "Implementation of Wind Performance Studies for Large Antenna Structures," *Record of IEEE 1977 Mechanical Engineering in Radar Symposium, Arlington, Virginia, Nov. 8-10, 1977*, IEEE Publication 77CH 1250-0 AES, pp. 27-33.

Levy, R., "Antenna Bias Rigging for Performance Objective," *Record of IEEE 1977 Mechanical Engineering in Radar Symposium, Arlington, Virginia, Nov. 8-10, 1977*, IEEE Publication 77CH 1250-0 AES, pp. 94-97.

Liu, A. S., and Pease, G. E., "Spacecraft Ranging From a Ground Digitally Controlled Oscillator," *J. Spacecraft Rockets*, Vol. 12, No. 9, pp. 528-532, Sept. 1975.

Martin, W. L., and Zygielbaum, A. I., *Mu-II Ranging*, Technical Memorandum 33-768, Jet Propulsion Laboratory, Pasadena, Calif., May 15, 1977.

Melbourne, W. G., "Navigation between the Planets," *Sci. Amer.*, Vol. 234, No. 6, pp. 58-74, June 1976.

Miller, R. B., *Tracking and Data System Support for the Pioneer Project: Pioneer 10–From April 1, 1972, Through the Jupiter Encounter Period, January 1974*, Technical Memorandum 33-584, Vol. III, Jet Propulsion Laboratory, Pasadena, Calif., June 15, 1975.

Miller, R. B., et al., *Tracking and Data System Support for the Pioneer Project: Pioneer 10–From January 1974 to January 1975; Pioneer 11–From May 1, 1973 Through Jupiter Encounter Period, January 1975,* Technical Memorandum 33-584, Vol. IV, Jet Propulsion Laboratory, Pasadena, Calif., Dec. 1, 1975.

Mudgway, D. J., *Tracking and Data System Support for the Viking 1975 Mission to Mars: Prelaunch Planning, Implementation, and Testing*, Technical Memorandum 33-783, Vol. I, Jet Propulsion Laboratory, Pasadena, Calif., Jan. 15, 1977.

Mudgway, D. J., and Traxler, M. R., *Tracking and Data System Support for the Viking 1975 Mission to Mars: Launch Through Landing of Viking 1*, Technical Memorandum 33-783, Vol. II, Jet Propulsion Laboratory, Pasadena, Calif., Mar. 15, 1977.

Mudgway, D. J., *Tracking and Data System Support for the Viking 1975 Mission to Mars: Planetary Operations*, Technical Memorandum 33-783, Vol. III, Jet Propulsion Laboratory, Pasadena, Calif., Sept. 1, 1977.

Mudgway, D. J., *Tracking and Data System Support for the Viking 1975 Mission to Mars: Extended Mission Operations December 1976 to May 1978,* Technical Memorandum 33-783, Vol. IV, Jet Propulsion Laboratory, Pasadena, Calif., Dec. 15, 1978.

Muhleman; D. O., Esposito, P. B., and Anderson, J. D., "The Electron Density Profile of the Outer Corona and the Interplanetary Medium From Mariner-6 and Mariner-7 Time-Delay Measurements," *Astrophys. J.,* No. 211, No. 3, Part 1, pp. 943-957, Feb. 1, 1977.

Murray, B. C., Gulkis, S., and Edelson, R. E., "Extraterrestrial Intelligence: An Observational Approach," *Science,* Vol. 199, No. 4328, pp. 485-492, Feb. 3, 1978.

Ohlson, J. E., "Polarization Tracking of a Partially Coherent Signal Using a Double Loop," *IEEE Trans. Commun.,* Vol. COM-23, No. 9, pp. 859-866, Sept. 1975.

Ohlson, J. E., and Reid, M. S., *Conical-Scan Tracking With the 64-m-diameter Antenna at Goldstone,* Technical Report 32-1605, Jet Propulsion Laboratory, Pasadena, Calif., Oct. 1, 1976.

Ong., K. M., et al., "A Demonstration of a Transportable Radio Interferometric Surveying System With 3-cm Accuracy on a 307-m Base Line," *J. Geophys. Res.,* Vol. 81, No. 20, pp. 3587-3593, July 10, 1976.

Otoshi, T. Y., and Stelzried, C. T., "Cosmic Background Noise Temperature Measurement at 13-cm Wavelength," *IEEE Trans. Instr. Meas.,* Vol. IM-24, No. 2, pp. 174-179, June 1975.

Phillips, R. J., et al., "Simulation Gravity Modeling to Spacecraft-Tracking Data: Analysis and Application," *J. Geophys. Res.,* Vol. 83, No. B11, pp. 5455-5464, Nov. 10, 1978.

Posner, E. C., "Random Coding Strategies for Minimum Entropy," *IEEE Trans. Inform. Theor.,* Vol. IT-21, No. 4, pp. 388-391, July 1975.

Posner, E. C., "Life Cycle Costing with a Discount Rate," *Utilitas Mathematica,* Vol. 13, pp. 157-188, 1978.

Powell, R. V., and Hibbs, A. R., "An Entree for Large Space Antennas," *Astronaut. Aeronaut.,* Vol. 15, No. 12, pp. 58-64, Dec. 1977.

Reed, I. S., Truong, T. K., and Benjauthrit, B., "On Decoding of Reed-Solomon Codes over GF(32) and GF(64) Using the Transform Techniques of Winograd," *Conference Record, 1978 National Telecommunications Conference*, Vol. 2, Birmingham, Alabama, Dec. 3-6, 1978.

Simon, M. K., "A Generalization of Minimum-Shift-Keying (MSK) Type Signaling Based Upon Input Data Symbol Pulse Shaping," *IEEE Trans. Commun.*, Vol. COM-24, No. 8, pp. 845-856, Aug. 1976.

Simon, M. K., "An MSK Approach to Offset QASK," *IEEE Trans. Commun.*, Vol. COM-24, No. 8, pp. 921-923, Aug. 1976.

Simon, M. K., "The False Lock Performance of Costas Loops with Hard-Limited In-Phase Channel," *IEEE Trans. Commun.*, Vol. COM-26, No. 1, pp. 23-34, Jan. 1978.

Simon, M. K., "On the Calculation of Squaring Loss in Costas Loops with Arbitrary Arm Filters," *IEEE Trans. Commun.*, Vol. COM-26, No. 1, pp. 179-184, Jan. 1978.

Simon, M. K., "Tracking Performance of Costas Loops With Hard-Limited In-Phase Channel," *IEEE Trans. Commun.*, Vol. COM-26, No. 4, pp. 420-432, Apr. 1978.

Sjogren, W. L., et al., "Gravity Fields," *IEEE Trans. Geosci. Electron.*, Vol. GE-14, No. 3, pp. 172-183, July 1976.

Slade, M. A., et al., "Alsep-Quasar Differential VLBI," *The Moon*, Vol. 17, pp. 133-147, 1977.

Smith, E. K., and Edelson, R. E., *Radio Propagation Through Solar and Other Extra-terrestrial Ionized Media*, Publication 79-117, Jet Propulsion Laboratory, Pasadena, Calif., Jan. 15, 1980.

Tausworthe, R. C., *Standard Classifications of Software Documentation*, Technical Memorandum 33-756, Jet Propulsion Laboratory, Pasadena, Calif., Jan. 15, 1976.

Thomas, J. B., et al., "A Demonstration of an Independent-Station Radio Interferometry System With 4-cm Precision on a 16-km Base Line," *J. Geophys. Res.*, Vol. 81, No. 5, pp. 995-1005, Feb. 10, 1976.

Toukdarian, R. Z., *Final Engineering Report for Goldstone Operations Support Radar*, Technical Memorandum 33-800, Jet Propulsion Laboratory, Pasadena, Calif., Nov. 1, 1976.

Truong, T. K., and Reed, I. S., "Convolutions Over Residue Classes of Quadratic Integers," *IEEE Trans. Inform. Theor.*, Vol. IT-22, No. 4, pp. 468-475, July 1976.

Truong, T. K., and Reed, I. S., "Convolutions over Quartic Integer Residue Classes," *Proceedings of the International Conference on Information Sciences and Systems*, Patras, Greece, Aug. 19-24, 1976.

Truong, T. K., Liu, K. Y., and Reed, I. S., "Fast Number-Theoretic Transforms for Digital Filtering," *Electron. Lett.*, Vol. 12, No. 24, Nov. 1976.

Truong, T. K., et al., "X-Ray Reconstruction by Finite Field Transforms," *IEEE Trans. Nucl. Sci.*, Vol. NS-24, No. 1, pp. 843-849, Feb. 1977.

Truong, T. K., Golomb, S. W., and Reed, I. S., "Integer Convolutions Over the Finite Field $GF(3 \cdot 2^n + 1)$," *SIAM J. Appl. Math.*, Vol. 32, No. 2, pp. 356-365, Mar. 1977.

Truong, T. K., Reed, I. S., and Liu, K. Y., "Fast Algorithm for Computing Complex Number-Theoretic Transforms," *Electron. Lett.*, Vol. 13, No. 10, pp. 278-280, May 12, 1977.

Weber, W. J., III, "Performance of Phase-Locked Loops in the Presence of Fading Communication Channels," *IEEE Trans. Commun.*, Vol. COM-24, No. 5, pp. 487-499, May 1976.

Weber, W. J., III, Ackerknecht, W. E., and Kollar, F. J., *Viking X-Band Telemetry Experiment Final Report,* Technical Memorandum 33-794, Jet Propulsion Laboratory, Pasadena, California, Sept. 1, 1976.

Wong, J. S. L., et al., *Review of Finite Fields: Applications to Discrete Fourier Transforms and Reed-Solomon Coding,* JPL Publication 77-23, Jet Propulsion Laboratory, Pasadena, Calif., July 15, 1977.

Woo, R., "Measurements of the Solar Wind Using Spacecraft Radio Scattering Observations," in *Study of Traveling Inter-Planetary Phenomena,* pp. 81-100, D. Reidel Publishing Co., Dordrecht, Holland/Boston, 1977.

Woo, R., "Radial Dependence of Solar Wind Properties Deduced from Helios 1/2 and Pioneer 10/11 Radio Scattering Observations," *Astrophys. J.,* Vol. 219, No. 2, Part 1, pp. 727-739, Jan. 15, 1978.

Woo, R. T., "Observations of Turbulence in the Atmosphere of Venus Using Mariner 10 Radio Occultation Measurements," *J. Atmos. Sci.,* Vol. 32, No. 6, pp. 1084-1090, June 1975.

Yuen, J. H., *A Practical Statistical Model for Telecommunications Performance Uncertainty,* Technical Memorandum 33-732, Jet Propulsion Laboratory, Pasadena, Calif., June 15, 1975.

NASA—JPL—Coml., L.A., Calif.